A GUIDEBOOK ON THE USE OF SATELLITE GREENHOUSE GASES OBSERVATION DATA TO EVALUATE AND IMPROVE GREENHOUSE GAS EMISSION INVENTORIES

1st EDITION

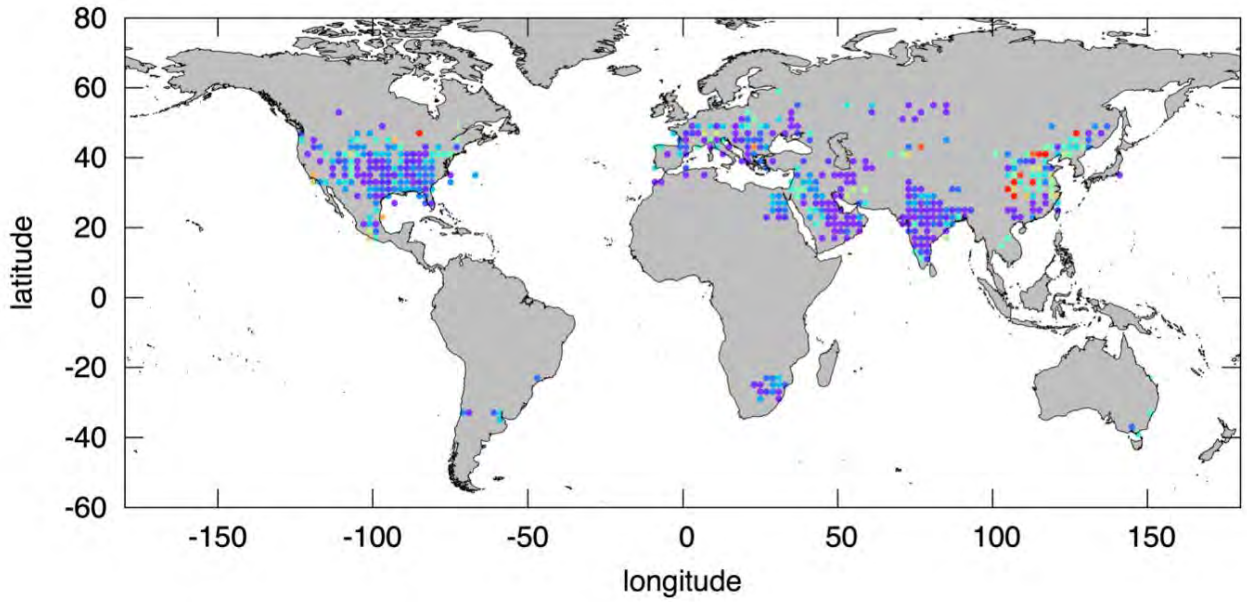

MARCH 2018

NATIONAL INSTITUTE FOR ENVIRONMENTAL STUDIES,

JAPAN

National Institute for Environmental Studies, Japan

Revision History
March 31, 2018: Revision 12a
April 5, 2018: Revision 12b

Map in the cover page : GOSAT observed XCO_2 anomalies averaged over 2° × 2° grid over anthropogenic sources regions over the globe for 2009–2012. See Section 4.4 for more details.

This document may be cited as:
Matsunaga T. and Maksyutov S (eds) (2018) A Guidebook on the Use of Satellite Greenhouse Gases Observation Data to Evaluate and Improve Greenhouse Gas Emission Inventories, Satellite Observation Center, National Institute for Environmental Studies, Japan, 129 pp.

Contact : Dr. Tsuneo Matsunaga (matsunag@nies.go.jp), Satellite Observation Center, National Institute for Environmental Studies, 16-2 Onogawa Tsukuba Ibaraki 305-8506 Japan.

Preface

The Paris Agreement, which entered into force on November 4, 2016, is the world's first framework to deal with climate change through both "mitigation" measures to reduce greenhouse gas (GHG) emissions and "adaptation" to the impacts of climate change. All nations started to take action to comply with the Paris Agreement, which has been ratified by 159 countries including developed and developing countries and the European Union as of September 2017.

The Paris Agreement defines a mechanism of "global stocktake" that all nations set the GHG reduction targets, report each progress, and assess the collective progress towards achieving the goals every five years after 2020.

Each country is required to report its national GHG emissions inventory under a highly transparent framework. To secure the transparency of the inventory, a system is necessary to compare and evaluate the inventories by some independent ways. One of the ways is a GHG observation method using satellite remote sensing techniques that Japan and other countries are working on.

In Japan, under a joint project by the Ministry of the Environment (MOE), the National Institute for Environmental Studies (NIES), and the Japan Aerospace Exploration Agency (JAXA), the Greenhouse gases Observing SATellite (GOSAT) "IBUKI" was launched as the world's first satellite dedicated to monitoring greenhouse gases in January 2009. The satellite has been observing global GHGs such as carbon dioxide (CO_2) and methane (CH_4) and monitoring their fluctuations for nine years since its launch.

With the "IBUKI" observations and the full use of ground-based and aircraft observations and modeling techniques, we have recently found the following trends for the first time in the world: whole-atmosphere monthly mean CO_2 concentrations reaching 406 ppm and CH_4 recording 1824 ppb in January 2018 with an annual increase with seasonal variations. In addition, we released the estimates of anthropogenic CO_2 and CH_4 emissions, which marked the first step towards utilizing the "IBUKI" series for environmental policy.

These observation outcomes leveraging the advantages of the satellite are contributing to the precise predictions of climate change. In addition, they become basic information for monitoring domestic and international efforts to reduce GHG emissions. We have been developing a successor "IBUKI-2" (GOSAT-2) to be launched in FY2018 and striving to advance techniques to assess and validate GHG emissions in large cities and large-scale emission sources using the IBUKI-2 observations.

On the other hand, in the United States, NASA launched the Orbiting Carbon Observatory 2 (OCO-2) in July 2014 and has been in operation. This satellite aims to characterize CO_2 sources and sinks on regional scales and quantify CO_2 variability over the seasonal cycles. The project teams of

OCO-2, GOSAT, and GOSAT-2 have been enforcing cooperative relationships from an early stage and making an effort to improve the accuracy of the data products by cross-calibration and validation under the Memorandum of Understanding among MOE, JAXA, NIES, and NASA, which was signed in March 2015.

In December 2017, JAXA and NIES made collaboration agreements with the European Space Agency (ESA), with the Centre National D'Etudes Spatiales (CNES), and with the German Aerospace Center (DLR). These agreements aim to increase the reliability of satellite GHG data and achieve its uniformity by cross-calibration and validation among the data from GOSAT, GOSAT-2, and GHG observing satellites operated or to be launched by European agencies.

To utilize these space-based GHG measurements for the system of estimating and evaluating each nation's GHG emissions, there are many possible challenges because innovative techniques are necessary. For example, one of the issues is technical assistance for inventory compilers in areas not having inventory data with high quality to compile and evaluate the GHG emissions inventories. It is necessary that Japan will cooperate internationally not only in a technical aspect such as analyzing satellite remote sensing data, but also in capacity building activities including training courses for inventory compilers through association with international organizations and development agencies.

We hope that this guidebook will be a good opportunity to introduce remote sensing techniques by GHG observation satellites as one of the methods for estimating and evaluating each nation's GHG emissions. As a result, we also hope that this guidebook will lead to taking further measures against global warming.

Masanobu Kimura
Director
Research and Information Office
Global Environment Bureau
Ministry of the Environment Japan

CONTENTS

ACKNOWLEDGEMENTS

The preparation and review of this guidebook has been supported by many individuals. We would like to thank the authors and co-authors of Chapter 4 for descriptions of their studies. In addition, the participants in the first and second expert meetings on the guidebook held in Tokyo in 2017 and 2018 are acknowledged for providing presentations and useful advice to prepare and improve the guidebook. Finally, appreciation is extended to many scientists and other contributors for providing helpful comments and suggestions on the draft edition of the guidebook. Especially, support for the revision of Section 1.1 and 2.1, provided by David Crisp, Eric Kort, Ray Nassar, and Alexander Turner, is sincerely appreciated. All the contributors are listed in the table below. We are most grateful for their valuable contributions.

The production of this guidebook has been financially supported by the Ministry of the Environment, Japan (MOE).

Tsuneo Matsunaga, Shamil Maksyutov, and Tomoko Kanno
National Institute for Environmental Studies (NIES), Japan

	Name	Affiliation	Contribution
1	Aoki, Shuji	Tohoku University, Japan	Chapter 4 Co-author
2	Bito, Chika	NIES	Participant in the 1st expert meeting
3	Boer, Rizaldi	Bogor Agricultural University, Indonesia	Participant in the 1st and 2nd expert meetings
4	Bovensmann, H.	University of Bremen, Germany	Chapter 4 Co-author
5	Briggs, Stephen	European Space Agency, Italy	Providing comments on the draft edition
6	Buchwitz, Michael	University of Bremen, Germany	Chapter 4 Lead author and Participant in the 1st and 2nd expert meetings via Skype
7	Burrows, J. P.	University of Bremen, Germany	Chapter 4 Co-author
8	Butz, Andre	German Aerospace Center (DLR), Germany	Chapter 4 Co-author
9	Chijimatsu, Satoshi	MOE	Participant in the 1st expert meeting
10	Counet, Paul	EUMETSAT, Germany	Providing comments on the draft edition

11	Crisp, David	California Institute of Technology, USA	Chapter 4 Co-author and Participant in the 2nd expert meeting
12	Dlugokencky, Edward J.	National Oceanic and Atmospheric Administration, USA	Chapter 4 Co-author
13	Endo, Takahiro	Remote Sensing Technology Center of Japan (RESTEC), Japan	Participant in the 1st and 2nd expert meetings
14	Ganesan, Anita	University of Bristol, UK	Participant in the 2nd expert meeting via Skype
15	Hakkarainen, Janne	Finnish Meteorological Institute (FMI), Finland	Chapter 4 Lead author and Participant in the 1st and 2nd expert meetings
16	Hatanaka, Elsa	NIES	Participant in the 1st and 2nd expert meetings
17	Hill, Timothy G.	University of Waterloo, Canada	Chapter 4 Co-author
18	Ialongo, Iolanda	FMI	Chapter 4 Co-author
19	Imasu, Ryoichi	University of Tokyo, Canada	Participant in the 1st and 2nd expert meetings
20	Inanaga, Asako	RESTEC	Participant in the 1st expert meeting
21	Isono, Kazuo	MOE	Participant in the 1st expert meeting
22	Ito, Akihiko	NIES	Chapter 4 Co-author
23	Ito, Hiroshi	NIES	Participant in the 2nd expert meeting
24	Janardanan, Rajesh	NIES	Chapter 4 Lead author and Participant in the 1st and 2nd expert meetings
25	Janssens-Maenhout, Greet	Joint Research Center, Italy	Participant in the 1st expert meeting via Skype
26	Jones, Dylan B.A.	University of Toronto, Canada	Chapter 4 Co-author
27	Kaewcharoen, Sivach	Office of Natural Resources and Environmental Policy and Planning, Thailand	Participant in the 1st and 2nd expert meetings
28	Kimura, Masanobu	MOE	Participant in the 2nd expert meeting
29	Kobayashi, Kazufumi	MOE	Participant in the 2nd expert meeting

30	Kort, Eric	University of Michigan, USA	Chapter 4 Lead author and Participant in the 1st and 2nd expert meetings via Skype
31	Kosaka, Naohumi	NIES	Participant in the 1st expert meeting
32	Kuze, Akihide	Japan Aerospace Exploration Agency (JAXA), Japan	Participant in the 1st expert meeting
33	Lauvaux, Thomas	Pennsylvania State University, USA	Participant in the 1st expert meeting via Skype
34	McLinden, Chris A.	Environment and Climate Change Canada, Canada	Chapter 4 Co-author
35	Miyauchi, Seiji	Japan Meteorological Agency, Japan	Participant in the 2nd expert meeting
36	Morimoto, Shinji	Tohoku University, Japan	Chapter 4 Co-author
37	Nakajima, Masakatsu	JAXA	Participant in the 1st expert meeting
38	Nakamura, Yuko	JAXA	Participant in the 1st expert meeting
39	Nakazawa, Takakiyo	Tohoku University, Japan	Chapter 4 Co-author
40	Nassar, Ray	Environment and Climate Change Canada, Canada	Chapter 4 Lead author and Participant in the 2nd expert meeting via Skype
41	Ninomiya, Keiichiro	NIES	Participant in the 1st and 2nd expert meetings
42	Niwa, Yosuke	Meteorological Research Institute, Japan	Participant in the 1st and 2nd expert meetings
43	Oda, Tomohiro	USRA／NASA Goddard Space Flight Center, USA	Chapter 4 Co-author and Participant in the 1st and 2nd expert meetings
44	Prabir, Patra	Japan Agency for Marine-Earth Science and Technology (JAMSTEC), Japan	Chapter 4 Lead author and Participant in the 1st and 2nd expert meetings
45	Prinn, Ronald G.	Massachusetts Institute of Technology, USA	Chapter 4 Co-author
46	Reuter, M.	University of Bremen, Germany	Chapter 4 Co-author
47	Saeki, Tazu	NIES	Chapter 4 Lead author and Participant in the 2nd expert meeting

48	Saigusa, Nobuko	NIES	Participant in the 2nd expert meeting
49	Saito, Makoto	NIES	Chapter 4 Co-author and Participant in the 1st an 2nd expert meetings
50	Schneising-Weigel, O.	University of Bremen, Germany	Chapter 4 Co-author
51	Shiomi, Kei	JAXA	Participant in the 1st expert meeting
52	Takemoto, Akio	MOE	Participant in the 1st expert meeting
53	Tamminen, Johanna	FMI	Chapter 4 Co-author and Participant in the 1st expert meeting via Skype
54	Tanabe, Kiyoto	Institute for Global Environmental Strategies, Japan	Participant in the 1st and 2nd expert meetings
55	Tanaka, Tetsuhiro	MOE	Participant in the 2nd expert meeting
56	Turner, Alexander	University of California at Berkeley, USA	Chapter 4 Lead author and Participant in the 1st and 2nd expert meetings via Skype
57	Uchida, Miyuki	NIES	Participant in the 1st expert meeting
58	Ueno, Mikio	Japan Meteorological Agency, Japan	Participant in the 1st and 2nd expert meetings
59	Urita, Shinji	MOE	Participant in the 1st expert meeting
60	Wunch, Debra	University of Toronto, Canada	Chapter 4 Co-author
61	Yoshida, Yukio	NIES	Chapter 4 Co-author

About this guidebook

This guidebook, “A Guidebook on the Use of Satellite Greenhouse Gases Observation Data to Evaluate and Improve Greenhouse Gas Emission Inventories” (hereinafter referred to as “this guidebook”), has been produced by the National Institute for Environmental Studies, as part of outsourced contracts with the Ministry of the Environment, Japan in FY 2016 and 2017.

The Paris Agreement, which entered into force in 2016, is the world’s first framework to deal with climate change through both “mitigation” measures to reduce greenhouse gas (GHG) emissions and “adaptation” to the impacts of climate change. The Paris Agreement defines a mechanism of “global stocktake” that all nations set the GHG reduction targets, report each progress, and assess the collective progress towards achieving the goals every five years after 2020.

There are several ways to compile a national GHG emission inventory (hereinafter referred to as “inventory”). The Paris Agreement requires each country to report its inventory under a highly transparent framework. To secure the transparency of the inventory, a system is necessary to compare and evaluate the inventories by some independent ways. One of the ways is a GHG observation method using satellite remote sensing techniques that Japan and other countries are working on. Especially in the field of satellite remote sensing of GHGs, research and development has been actively promoted. Several satellites to monitor GHGs have been in operation. The examples of such satellites include the Greenhouse gases Observing SATellite (GOSAT) launched by Japan in 2009, the Orbiting Carbon Observatory 2 (OCO-2) by the US in 2014, and Sentinel-5p by the European Space Agency in 2016. In addition, future plans for satellites are currently underway.

This guidebook targets each nation’s inventory compilers and researchers in the related fields. The objective of this guidebook is to explain methodology to compare and evaluate inventories, which all nations report under the Paris Agreement, by using satellite remote sensing techniques (Chapter 2 and 3), and to introduce their practical case studies (Chapter 4). The case studies include the latest research at various spatial scales from global and sub-continental level to individual large-sized coal power plants.

All satellite GHG data introduced in this guidebook can be downloaded for free from each satellite website.

Furthermore, capacity building activities for the inventory compilers are being considered. We have been examining the feasibility of the activities such as conducting lectures and training courses using this guidebook as one learning tool, and providing various data, software, and work environment.

We hope that this guidebook and the future capacity building activities will help the inventory compilers to widely use the methodology to compare and evaluate the inventories using satellite remote sensing techniques towards the first global stocktake.

1. OVERVIEW

1.1 Background

The Earth's environment is changing rapidly and these changes are affecting natural terrestrial and marine ecosystems, agriculture, human health, economic activity, and even national security. Recognizing the impact of these changes, the Sustainable Development Goals (SDGs) defined by the United Nations (UN) in 2015 include "Goal 13: Take urgent action to combat climate change and its impacts". The rising concentrations of atmospheric greenhouse gases (GHGs) such as carbon dioxide (CO_2) and methane (CH_4) are key drivers of climate change (IPCC, 2013). Since the dawn of the industrial age, fossil fuel combustion and other human activities have increased the atmospheric CO_2 concentration by more than 40%, from less than 280 parts per million (ppm) in 1750 to more than 400 ppm today. Over that period, a diverse range of human activities increased the atmospheric CH_4 concentrations by more than 2.5 times, from 750 parts per billion (ppb) to more than 1.85 ppm. These rapid increases are raising concerns because CO_2 and CH_4 are efficient atmospheric GHGs and the primary drivers of climate change. Social, national, and international cooperation and collaboration are needed to reduce CO_2 and CH_4 emissions to acceptable levels.

The United Nations Framework Convention on Climate Change (UNFCCC) was established in 1994 to stabilize “greenhouse gas concentrations in the atmosphere at a level that would prevent dangerous anthropogenic interference in the climate system.” The Paris Agreement from the 21st session of the Conference of the Parties (COP21) of the UNFCCC, which entered into force in 2016, reinforced the urgent need for dramatic reductions in GHG emissions to keep the global temperature rise this century well below 2 degrees Celsius above pre-industrial levels. Parties to the Agreement defined “nationally determined contributions” (NDCs) to a global GHG reduction effort. These NDCs are expected to evolve in time, based a Global Stocktake conducted at 5 year intervals.

To track their progress toward their NDCs and the global GHG emission reduction targets, each Party agreed to provide “A national inventory report of anthropogenic emissions by sources and removals by sinks of greenhouse gases, prepared using good practice methodologies accepted by the Intergovernmental Panel on Climate Change and agreed upon by the Conference of the Parties serving as the meeting of the Parties to this Agreement.” To promote transparency, accuracy, completeness, consistency, comparability, and environmental integrity of the Stocktake, the Agreement defines an enhanced “Transparency Framework”.

Direct atmospheric measurements of CO_2 and CH_4 are highly complementary to conventional GHG inventories and could provide an independent Measurement, Reporting and Verification (MRV) approach for NDCs in addition to providing useful information for improving inventories. The “2006 IPCC Guidelines for National Greenhouse Gas Inventories” (IPCC 2006 Guidelines)

mandates reports on GHG emissions and removals at national scales using a bottom-up approach that includes specific gases (CO_2, CH_4, N_2O, and others), and Sectors (Energy, Industrial Processes, and Products, Agriculture, Forestry, Land Use, Waste, and Other), each of which is divided into Categories (e.g. transport) which are subdivided into sub-categories (e.g., cars). When implemented fully, the methods specified in these Guidelines can accurately identify and characterize emissions sources and natural sinks at national scales. However, many developing nations do not have the resources needed to compile comprehensive bottoms-up inventories in the presence of rapid economic, social, or environmental change. Other natural and anthropogenic emission sources or natural sinks of GHGs are poorly constrained due to uncertainties in the "activity data" or "emission factors" used in their derivation.

In contrast, direct atmospheric measurements of CO_2, CH_4, and other GHGs can provide an integrated constraint on their atmospheric concentrations and its trends over time. The most accurate measurements are collected by a network of ~125 surface stations that are coordinated by World Meteorological Organization Global Atmospheric Watch (WMO GAW) program. In situ measurements from surface flasks, towers, and aircraft in this network provide the best available constraints on the atmospheric concentrations of CO_2, CH_4 and other GHGs and their trends at continental to global scales. While this network has grown steadily since 1958, and now spans the globe, it is still too sparse to provide insight into national scale source and sinks. Space based remote sensing measurements of these gases provide much greater spatial resolution and coverage, but have lower precision and accuracy. As these space based measurement capabilities improve and the space based GHG measurements are validated against the more accurate ground-based in situ standards by well-documented, scientifically sound methodologies, they could play a much larger role in the evaluation and improvement of national inventories.

The Intergovernmental Panel on Climate Change (IPCC), through its Task Force on National Greenhouse Gas Inventories (TFI), has published a series of documents starting from "2006 IPCC Guidelines for National Greenhouse Gas Inventories" together with their supplemental documents such as "2013 Supplement to the 2006 IPCC Guidelines for National Greenhouse Gas Inventories: Wetlands" and "2013 Revised Supplementary Methods and Good Practice Guidance Arising from the Kyoto Protocol". As part of the ongoing "2019 Refinement to the 2006 IPCC Guidelines for National Greenhouse Gas Inventories", a request for "updating verification guidance …, especially guidance on comparisons with atmospheric measurements …" was approved by IPCC and included in the "2019 Refinement" plan. To implement this strategy, here we review recent progress in the use of atmospheric GHG observations for emission estimates suitable for comparison to the national GHG emission inventories. The Refinement will be authorized at IPCC General Assembly to be held in May 2019.

1.2 Objective of This Guidebook

The objective of this guidebook is to provide a general and up-to-date overview on satellite remote sensing of GHGs and their applications to GHG emission inventories to inventory compilers and researchers who are interested in using satellite GHG data to evaluate and improve national greenhouse gas emission inventories.

The aim of the draft edition of this guidebook is to foster discussions on the use of satellite greenhouse gas data between remote sensing scientists and inventory compilers, and to obtain valuable comments towards the first edition. The first edition of this guidebook will be used as one of reference books used in future capacity building activities for inventory compilers and users.

1.3 Structure of This Guidebook

The structure of this guidebook is as follows:

- Chapters 2 and 3 provide an overview satellite remote sensing of greenhouse gases and how to retrieve fluxes from these measurements that can be compared GHG inventories.
- Chapter 4 provides the latest case studies regarding satellite remote sensing of GHGs and emission inventories. Note that the essential parts of these case studies have been published in peer-reviewed journals.
- List of references, acronyms, abbreviations, and greenhouse gas-observing satellites are provided in Appendices.

Box 1 in the next page provides a brief overview of the process to estimate surface fluxes of carbon dioxide and methane from satellite remote sensing data. Box 2 provides explanations of "verification" in IPCC and UNFCCC documents.

Box 1. A 6-step process to estimate surface fluxes of carbon dioxide and methane from space-based remote sensing measurements collected by satellites.

1	Acquire precise, high resolution spectra within CO_2 and CH_4 absorption bands at infrared wavelengths at high spatial resolution over the globe. Co-bore-sighted spectra of the molecular oxygen (O_2) A-band are also useful for estimating the total dry air column abundance, the surface pressure, and the presence, distribution, and total optical depths of clouds and aerosols.
2	Calibrate these space based spectroscopic measurements to convert them from instrument units (i.e. time tagged data numbers) to geophysical units (i.e. photons/second/steradian/micron) and to relate them to internationally-recognized radiometric, spectroscopic, and geometric standards, so that they can be cross-validated and combined with other types of measurements and model results.
3	Use a remote sensing retrieval algorithm to estimate the column-averaged dry air mole fractions of CO_2 and CH_4, (XCO_2, XCH_4) and other relevant atmospheric and surface state properties (i.e. surface pressure and reflectance, profiles of atmospheric temperature, water vapor, clouds and aerosols) from each sounding.
4	Validate the XCO_2 and XCH_4 measurements against available standards, including ground-based up-looking remote sensing observations and vertical profiles of CO_2 and CH_4 obtained by aircraft.
5	Perform a flux inversion experiment to estimate the surface GHG fluxes needed to maintain the observed XCO_2 and XCH_4 distribution in the presences of the prevailing winds.
6	Validate the retrieved flux distribution against available standards, including direct GHG flux measurement from networks of flux towers, and/or comparisons of the CO_2 and CH_4 profiles returned by the flux inversion models against available vertical profiles of these gases measured from aircraft.

Note: Experience from the first generation of space-based GHG satellites confirms that this application requires space-based sensors with an unprecedented combination of precision, accuracy, spectral and spatial resolution, and coverage. These factors also impose stringent requirements on calibration and calibration stability and the validation of the XCO_2 and XCH_4 products retrieved from their measurements. Chapter 2 summarizes the progress to date and near term plans for instrument development, calibration, validation, and the methods needed to retrieve estimates of XCO_2 and XCH_4 from space based observations. Approaches for performing flux inversion are described in Chapter 3.

Box 2. About "Verification"

In the title of the draft edition of this guidebook, a technical term, "verification", was used. As we received several suggestions to use words other than "verification", we changed the title of the 1st edition from the draft edition.

Here, the explanations of "verification" in IPCC and UNFCCC documents are excerpted to avoid any confusion.

Chapter 6, Volume 1, 2006 IPCC Guidelines for National Greenhouse Gas Inventories:

In Page 6.5:

"*Verification refers to the collection of activities and procedures conducted during the planning and development, or after completion of an inventory that can help to establish its reliability for the intended applications of the inventory. For the purposes of this guidance, verification refers specifically to those methods that are external to the inventory and apply independent data, including comparisons with inventory estimates made by other bodies or through alternative methods. Verification activities may be constituents of both QA and QC, depending on the methods used and the stage at which independent information is used.*"

In Page 6.19:

"*For the purposes of this guidance, verification activities include comparisons with emission or removal estimates prepared by other bodies and comparisons with estimates derived from fully independent assessments, e.g., atmospheric concentration measurements. Verification activities provide information for countries to improve their inventories and are part of the overall QA/QC and verification system. Correspondence between the national inventory and independent estimates increases the confidence and reliability of the inventory estimates by confirming the results. Significant differences may indicate weaknesses in either or both of the datasets. Without knowing which dataset is better, it may be worthwhile to re-evaluate the inventory.*"

https://www.ipcc-nggip.iges.or.jp/public/2006gl/pdf/1_Volume1/V1_6_Ch6_QA_QC.pdf

Handbook on Measurement, Reporting, and Verification for Developing Country Parties:

In Page 16:

"*Verification is addressed at the international level through ICA of BURs, which is a process to increase the transparency of mitigation actions and their effects, and support needed and received.17 National communications are not subject to ICA. At the national level, verification is implemented through domestic MRV mechanisms to be established by non-Annex I Parties, general guidelines for which were adopted at COP 19 in 2013. Provisions for verification at the domestic level that are part of the domestic MRV framework are to be reported in the BURs. Special provisions have been adopted for verification of REDDplus activities, as discussed in chapter 3.7.*"

https://unfccc.int/files/national_reports/annex_i_natcom_/application/pdf/non-annex_i_mrv_handbook.pdf

2. SATELLITE OBSERVATIONS AND DATA APPLICATIONS, PART 1: SATELLITE OBSERVATIONS, GHG CONCENTRATION RETRIEVALS AND VALIDATION

This chapter introduces the basics of space-based remote sensing of GHGs, summarizes the progress made by past and present GHG missions, and the prospects for future missions. Section 2.1 describes the background physics and Section 2.2 provides a brief history of this type of remote sensing. In Section 2.3, the definitions of satellite data products are summarized. Section 2.4 describes the methodology to derive greenhouse gas concentrations from satellite observation. The validation of derived greenhouse gas concentrations is discussed in Section 2.5.

2.1 INTRODUCTION

High resolution spectra of sunlight that is reflected or thermal radiation that is emitted by the Earth's surface and atmosphere carry information about the thermal structure and composition of the surfaced and atmosphere. Spectra of reflected solar and emitted thermal radiation collected by remote sensing instruments on orbiting spacecraft can therefore be analyzed to yield information about the surface and atmospheric state.

Solar radiation reflected by the Earth and its absorption by atmosphere is typically divided into ultraviolet (UV, 10-400 nm), visible (VIS, 400-700 nm), near infrared (NIR, 700-1400 nm), and short wavelength infrared (SWIR, 1400-3000 nm) wavelengths. Thermal infrared radiation (TIR) emitted by the Earth and its atmosphere is typically divided into mid-wavelength infrared (MWIR, 3-8 μm), long-wavelength infrared (LWIR, 8-15 μm) and far infrared (15-1000 μm). Molecular gases such as CO_2 and CH_4 interact with this solar and thermal radiation by absorbing and emitting only specific wavelengths (or colors) of light. These wavelengths are determined by the electronic, vibrational and rotational energy transitions of the molecules, which, in turn, are dictated by quantum mechanics. These transitions introduce narrow, dark, "absorption lines" or bright "emission lines" in spectra recorded by orbiting spacecraft (Fig. 2.1-1).

The intensity (darkness) of an absorption line produced by a given gas at a specific wavelength in a reflected solar spectrum depends the optical cross section of each molecule of that gas at that wavelength, the number density of that type of molecule along the atmospheric optical path and the length of the optical path that traverses the atmosphere. For a spectrum of thermal radiation, the darkness of an absorption line or brightness of the emission line associated with a given molecular transition depends on these factors as well as the temperature variations along the optical path.

Given information about the vertical structure, composition and optical properties of the atmosphere and the observing geometry, the spectrum of reflected sunlight or emitted thermal radiation can be simulated using an atmospheric radiative transfer model. For these applications, the wavelength-, pressure-, and temperature-dependent optical cross sections of CO_2, CH_4 and other atmospheric gases are determined from increasingly accurate measurements performed by

laboratory spectroscopists. The distribution of atmospheric pressure, temperature, and the concentration of absorbing gases and other properties of the surface and atmosphere that can affect the spectrum, such as the absorption and scattering by the surface or by cloud or aerosol particles, can be assumed, based on an environmental model, or derived directly from the measurements, using a remote sensing retrieval algorithm.

To retrieve estimates of greenhouse gas concentrations from space based observations, a remote sensing retrieval algorithm typically incorporates three components:

- A surface-atmosphere radiative transfer model, like that describe above;
- An "instrument model" that simulates the spectrally-dependent response of the satellite instrument; and
- An "inverse model" to optimize the atmospheric trace gas abundance and distribution and other surface or atmospheric properties to yield a good fit between the simulated and observed spectra.

In a typical satellite remote sensing retrieval experiment, an initial surface and atmospheric state is assumed, based on prior knowledge. This "state vector" is used along with information about the illumination and viewing geometry to generate a spectrally-dependent radiance spectrum at the top of the atmosphere. In addition to a high resolution radiance spectrum, the radiative transfer model generates "Jacobians," which specify the rate of change of the radiances at each output wavelength with respect to changes in the abundance or optical properties of the absorbing gas or other atmospheric properties at any level of the atmosphere.

Each synthetic spectrum is processed with the instrument model and compared to the spectrum observed by the satellite. The spectrally-dependent differences between the observed and synthetic spectrum are then used along with the Jacobians in the spectral inverse model to update the trace gas concentrations or other aspects of the assumed surface-atmosphere state to improve the fit. This update state is then used to re-compute the synthetic spectrum, and the process is repeated until the difference between the observed and simulated spectra agree to within a specified tolerance. The final surface-atmosphere state, including the updated GHG concentrations is then saved.

The approach described above can be used to retrieve estimates of CO_2 and CH_4 from either reflected solar radiation or from emitted thermal radiation, but these two types of measurements provide different types of information. Thermal infrared spectra can yield information about the CO_2 and CH_4 concentrations at altitudes between 5 and 10 km at all times of day. However these measurements have very little sensitivity to GHG gas concentrations near the surface, where most sources and sinks are located. They therefore only provide insight into GHG distributions on continental to global scales.

Measurements of reflected sunlight collected with SWIR CO_2 and CH_4 bands can be combined with O_2 observations collected within the O_2 A-band to yield estimates of the column-averaged dry air mole fractions of CO_2 and CH_4 called XCO_2 and XCH_4, which are most sensitive to the near-surface concentrations of these gases. This approach has therefore been widely adopted for space based GHG flux inversion experiments, and is the primary focus of this guidebook.

A critical limitation of this approach is that it can only be used during the day. In addition, while space based measurements of reflected sunlight can yield very precise measurements, the accuracy of the retrieved XCO_2 and XCH_4 estimates can be compromised by spatially coherent biases, that can be misinterpreted as evidence for sources and sinks. These biases originate from a variety of sources including instrument calibration errors and optical path length uncertainties introduced by optically-thin clouds and aerosols, pointing errors.

To address these concerns, a comprehensive validation approach has been implemented to identify, characterized and mitigate the impact of these biases. Uplooking spectroscopic measurements of the gases collected by the Total Carbon Column Observing Network (TCCON, Wunch et al., 2011) serve as a transfer standard for validating satellite XCO_2 and XCH_4 measurements against the in situ standards maintained by the WMO network. This approach has allowed rapid improvements in the products returned by the first generation of space based GHG sensors, but additional improvements are needed to provide timely, quantified guidance on progress towards emission reduction targets (NDCs) at national scales. These improvements continue to be a major focus of the satellite GHG program.

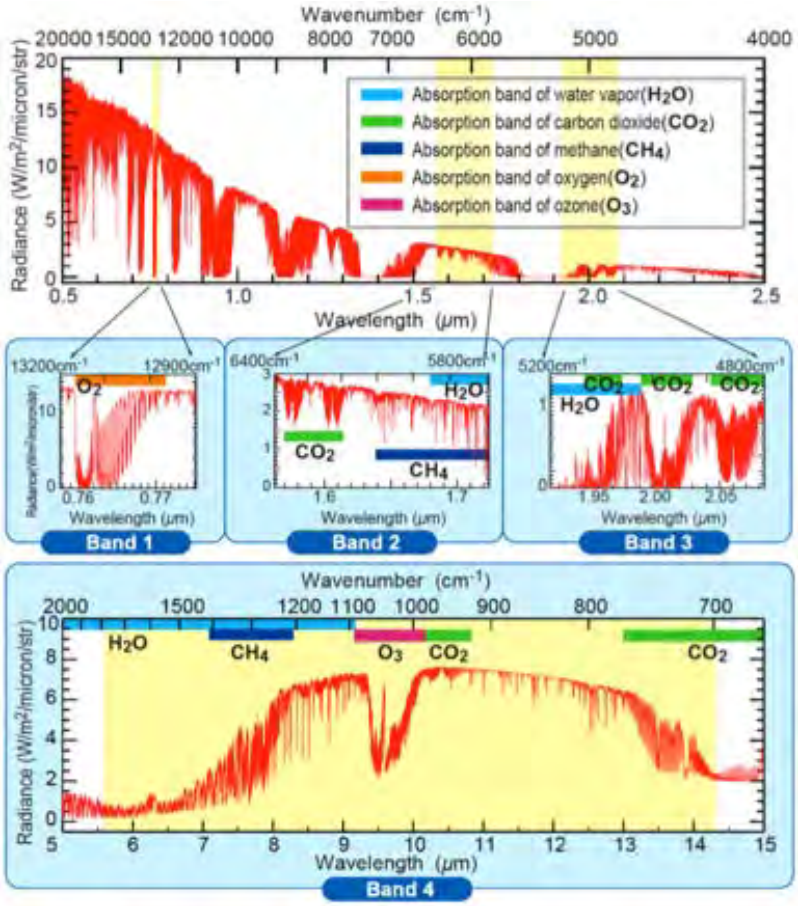

Fig. 2.1-1. The spectrum of the sunlight and thermal emission from the Earth showing the absorption bands of several gas species.
http://www.gosat.nies.go.jp/eng/GOSAT_pamphlet_en.pdf

2.2 BRIEF HISTORY OF SATELLITE REMOTE SENSING OF GREENHOUSE GASES

The first satellite instrument to exploit the SWIR spectral region for observing CO_2 and CH_4 was the Scanning Imaging Absorption Spectrometer for Atmospheric CHartographY (SCIAMACHY). SCIAMACHY was designed for general atmospheric chemistry observations and was the first space based instrument designed to observe the greenhouse gases CO_2 and CH_2 at near infrared wavelengths. This pioneering experiment was a German led national contribution to the European Space Agency Envisat mission, which operated from 2002–2012. SCIAMACHY observed the solar radiance upwelling at the top of the atmosphere from the UV to SWIR regions in nadir and limb viewing geometries. It also made measurements of the extraterrestrial solar irradiance. It had 8 moderate resolution spectral channels: 6 measuring contiguously from 0.21 to 1.75 μm and two additional SWIR channels spanning 1.94-2.04 μm and 2.26-2.38 μm. Its spectral bands were chosen to measure column abundances and concentrations of a broad range of key trace gases, aerosol and cloud particles in addition to the first space based measurements of the total column amounts and their dry column mole fractions of CO_2 and CH_4.

Some specifications of SCIAMACHY related to greenhouse gases observation are summarized in Table 2.2-1. SCIAMACHY data are used in the case studies described in Section 4-1, 4-3, and 4-5.

Figure 2.2-1. ENVISAT (http://earth.esa.int/image/image_gallery?img_id=391530).

Table 2.2-1. Some specifications of SCIAMACHY, GOSAT, and OCO-2. Note that the values shown here are not test results nor actual performances of the instruments.

Mission	Target greenhouse gases	Spectral bands*	Spectral resolution	Nadir footprint size
SCIAMACHY	CO_2 and CH_4	0.60 - 0.81 μm 0.97 - 1.77 μm 1.93 - 2.04 nm 2.26 - 2.39 nm	0.48 nm 1.48 nm 0.22 nm 0.26 nm	32 x 60 km^2
GOSAT	CO_2 and CH_4	0.76 - 0.78 μm 1.56 - 1.72 μm 1.92 - 2.08 μm 5.5 - 14.3 μm	0.2 cm^{-1} (0.012 nm) 0.2 cm^{-1} (0.054 nm) 0.2 cm^{-1} (0.080 nm) 0.2 cm^{-1} (0.6 - 4 nm)	10.5 km
OCO-2	CO_2	0.757 - 0.772 μm 1.59 - 1.63 μm 2.04 - 2.08 μm	0.042 nm 0.082 nm 0.104 nm	1.3 x 2.3 km^2

*: Used for greenhouse gases measurements.

The next generation of greenhouse gases remote sensing missions after SCIAMACHY included the Japanese Greenhouse Gases Observing SATellite (GOSAT) and US Orbiting Carbon Observatory (OCO). GOSAT was successfully launched in 2009 and continues to operate well beyond its design lifetime (5 years). The launch of OCO also in 2009 failed due to a malfunction of the launch vehicle. The replacement satellite, OCO-2, was successfully launched in 2014 and has been operating since then.

OCO and OCO-2 were specifically designed for the measurement of CO_2. GOSAT also measures methane (CH_4) as well. Their spectrometers observe relatively narrow spectral bands in the NIR and SWIR regions with the spectral resolution and the signal to noise ratio high enough to

obtain accurate and precise greenhouse gases concentrations. GOSAT also collects measurements of temperature and trace gases in the TIR part of the spectrum.

These two satellites have different strategies to record spectral measurements necessary for CO_2 and methane. GOSAT uses a Fourier Transform Spectrometer (FTS) to cover a wide spectral range from the NIR to TIR regions with a very high spectral resolution. Due to engineering constraints, the FTS instantaneous field of view (IFOV) is relatively large (nadir footprint size is 10.5 km in diameter) and data acquisition intervals are relatively long (4–5 seconds / measurement). However, GOSAT has the advantage of a very versatile (agile) pointing system which can rapidly change the line of sight of the instrument within ±20° of nadir in the along-track direction and ±35° of nadir in the cross-track direction (Kuze et al. (2009)). Note that GOSAT Research Announcement Principal Investigators can submit specific observation requests for GOSAT FTS within engineering and resource limitations.

OCO-2 uses an imaging grating spectrometer to measure CO_2. OCO-2 observes 8 parallelogram-shaped footprints across its swath every 0.333 seconds. Each parallelogram is ~2.25 km in the along-track direction due to the motion of the spacecraft and up to 1.3 km wide in the cross track direction, but often much narrower due to the orientation of the OCO-2 entrance slit as it rotates 360° every orbit. This small IFOV or nadir footprint size yields more cloud-free data than GOSAT. OCO-2 uses satellite attitude changes to aim at specific targets rather than a dedicated small pointing system like GOSAT.

Some key specifications of GOSAT and OCO-2 are also summarized in Table 2.2-1. GOSAT data are used in the case studies described in Section 4-3, 4-4, 4-5, 4-6, and 4-8. OCO-2 data are used in Section 4-2 and 4-9.

Figure 2.2-2. (Left) GOSAT (http://jda-strm.tksc.jaxa.jp/archive/photo/P-029-11965/c42b80d2a4d3461d9b2e8275d1136bfa.jpg) and (right) OCO-2 (https://www.jpl.nasa.gov/spaceimages/images/mediumsize/PIA18374_ip.jpg).

The third generation of greenhouse gases remote sensing missions launched quite recently or to be launched by the early 2020's includes:

GHGSat (a Canadian private company): Claire (launched in 2016) - CH_4

China: TanSat (launched in 2016) - CO_2

EU: TROPOMI (onboard Sentinel-5p launched in 2017) - CH_4,

Sentinel-4 (to be launched in 2019),

Sentinel-5 (to be launched in 2020)

China: GMI (onboard Gaofen-5 to be launched in 2018) - CO_2 and CH_4

Japan: GOSAT-2 (to be launched in FY2018) - CO_2 and CH_4

US: OCO-3 (to be deployed on the International Space Station no earlier than 2018) - CO_2

France: MicroCarb (to be launched in 2021) - CO_2

France and Germany: MERLIN (to be launched in 2021) - CH_4,

US: GeoCARB (to be launched in 2022) - CO_2 and CH_4

EC/ESA: Copernicus Sentinel 7 - CO_2 and CH_4

Appendix-3 is a list of satellite missions for greenhouse gases remote sensing and related resources.

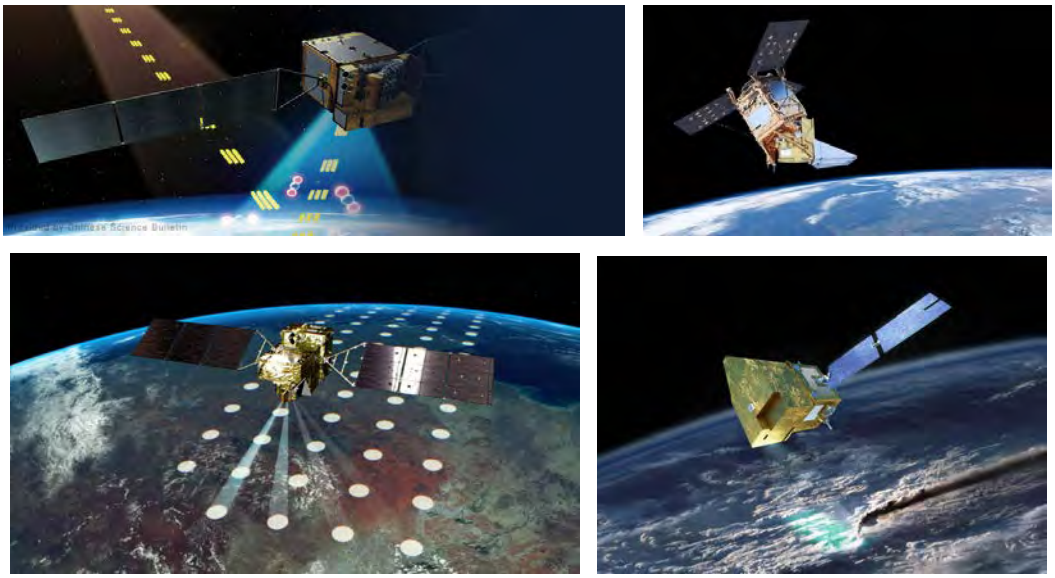

Figure 2.2-3. (Upper left) TanSat (http://english.cas.cn/head/201612/W020161222496366546461.jpg), (Upper right) Sentinel-5p (http://www.esa.int/var/esa/storage/images/esa_multimedia/images/2017/10/sentinel-5p_hl_pr/17203927-2-eng-GB/Sentinel-5P_HL_PR_highlight_std.jpg), (Lower left) GOSAT-2(http://jda-strm.tksc.jaxa.jp/archive/photo/P100010579/1c1679dfd228732ea7e8f5062ff3bce7.jpg), and (Lower right) MicroCarb (https://microcarb.cnes.fr/sites/default/files/styles/large/public/drupal/201512/image/bpc_microcarb-satellite.png?itok=39m6wHbr).

2.3 PRODUCTS OF SATELLITE REMOTE SENSING OF GREENHOUSE GASES

Satellite data are generally distributed as "Products" which contain satellite measurements and other related data with their prescribed formats. Products are often categorized into several levels. Below are general descriptions of each level. Note that detailed definitions of products may differ according to missions.

- Level 1 products contain physical parameters directly measured by space-borne instruments such as spectral radiances.
- Level 2 products contain physical parameters retrieved from parameters in Level 1 products such as concentrations of greenhouse gases.
- Level 3 products contain gridded maps at some given spatial and temporal resolution. They are primarily based on Level 2 products and may include some gap filling.
- For GOSAT and OCO-2, Level 4A products are defined as the regional flux estimated based on the inversion analysis of observed greenhouse gas concentrations (Level 2 products) with a help of atmospheric transport models.

GOSAT standard products from Level 1 to 4 can be freely downloaded from NIES GOSAT Data Archive Service (GDAS, https://data2.gosat.nies.go.jp/index_en.html, Figure 2.3-1). OCO-2 Level 1 and 2 products can be downloaded from NASA Goddard Earth Science Data & Information Services Center (GES DISC, https://disc.gsfc.nasa.gov/datasets?page=1&keywords=OCO-2). Additionally, GOSAT Level 2 data processed by different retrieval algorithms can be downloaded from several sites such as European Space Agency's GHG-CCI (http://www.esa-ghg-cci.org/sites/default/files/documents/public/documents/GHG-CCI_DATA.html) and NASA's CO_2 Virtual Science Data Environment (https://co2.jpl.nasa.gov).

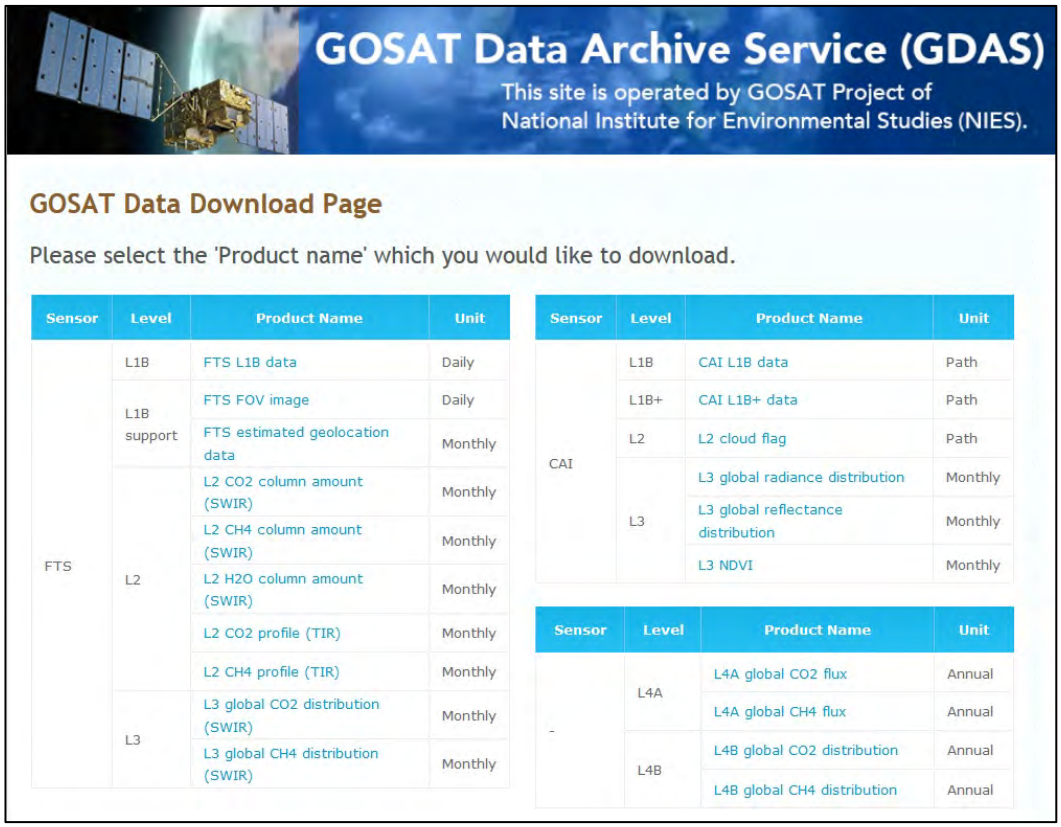

Figure 2.3-1 The data download page of NIES GOSAT Data Archive Service.

2.4 RETRIEVAL ALGORITHMS TO DERIVE GREENHOUSE GAS CONCENTRATIONS FROM SWIR SPECTRAL DATA

An overview of the algorithms to derive greenhouse gas concentrations from spectral data in the SWIR region is given in this section. These methods, often called the retrieval algorithms, are being used in the operational Level 2 product generation for the existing satellites such as GOSAT and OCO-2. Thus, explanations in this section are concise enough to understand the characteristics and the limitations of these products.

Spaceborne NIR/SWIR spectrometers observe the sunlight reflected at the Earth's surface and/or scattered in the atmosphere. These spectra are calibrated using pre-launch and on-orbit measurements of radiometric, spectroscopic, polarimetric, and geometric standards to convert them from instrument unit to geo-located spectral radiances (Level 1 data products). High resolution spectra of this sunlight contain many narrow dark lines due to the absorption of sunlight by gas molecules along the atmospheric optical path. The locations (wavelengths) and the relative intensities of the absorption lines is unique to each gas species and the overall intensities of the absorptions is determined mostly by the number of gas molecules along the atmospheric path as the sun light travels toward the Earth surface and is then reflected toward the satellite. By analyzing the intensities of these absorption lines, the column-averaged dry-air mole fractions (hereafter, column concentrations) of greenhouse gases such as carbon dioxide (XCO_2) and methane (XCH_4) can be

derived. In case of GOSAT and OCO-2, absorption lines around 1.6 μm and 2.0 μm are used for CO_2 and CH_4 measurements. Molecular oxygen (O_2) absorption lines around 0.76 μm are also used to estimate the surface air pressure and the column concentration of dry air along the same optical path used to observe CO_2 and CH_4.

The observed NIR/SWIR spectra, however, are affected by not only the column concentrations of greenhouse gases, but also other atmospheric constituents, land / ocean surface reflectance, and instrumental parameters. Some of these properties are stable, but some are spatially and temporally variable. To derive XCO_2 and XCH_4 from satellite data with the accuracy of about 0.25%, it is necessary to estimate the environmental parameters simultaneously with XCO_2 and XCH_4. The impact of the instrumental parameters is established through the calibration process.

To retrieve XCO_2 or XCH_4 from GOSAT and OCO-2 spectra, the observed spectrum is simulated with a surface/atmospheric radiative transfer model using an assumed (a priori) atmospheric and surface state. An inverse model based on optimal estimation (Rodgers, 2000) is then used to update gas concentrations and other properties of the surface and atmospheric state to minimize the difference between the observed and simulated spectra, and this process is repeated until a good fit is achieved. Mathematical details of these algorithm can be found in O'Dell et al. (2012), Yoshida et al. (2013), and the literature cited therein.

Scattering by clouds and aerosols (dust, haze, smog) can introduce uncertainties in the atmospheric path length that can introduce errors in the XCO_2 and XCH_4 retrievals. To minimize these errors, the optical properties and vertical distribution of atmospheric aerosols and clouds must be retrieved simultaneously with the gas concentrations. Measurements acquired in the O_2 A-band at 0.76 μm provide insight into the cloud and aerosol scattering at that wavelength. However, an accurate description of the wavelength dependent optical properties of clouds and aerosols is needed to estimate their impact on the CO_2 and CH_4 bands at wavelengths near 1.61, 1.67, and 2.06 μm in the SWIR. Estimating these properties has been a major focus of the current researches, and some users have adopted a "Proxy Method" that assumes that the scattering is the same in the nearby CO_2 and CH_4 bands, so that if the concentration of one of these two gases is assumed to be known, the other can be retrieved. For methane, see Schepers et al. (2012), Parker et al. (2015), and the literature cited therein.

As most retrieval algorithms can successfully process only soundings with little or no cloud contaminations within IFOV of their spectrometers, it is important to implement reliable cloud detection and screening algorithms in the operational data processing system. Cloud information can be derived from the SWIR reflectance spectra themselves. In the case of GOSAT, cloud maps derived from a multispectral imager (Cloud and Aerosol Imager, CAI) are also used to detect cloud fragments in the FTS IFOV. For OCO-2, clouds are screened using spectroscopic observations in the O_2 A-band and CO_2 bands at 1.61 and 2.06 μm (see Taylor et al. 2011; 2016) or inferred from

co-located images.

Figure 2.4-1 shows the processing flow for GOSAT FTS SWIR Level 2 CO_2 and CH_4 data products at NIES. GOSAT CAI Level 1B and Level 2 cloud flag processing is incorporated in this figure as they provide cloud maps used in FTS Level 2 processing.

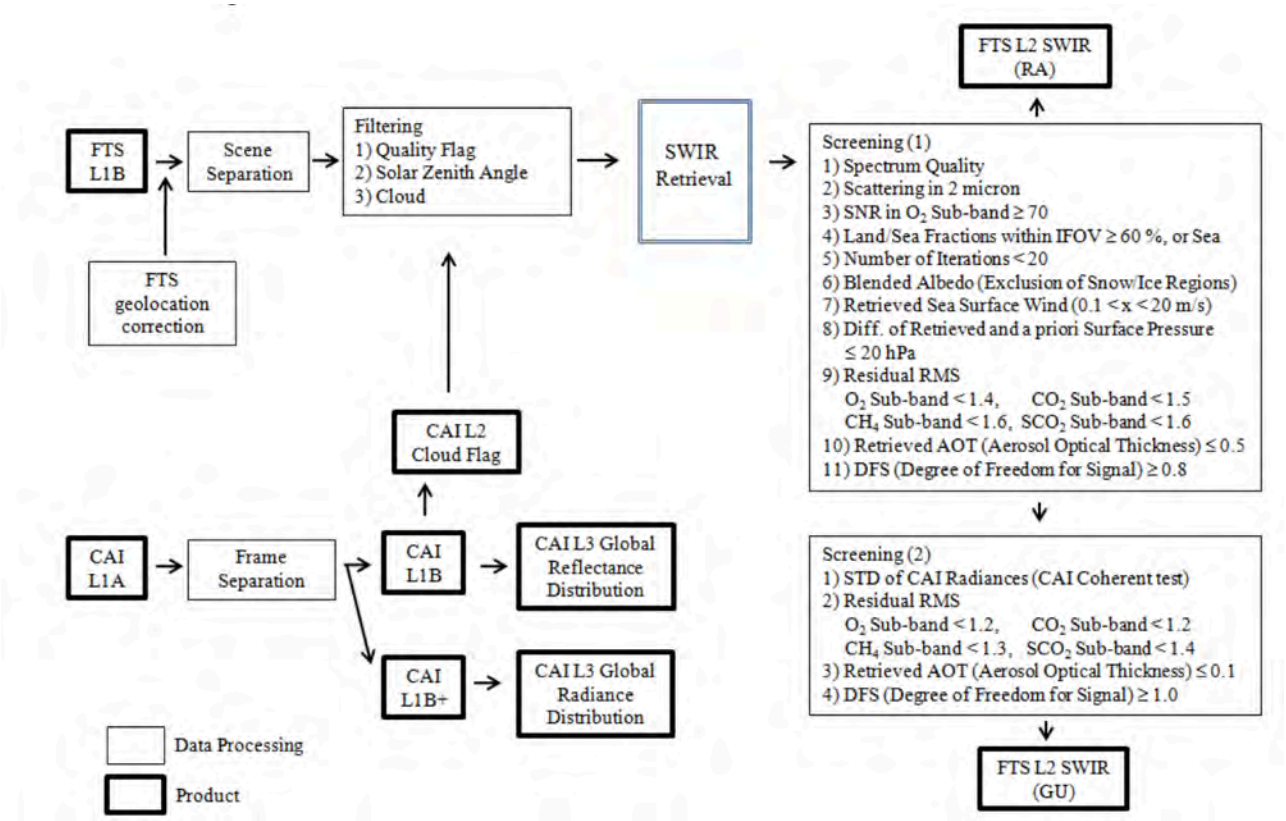

Figure 2.4-1 Processing Flow for FTS SWIR Level 2 CO_2 and CH_4 data products (Ver.02.2*)
https://data2.gosat.nies.go.jp/doc/documents/DataProcessingFlow_FTSSWIRL2_V02.2x_en.pdf

2.5 VALIDATION OF COLUMN CONCENTRATIONS DERIVED FROM SATELLITE SWIR DATA

To ensure the accuracy of the XCO_2 and XCH_4 products derived from satellite data, the satellite measurements must be accurately calibrated and the retrieved XCO_2 and XCH4 estimates must be validated against internationally-recognized standards. The instruments are calibrated both prior to launch and then while in orbit to quantify the spectral, radiometric, and geometric performance. Calibration is instrument specific and is not discussed further in this guidebook. To validate XCO_2 and XCH_4 estimates retrieved from satellite data (Level 2 or higher level products), these products are quantitatively evaluated using the data with higher quality and independently measured by other instruments. Here, the satellite data are often validated with ground-based and airborne in situ and remote sensing measurements of these gases.

The validation approach for column concentrations derived from satellite SWIR spectral data adopted by SCIAMACHY, GOSAT, and OCO-2 is to compare the XCO_2 and XCH_4 estimates retrieved from the satellite data with the column concentrations derived from ground-based SWIR spectral data collected by Total Carbon Column Observing Network (TCCON; Wunch et al. (2011)). TCCON is a network of ground-based high resolution solar-viewing Fourier transform spectrometers (FTS) deployed over a range of latitudes and longitudes (Figure 2.5-1).

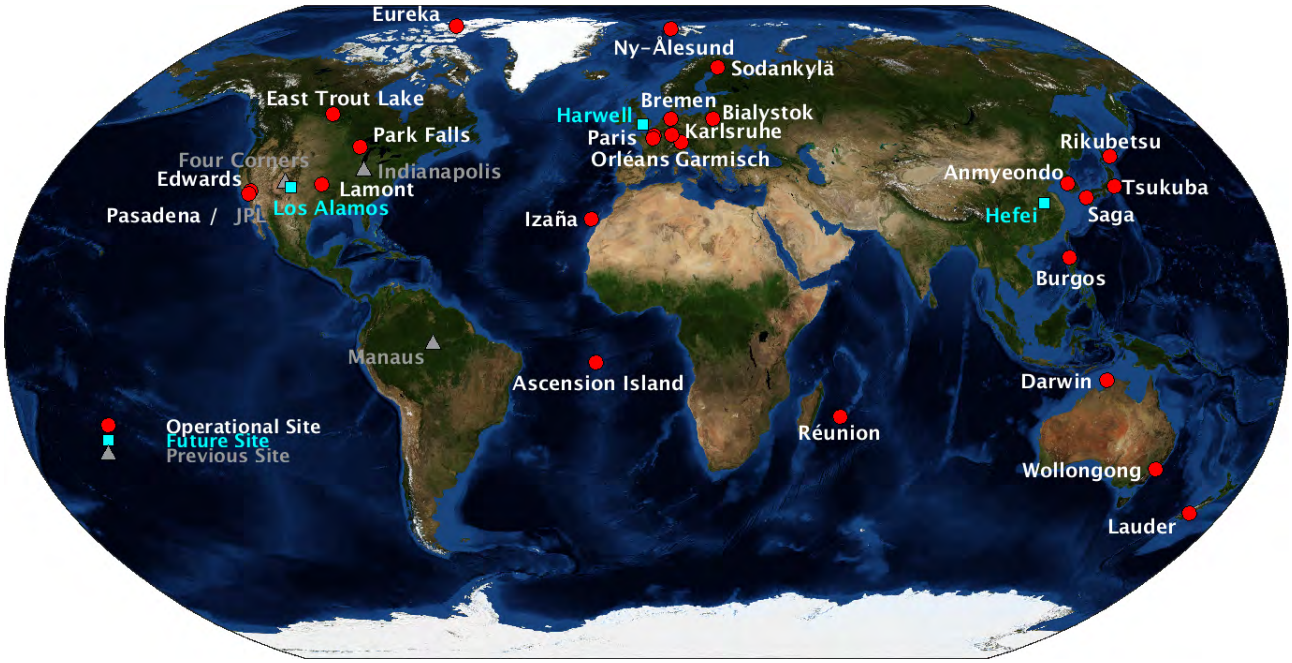

Figure 2.5-1. Locations of TCCON sites.
(http://tccondata.org/img/tccon_map.jpg)

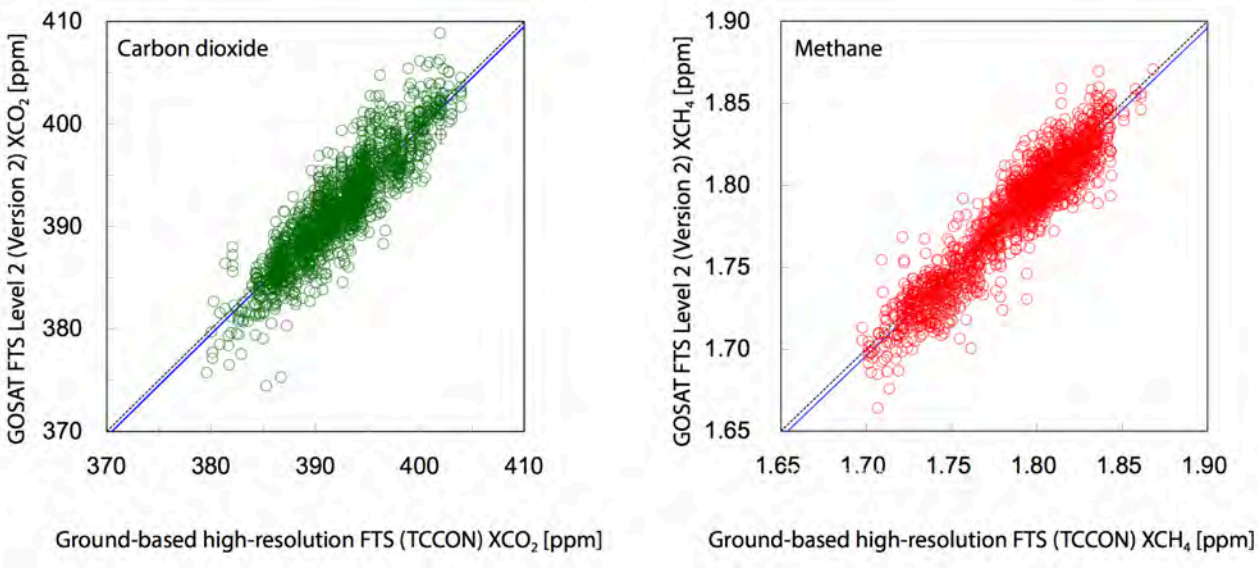

Figure 2.5-2. GOSAT FTS Level 2 products (Version 2) validation results with TCCON data: (left) XCO_2 and (right) XCH_4 (http://www.gosat.nies.go.jp/eng/gosat_leaflet_en.pdf)

For detailed results of GOSAT and OCO-2 validation activities, see Morino et al. (2011) and Yoshida et al. (2013) for GOSAT and Wunch et al. (2017) for OCO-2. According to Yoshida et al. (2013), the biases and the standard deviations of the GOSAT Level 2 products V02.00 are -1.48 and 2.09 ppm for XCO_2 and -5.9 and 12.6 ppb for XCH_4, respectively (Figure 2.5-2). According to Wunch et al. (2017), the absolute median differences and the RMS differences of OCO-2 XCO_2 are less than 0.4 ppm and less than 1.5 ppm, respectively. These values are interpreted as the accuracy and precision of the XCO_2 and XCH_4 satellite data. Biases in the retrieved concentration data can be reduced by empirical methods (e. g. Inoue et al., 2016) or through comparisons with outputs from atmospheric transfer models which calculate global gas concentration distribution.

3. SATELLITE OBSERVATIONS AND DATA APPLICATIONS, PART 2: USING SATELLITE OBSERVATIONS FOR EMISSION ESTIMATES AND COMPARISON TO EMISSION INVENTORIES

Introduction

Atmospheric measurements of GHGs can provide a useful additional constraint on emissions where bottom-up inventories are incomplete or inaccurate (Henne et al., 2016; Saunois et al., 2016). A number of techniques are employed for estimating fluxes from GHG concentration measurements. On the smallest scales, a mass balance approach can be used to estimate fluxes from concentration measurements collected upwind and downwind of a known emission source, with surface and airborne measurement campaigns (Karion et al., 2011; McKain et al., 2015; Zavala-Araiza at al., 2015). On larger scales, ranging from city to national and continental scale, inverse models of atmospheric transport and other methods, including inter-tracer correlation, are used to estimate the surface fluxes. Inverse models use an atmospheric tracer transport model to simulate GHG concentration at observation locations given some assumed surface fluxes. Surface flux optimization techniques are applied to provide the best fit between observed concentrations and simulations with an atmospheric transport model (Enting, 2002).

Similarly to ground based measurements, use of the satellite observations for anthropogenic GHG emission estimates can be divided into two approaches. Mass balance approaches are described in section 3.1, and inverse models are described in section 3.2.

3.1 Emission estimates based on analysis of concentration anomalies around emission sources

While ground-based in situ measurements can provide estimates of GHG concentrations at the surface that are both precise and accurate, these measurements are spatially sparse and often provide no information about atmospheric profile of these gases. In contrast, space based remote sensing observations provide estimates of the column-averaged GHG concentration with much greater spatial resolution and coverage, but these estimates are often less precise and accurate as the ground-based in situ measurements.

Accordingly, some emission estimate methods, that can be used successfully with ground based observations, are not directly applicable to satellite observations due to lower precision of the satellite retrievals and due to observing vertically integrated concentration, which dilutes sensitivity to GHG concentrations in the planetary boundary layer. In the cases where the GHG concentration gradients are small, the lower precision of the space based measurements can be compensated to some extent by accumulating a large number of lower precision measurements. This approach can be applied over an extended period of time to recover information about the long-term mean

concentration differences between clean regional background and observations made directly over the emission point and its plume (Schneising et al., 2008, 2011; Kort et al., 2012; Janardanan et al., 2016, 2017; Hakkarainen et al., 2016; Turner et al., 2016; Buchwitz et al., 2017 and others). Notably, some OCO-2 observations of power plant plumes (Nassar et al., 2017) can be analyzed to yield flux estimates without long-term averaging on an event basis, due to lower single sounding random errors and its smaller surface footprint allowing observations of narrow plumes of high CO_2 concentration.

A number of emission estimation methods relying on observations of the concentration enhancements around emission sources and their temporal trends have been developed over the past decade. Anthropogenic emissions of CO_2, CH_4, as well as NO_x, CO and other pollutants lead to buildup of the emitted tracers above the emission area and the transport of a high concentration plume downstream of the emission source (city, powerplant, etc.) by wind. Satellites observe increased column GHG concentration when the plume is in their observation footprint. The emission plumes or enhancements can be identified either by:

(1) long term averaging of the observed concentration (Schneising et al., 2008, 2011, 2014a; Buchwitz, et al., 2017),

(2) comparing with model simulations (Janardanan et al., 2016, 2017; Nassar et al., 2017), or

(3) by collocated observation of another pollution tracer such as NO_2 by OMI (Hakkarainen et al., 2016) and NH_3 by GOSAT TIR (Ross et al., 2013), or transport model simulation of pollution tracer CO (Parker et al., 2016).

Fig. 3.1-1 illustrates the three approaches for estimating enhancements listed above. Estimated concentration enhancements are related to emissions using either a simple wind-speed dependent model (Schneising et al., 2014a, Buchwitz, et al., 2017), or plume-resolving high-resolution transport model (Kort et al., 2012, Janardanan et al., 2016, 2017, Nassar et al., 2017). The following sections discuss details of these three approaches applied to delineating and quantifying GHG concentration enhancements and their relation to emissions.

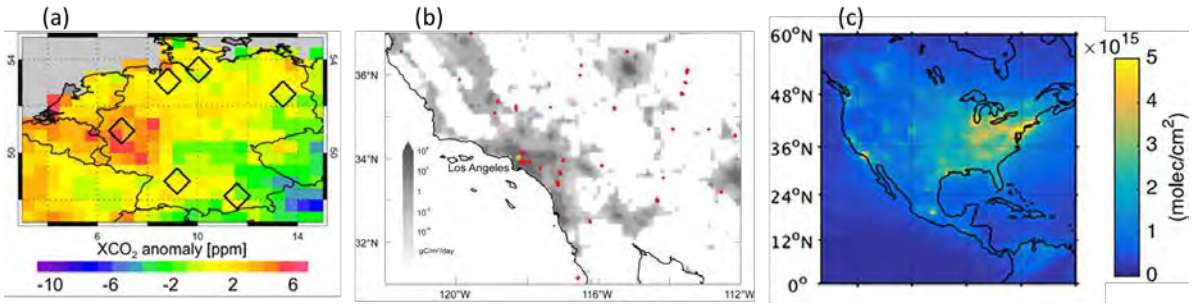

Fig. 3.1-1 Diagram showing three approaches to extracting XCO_2 anomalies from multiyear time series of satellite observations: (a) long term averaging of SCIAMACHY data over Western Europe, from (Scheising et al., 2008); (b) GOSAT observation locations (in red) used to simulate XCO_2 using high resolution transport model and CO_2 emissions (in grey), as in Janardanan et al., (2016); (c) OMI observations of NO_2, that provide information on "polluted" vs "clean" air for filtering OCO-2 observations (Hakkarainen et al., 2016).

3.1.1 Long-term averaging

As found by Schneising et al., (2008) when analyzing SCIAMACHY XCO_2 retrievals for a period of 3 years (2003-2005), both the measurement noise and the noise introduced as the CO_2 from other sources is transported over the source of interest by the winds is suppressed by averaging, and local concentration anomalies become visible, coinciding geographically with areas of strong surface emissions. Long term averages of SCIAMACHY measurements of methane were even able to detect trends in local concentration anomalies over emitting areas (Schneising et al., 2014a).

Applying long-term averaging is a convenient way to extract emission-related concentration anomalies, as it doesn't require transport modeling or a proxy tracer observation. However, the quantitative value of the derived anomalies for the emission estimates is limited, as averaging sums up the enhancements due to emission contributions from different wind directions and at different wind speeds. Long-term averaging was shown to work for sensors like SCIAMACHY or OMI, which provide coarse wide swath observations, resulting in almost continuous observation coverage. In the case of narrow swath instruments, like OCO-2, or coarse footprint sampling observations, as in the case of GOSAT, a modified approach to long-term averaging will be needed.

3.1.2 High resolution transport modeling

Janardanan et al., (2016, 2017), and Heymann et al., (2017) used high resolution transport models to simulate each GHG plume transported by wind from strong emission sources, while Nassar et al., (2017) used simple Gaussian plume model for this purpose. In addition to filtering the observations by threshold value of simulated enhancements, Janardanan et al. (2016, 2017) applied binned averaging of the observed enhancements that resulted in a large reduction in observation

noise, making the relationship between modeled and observed enhancements visibly close to linear. In this approach, a simple ratio of the mean observed to simulated enhancements or a regression slope value is used as a correction factor for adjusting the emission intensities provided by an emission inventory to match the observed concentrations.

Using transport modeling has the merit of allowing both extraction of the concentration anomalies and taking wind speed into account when relating the concentration anomalies to surface emissions. However, there are also multiple difficulties of applying the local scale transport modeling, including:

(1) uncertainties related to defining a clean background;
(2) a need for accurate high resolution wind data, resolving coastal air circulations and topographic effects;
(3) correlated errors due to aerosol loading leading to retrieval biases.

3.1.3 Use of the collocated observations of another tracer of atmospheric pollution

Use of high resolution transport modeling in backward transport mode (Janardanan et al., 2016, 2017) requires a large volume of computations in cases of satellite instruments that produce a large amount of data (like OCO-2). In that case, collocated observations of another tracer can be applied to detect the observations influenced by GHG emissions and separate them from observations made in the clean air.

In Nassar et al. (2017), OCO-2 observations from direct overpasses or close flybys of individual coal-burning power plants were fit to simulations using a vertically-integrated Gaussian plume model. This required conversion of the OCO-2 observations to XCO_2 enhancements relative to the background and converting plume model enhancements from gC/m^2 to ppm. Although the approach avoids simple averaging of the data so that it can utilize gradients within the emission plume, each emission estimate was based on from 17 to 167 (mean of 66) OCO-2 footprints from the plume and larger numbers for the background (126-489, mean of 310). An associated method for quantifying emission estimate uncertainties accounts for the impact of wind speed uncertainty, background uncertainties, observation enhancement uncertainties and potential interfering emission sources. More details on this study are given in the case study section of the Guidebook.

Hakkarainen et al. (2016) constructed CO_2 anomaly maps from OCO-2 data, and then used NO_2 observations from OMI to determine whether these anomalies were correlated with fossil fuel or biomass burning sources. Ross et al. (2013) used GOSAT TIR NH_3 observations to identify surface GOSAT footprints influenced by biomass burning, and proceeded with using the data for deriving the ratio of CH_4 to CO_2 emissions by biomass burning. Parker et al. (2016) used simulations of CO transport driven by biomass burning emissions to detect influences of biomass burning in GOSAT footprints, also for deriving ratio of CH_4 to CO_2 emissions.

Using a reference tracer of atmospheric pollution was shown to be sometimes more accurate than high resolution transport modeling for discriminating between polluted versus clean background air (Oney et al., 2017). Limitations are also present: (1) although the method is good for extracting anomalies related to combustion, other processes (fugitive emissions of methane) correlate to combustion intensity (NO_2, CO) only at much larger scales; (2) the emission estimates depend on uncertainty of the reference tracer emissions, and accounting for chemical transformation of the reference tracer.

3.2 Anthropogenic GHG emission estimates based on inverse modeling

Inverse models combine information about the atmospheric transport with observations of GHG concentrations, and adjust the surface fluxes to produce a good fit of the transport model simulation to the observations. Inverse models have been used along with ground based GHG observations to regional and national scale anthropogenic non-CO_2 GHG emission estimates (Stohl et al., 2009; Manning et al., 2011; Miller et al., 2013; Henne et al., 2016 and others) and city-scale CO_2 emissions (Brioude et al., 2013; Breon et al., 2015; Lauvaux, et al., 2016). In flux inversion experiments that use sparse, but accurate surface GHG measurements, the number of observations is critical as the strength of the observational constraint for estimated fluxes is proportional to the number of available observations and inversely proportional to the uncertainty of a single observation (Enting, 2002). Thus, as pointed out by Rayner and O'Brien, (2001), satellite observations available in large volume over regions underrepresented by the surface network are useful for surface flux estimates, even when taken with a precision lower than that of the ground based observations. Inverse modeling techniques that were developed for estimating surface fluxes with ground-based observations (Rayner et al., 1999; Rodenbeck et al., 2003) are being applied to satellite observations as well (Meirink et al., 2008; Maksyutov et al., 2013; Houweling et al., 2015; Turner et al., 2015 and others). There are also several reviews of methods which have been tested and applied to use of the GHG concentration observations for emission estimates at local and regional scale (Jacob et al., 2016, Streets et al., 2013).

An inverse model relies on an atmospheric transport model to simulate the concentrations of emitted tracers at the observation locations with emission intensity fields, and tries to find a surface emission field that provides a best match between simulated and observed data. Due to the limited spatial and temporal resolution of the winds and other limitations of the atmospheric transport models, the mismatch between observed and optimized data can be larger than the GHG measurement errors.

A brief outline of the inverse modeling approach as mathematical formulation of the flux optimization problem is given in Section 4.6.2 of this Guidebook, while more detailed description that can be found in (Enting, 2002) and other introductory texts on inverse modeling.

Depending on observation data available for constraining the target flux category, the uncertainties of the inverse model estimates can be larger than those of inventory, as it is often the case for anthropogenic CO_2 emissions, thus application of the inverse modeling is only justified when the uncertainty of the inventory is larger or comparable to the uncertainty of the inverse model estimates. The uncertainties of anthropogenic emission inventories vary widely depending on target tracer, region, country and source category. There are also difficulties in estimating the uncertainty of the bottom-up inventory. One example of significant discrepancies between emission inventories and inverse model estimates is related to recent US emissions in the oil and gas category (Miller and Michalak, 2017). The main difficulty leading to uncertainty of the emission inventory for some species is large variability of the emission factors. As Beusse et al., (2014) mentioned, the uncertainty of methane emissions factors for US gas pipelines estimated by US Environment Protection Agency (EPA) study was 65%. For CO_2, the uncertainty of anthropogenic annual CO_2 emission inventories is rather low at the country scale in most cases (Rypdal et al., 2005), however, it can still be high for emerging economies which now represent some of the highest emitting nations and a larger share of global CO_2 emissions. Furthermore, CO_2 emission uncertainties are larger for smaller space and time scales, which makes top-down estimates less relevant for national reporting, but more relevant for the implementation of NDCs and for countries to understand the effectiveness of their efforts to achieve their NDCs and track their own progress.

3.2.1 Application of the inverse model emission estimates for comparison with national inventories

Use of satellite observations in inversion is in the experimental stage, due to multiple technical challenges of producing the high-quality concentration retrievals from the satellite-observed spectra. However, there are several promising results. A number of methane inverse modeling studies were conducted using (mostly) GOSAT and SCIAMACHY satellite data (Fraser et al., 2013; Alexe et al., 2015; Pandey et al., 2017; Turner et al., 2015; Cressot et al., 2014) and several of those have been intercompared in a Global Carbon Project CH_4 (GCP-CH_4) study by Saunois et al., (2016). A valuable outcome of the comparisons performed by Saunois et al., (2016), Bruhwiler et al., (2017) and Cressot et al. (2014) is that they have shown a general consistency between ground-based data inversions and satellite-based data inversions in terms of the estimated emissions for important emission regions such as East Asia and North America. The GCP-CH_4 study results for 2012 show that the spread (standard deviation) of anthropogenic methane emissions estimates between different inverse models for large regions (temperate North America, boreal North America, Europe, Central Asia and Japan, China, Russia) is between 11 to 25 % of the multi-model average for each region, and GOSAT-based estimates are within the range of the estimates. Accordingly, the inverse model estimates based on space-based observations can be considered as an additional source of

data for national inventory comparisons alongside with estimates based on surface observation data.

It should be noted that inverse models have biases dependent on design of the transport model, and the emission estimates are sensitive to underlying transport model biases. The differences are apparent when estimates for the same region and time period are compared (Houweling et al., 2015; Saunois et al., 2016). On the other hand, the differences become smaller when interannual flux variability and temporal trends are concerned, as shown recently by analysing the trends in methane emission estimates by several inverse models included in the GCP-CH_4 study for North America (Bruhwiler et al., 2017). Patra et al., (2016) and Saeki and Patra, (2017) applied inverse modeling of CH_4 and CO_2 fluxes over East Asia for checking the inventory time series consistency. Patra et al., (2016) concluded that the growth rate in East Asian emissions of CH_4 was likely to be overestimated by bottom-up inventories.

Publicly available inverse model estimates for CH_4 emissions based on satellite and ground-based measurements are provided by inverse model products, including the global inversion product from the Copernicus Atmospheric Monitoring Service[1] (CAMS), (Bergamaschi et al., 2013), NASA CMS-flux product for North America, (Turner and Jacob, 2016) and GOSAT Level 4A product (CH_4) (Saito et al., 2016). Several institutions, such as Laboratoire des Sciences du Climat et de l'Environnement (LSCE), Max Planck Institute for Biogeochemistry (MPI BGC), Harvard University and others also make their emission estimates at the global scale based on satellite data and make their gridded flux data available upon request.

Although the satellite-based global products are currently provided at coarse resolution (2-3 degrees), an upgrade to higher resolution is foreseen, based on recently developed regional zoom approaches, like those based on the NAME model (Ganesan et al., 2017; Manning et al., 2011), CHIMERE (Broquet et al., 2011) or Carbontracker-Lagrange (He et al, 2017).

To compare national inventory to publicly available inverse modeling products introduced above, one should implement following steps:

1. Check if the inverse modeling product confirms to at least 3 criteria:
   (1) the product is checked for probable errors and inconsistencies via comparison to other inverse modeling estimates (see Saunois et al., 2016, Bruhwiler et al., 2017);
   (2) observations impose strong enough constraint on estimated fluxes, the inverse model uses several observation sites over the country and, possibly, good satellite data coverage, sufficient to reduce flux uncertainty by 30-50%;
   (3) the estimated inverse model flux uncertainty is less than uncertainty of the national inventory.
2. Based on the inverse modelling data available at the time of inventory report preparation, select available time periods overlapping between inventory data and inverse model results. Download gridded emission data files, file format descriptions and release notes.

3. Remapping from gridded data to country boundaries. Calculate area fraction of the national land area in each grid cell of the emission data grid (fractional overlap between data grid cell boundaries and nation borders). Use area fraction to calculate national total emission for each time period (usually available at monthly time step), by summing grid emissions multiplied by fraction of national land area. Derive national total for each year by summing the monthly total emissions.
4. Remap emission uncertainty, in the case all the data required for regional emission uncertainty estimates is provided together with inverse modelling results.
5. When the number of available inverse modelling products is greater than one, remap to national total for each year for all the available products. It is useful to include in the comparison national total estimates with each available inverse modelling product, as in (Bergamaschi et al., 2018).

The above step-by-step guidance is illustrated in the following diagram (Fig. 3.2-1)

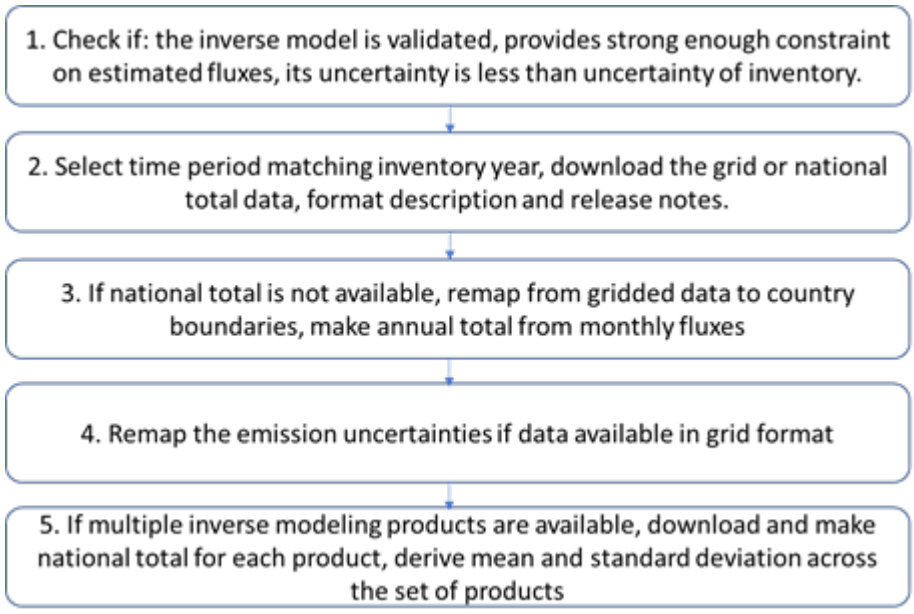

Fig. 3.2-1 Step by step procedure for extracting the national (reginal) total emissions from inverse modeling products.

Ready-made estimates for several countries, such as US (conterminous), Russia and China for year 2012 are prepared based on Global Carbon Project CH_4 inverse model estimates (Saunois et al. 2016) using a procedure that is described above and are published on the Environmental System Science Data Infrastructure for a Virtual Ecosystem (ESS-DIVE) web site (Global Methane Budget 2000-2012, 2016).

Useful examples of comparison between national emissions estimated by inventory and inverse

model are given by Bruhwiler et al. (2017) and Turner et al. (2015), both made for USA. Separate estimates of the sector-specific anthropogenic (oil and gas, agriculture and waste) and natural (wetlands) emissions is still a problem even for recent high resolution regional inverse modeling studies (Bergamaschi et al., 2018). Nevertheless, Turner et al. (2015) used GOSAT observations and a transport model with high resolution zooming over North America to project likely underestimation of the anthropogenic emissions in US methane emission inventory. In their case, distinguishing between natural and anthropogenic sources is assisted by geographical separation between natural sources (wetlands in the North) and growing oil and gas emissions in the South. More details on the study by Turner et al. (2015) are also given in the case study section 4.6 of this Guidebook. An estimate of the Indian national total emissions of methane was made by Ganesan et al., (2017) using high resolution regional inverse model and combination of the ground based observations and GOSAT data. They have concluded that atmospheric observation data support the nationally reported emissions in terms of both trend and amount.

[1] http://atmosphere.copernicus.eu/documentation-supplementary-products#greengas-fluxes

4. CASE STUDIES

In this chapter, several case studies in which greenhouse gas inventories are compared with the estimates from satellite-based or ground-based concentration measurements are described. Target gases, gas concentration data sources, and methods in each section are summarized in Table 4.0-1.

Table 4.0-1. Summary of case studies in Chapter 4.

Section	Target gas	Gas concentration data source	Method
4-1	CO_2	SCIAMACHY	Concentration enhancement
4-2	CO_2	OCO-2	Concentration enhancement
4-3	CO_2 and CH_4	GOSAT and SCIAMACHY	Concentration enhancement
4-4	CO_2 and CH_4	GOSAT	Concentration enhancement
4-5	CH_4	GOSAT and SCIAMACHY	Concentration enhancement
4-6	CH_4	GOSAT	Inverse modeling
4-7	CO_2	GLOVALVIEW (flask)	Inverse modeling
4-8	CH_4	WDCGG and GOSAT	Inverse modeling
4-9	CO_2	OCO-2	Concentration enhancement

4.1 Anthropogenic CO_2 emission trends from SCIAMACHY/ENVISAT and comparison with EDGAR

M. Buchwitz[1], M. Reuter[1], O. Schneising-Weigel[1], H. Bovensmann[1], and J. P. Burrows[1]

1) Institute of Environmental Physics (IUP), University of Bremen, Germany

4.1.1 Introduction

SCanning Imaging Absorption spectroMeter for Atmospheric CHartographY (SCIAMACHY) (Burrows et al., 1995; Bovensmann et al., 1999) onboard of the European environmental satellite ENVISAT was operational from March 2002 to April 2012. SCIAMACHY was a passive remote sensing spectrometer observing backscattered, reflected, transmitted or emitted radiation from the atmosphere and Earth's surface, in the wavelength range between 240 and 2380 nm. The spatial resolution depends on spectral region but was typically 30 km along track and 60 km across track. Global coverage at the equator was achieved after six days (swath width 960 km; nominal measurement sequence: 50% nadir (downlooking) and 50% limb (scanning the atmosphere while looking to the Earth's horizon and above)).

For the retrieval of column-averaged dry-air mole fractions of carbon dioxide (CO_2), i.e., XCO_2, two spectral regions have been used: the 1.6 μm region containing CO_2 absorption lines and the 0.76 μm spectral region covering the oxygen (O_2) A-band.

The retrieved XCO_2 (e.g., Buchwitz et al., 2000, 2015, 2016; Schneising et al., 2008, 2011; Reuter et al., 2010, 2011; Heymann et al, 2015) has been used to address important scientific issues related to the natural sources and sinks of atmospheric CO_2 (e.g., Reuter et al., 2014a, 2017; Schneising et al., 2014b).

In the following results from studies related to anthropogenic CO_2 emissions, which have been published in the peer-reviewed scientific literature (Schneising et al., 2008, 2013; Reuter et al., 2014b), are summarized.

4.1.2 Data

4.1.2.1 GHG Concentration Data

Schneising et al., 2008, analyzed SCIAMACHY year 2003-2005 XCO_2 retrievals. For validation the XCO_2 product of the Total Carbon Column Observing Network (TCCON) (Wunch et al., 2011) has been used. Furthermore, they used atmospheric CO_2 fields from NOAA's CO_2-assimilation system CarbonTracker (Peters et al., 2007).

Schneising et al., 2013, used SCIAMACHY XCO_2 retrievals covering the time period 2003-2009 and CarbonTracker CO_2 fields (Peters et al., 2007).

Reuter et al., 2014b, used SCIAMACHY XCO_2 retrievals from the time period 2003-2011.

4.1.2.2 Other Data

Schneising et al., 2008, used for comparison with the satellite XCO_2 retrievals population density (CIESIN/CIAT, 2005) and EDGAR anthropogenic CO_2 emissions (EDGAR 3.2 Fast Track 2000 dataset (32FT2000), Olivier et al., 2005). Furthermore, MODIS/Terra aerosol optical depth has been used (Level 3 collection 5 product obtained from http://modis-atmos.gsfc.nasa.gov/) and subvisual cirrus cloud retrievals from E. Martins, LMD/IPSL, Palaiseau, France.

Schneising et al., 2013, used for comparison EDGAR anthropogenic CO_2 emissions (version 4.2, Olivier et al., 2012). In addition, an aerosol optical depth data set based on MODIS from the European GEMS (Global and regional Earth-system Monitoring using Satellite and in-situ data) project has been used (obtained from http://data-portal.ecmwf.int/data/d/gems reanalysis/).

EDGAR version 4.2 has also been used by Reuter et al., 2014b. In addition, SCIAMACHY NO_2 vertical column retrievals have been used.

4.1.3 Methods

4.1.3.1 Outline

Different methods have been used in each of the three publications. These methods are shortly described in the following sub-sections.

4.1.3.2 Methodology used by Schneising et al., 2008

The main goal of Schneising et al., 2008, was to demonstrate that regionally elevated CO_2 over major anthropogenic source regions can be detected from space. Focus was on the Rhine-Ruhr area in western central Europe but other regions have also been studied, e.g., the US East Coast and the region around Tokyo in Japan. To eliminate XCO_2 variations not originating from anthropogenic CO_2 emissions, in particular variations due to uptake and release of CO_2 by the terrestrial biosphere, and to reduce noise, the satellite XCO_2 retrievals have been averaged over all three years (2003-2005) using a spatial grid of 0.5^ox0.5^o. The resulting XCO_2 maps have been compared with population density and EDGAR anthropogenic CO_2 emissions. In order to make sure that the observed elevated satellite-derived XCO_2 is not significantly affect by aerosols or thin clouds, satellite aerosol optical depth and information on subvisual cirrus clouds have been used. In addition, also simulated retrievals have been carried out as part of the error analysis. For details please see Schneising et al., 2008.

4.1.3.3 Methodology used by Schneising et al, 2013

The method used by Schneising et al., 2013, is similar as the method used by Schneising et al., 2008. The main differences are (i) the use of a longer time period, (ii) the aim to obtain information on emission trends, and (iii) to achieve a more quantitative comparison with EDGAR anthropogenic

CO_2 emissions assuming that a regional relative CO_2 emission enhancement corresponds to the same relative regional XCO_2 enhancement over the source region of interest. For details please see Schneising et al., 2013.

4.1.3.4 Methodology used by Reuter et al, 2014b

The method of Reuter et al., 2014b, differs significantly from the methods of Schneising et al., 2008 and 2013. Reuter et al., 2014b, took advantage of the fact that SCIAMACHY provides retrievals of NO_2 vertical columns in addition to XCO_2. They used satellite-derived NO_2 as a tracer for anthropogenic emissions and calculated regional anomalies ΔXCO_2 and ΔNO_2 from collocated SCIAMACHY XCO_2 and NO_2 retrievals. They found an approximately linear relationship between satellite-derived ΔXCO_2 and ΔNO_2 and interpreted the slope as a (regionally dependent) conversion factor allowing the use of NO_2 as a proxy for expected regional XCO_2 enhancements from nearby anthropogenic emissions ("XCO_2^e"). XCO_2^e is an estimate of the expectation value of the XCO_2 enhancement resulting from the source (or sources) causing a measured NO_2 level. Using this method, they obtained emission trends and CO_2-to-NOx emission ratios, which were compared with EDGAR. A very detailed error analysis is also presented in Reuter et al., 2014b, which had been carried out in order to obtain reliable uncertainty estimates. For details please see Reuter et al., 2014b.

4.1.4 Case Study Results

In the following three sub-sections the main results from the three case studies are shortly presented and summarized.

4.1.4.1 Results obtained by Schneising et al., 2008

The main goal of the study of Schneising et al., 2008, was to find out if regionally elevated CO_2 over major anthropogenic source regions can be detected from space. Their results can be summarized follows: When averaging the SCIAMACHY XCO_2 retrievals over the time period 2003-2005 the resulting map for western central Europe (Fig. 4.1-1) shows elevated CO_2 over the highly populated region of western central Germany and parts of the Netherlands and Belgium ("Rhine-Ruhr area"). They found that the spatial pattern is reasonably well correlated with population density and EDGAR anthropogenic CO_2 emissions (see Fig. 4.1-2). Note that a perfect correlation cannot be expected due to atmospheric transport and sparse sampling of the satellite data. On average they found a regional enhancement of 2.7 ppm over this region (XCO_2 average in red rectangle minus green rectangle in Fig. 4.1-2). The potential contribution to this enhancement from regionally elevated aerosols and sparse sampling of the satellite data was conservatively estimated to 1-1.5 ppm. They found similar results also for other major anthropogenic source regions such as

the US East Coast and the region around Tokyo in Japan. Overall, they concluded that their findings indicate that regionally elevated CO_2 arising from regional anthropogenic CO_2 emissions can potentially be detected from space.

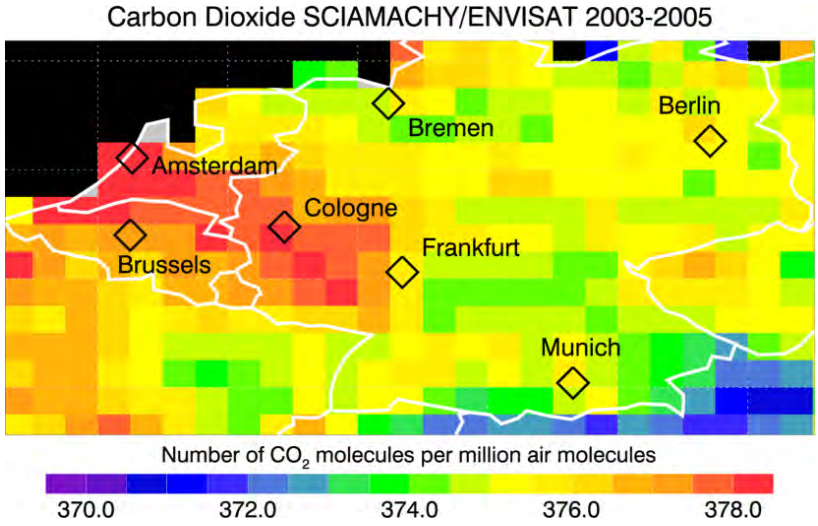

Figure 4.1-1. Elevated CO_2 over western central Europe's major anthropogenic source region, the Rhine-Ruhr area, covering parts of Germany, the Netherlands and Belgium. Adapted from Schneising et al., 2008 (see Fig. 4.1-2 for their original figure).

4.1.4.2 Results obtained by Schneising et al., 2013

The main goal of the study of Schneising et al., 2013, was to obtain more quantitative results compared to the predecessor study presented in Schneising et al., 2008. A summary of their main results is shown in Fig. 4.1-3. By subtracting satellite retrieved XCO_2 background values from those retrieved over urban areas significant CO_2 enhancements for several anthropogenic source regions have been found, namely 1.3±0.7 ppm for the Rhine-Ruhr metropolitan region and the Benelux, 1.1±0.5 ppm for the East Coast of the United States, and 2.4±0.9 ppm for the Yangtze River Delta area in China. The order of magnitude of the enhancements is in agreement with what is expected for anthropogenic CO_2 signals. The larger standard deviation of the retrieved Yangtze River Delta enhancement is due to a distinct positive trend of 0.3±0.2 ppm/yr, which is quantitatively consistent with anthropogenic emissions from the Emission Database for Global Atmospheric Research (EDGAR) in terms of percentage increase per year (see Fig. 4.1-3 bottom right). The obtained trends over Central Europe and the US East Coast also agree with EDGAR within the (quite large) uncertainty of the satellite-derived trends.

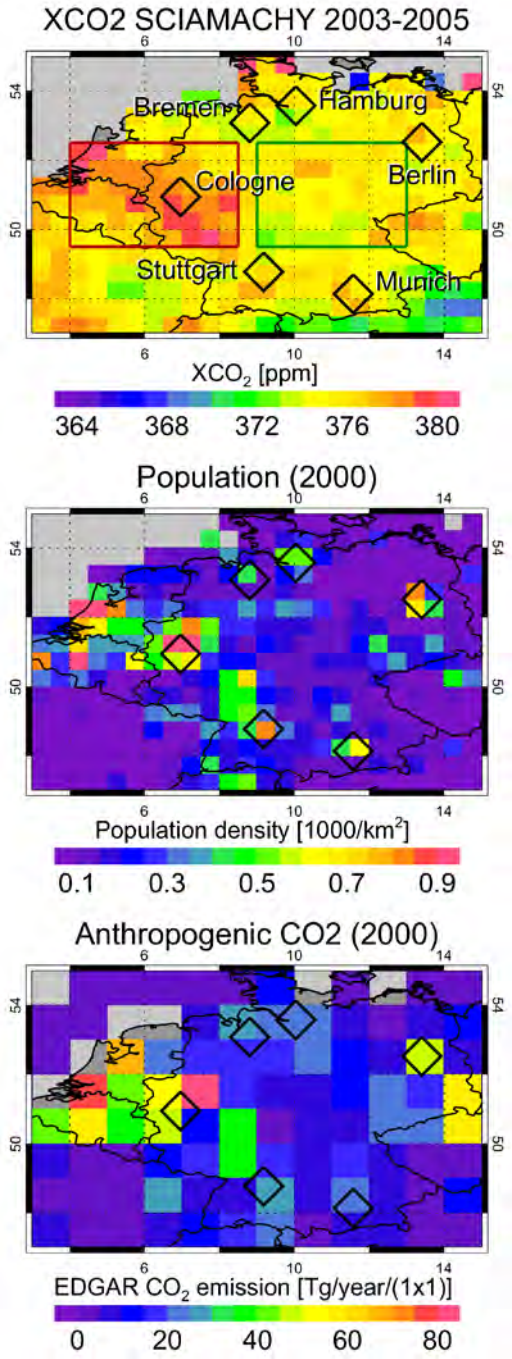

Figure 4.1-2. Top: SCIAMACHY XCO_2 during 2003-2005 over western Central Europe. Middle: Population density. Bottom: EDGAR anthropogenic CO_2 emissions. From Schneising et al., 2008 (their Fig. 17).

4.1.4.3 Results obtained by Reuter et al., 2014b

Reuter et al., 2014b, analyzed simultaneous and co-located satellite retrievals from SCIAMACHY of the column-average dry-air mole fraction of CO_2, i.e., XCO_2, and NO_2 vertical columns for the years 2003–2011 to provide top-down estimates of emission trends and CO_2 to NOx emission ratios. Their analysis (Figs. 4.1-3 and 4.1-4) showed that the CO_2-to-NOx emission ratio has increased by 4.2+/-1.7%/yr in East Asia. In this region, they found a large positive trend of

CO_2 emissions (9.8+/-1.7%/yr), which was largely attribute to the growing Chinese economy. This trend exceeds the positive trend of NOx emissions (5.8+/-0.9%/yr). Their findings suggest that the recently installed and renewed technology in East Asia, such as power plants, transportation, etc., is cleaner in terms of NOx emissions than the old infrastructure, and roughly matches relative emission levels in North America and Europe. The satellite-derived trends over North America and Europe were negative and in agreement with EDGAR (Fig. 4.1-4).

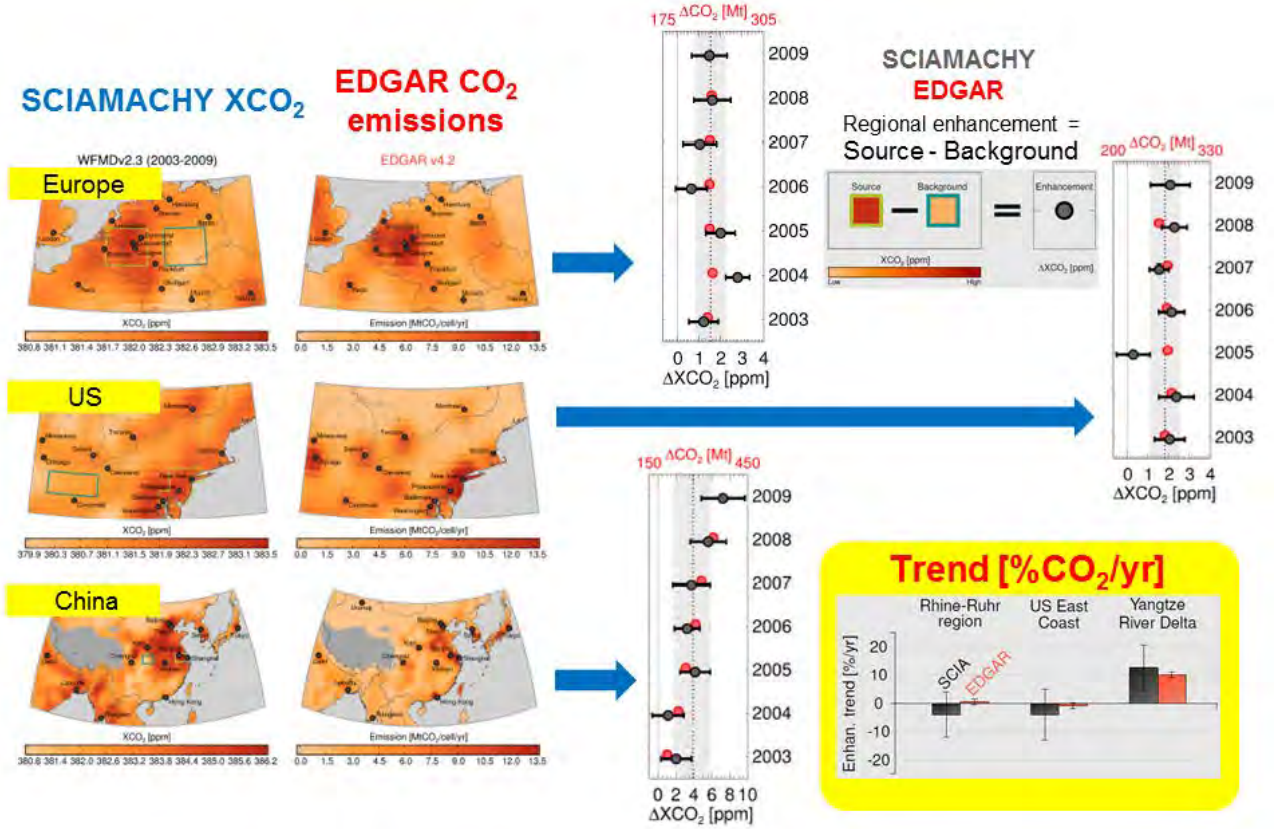

Figure 4.1-3. Overview of the main results of Schneising et al., 2013. Left: Comparison of SCIAMACHY XCO_2 during 2003-2009 with EDGAR version 4.2 anthropogenic CO_2 emissions over the three major source regions western central Europe, US East Coast and China. The SCIAMACHY XCO_2 maps have been used to compute annual XCO_2 enhancements (ΔXCO_2) by computing source region minus background region differences (see top right). The main result in terms of relative (percentage) enhancement trends of the satellite regional enhancement and the corresponding EDGAR enhancements are shown in the bottom right yellow rectangle.

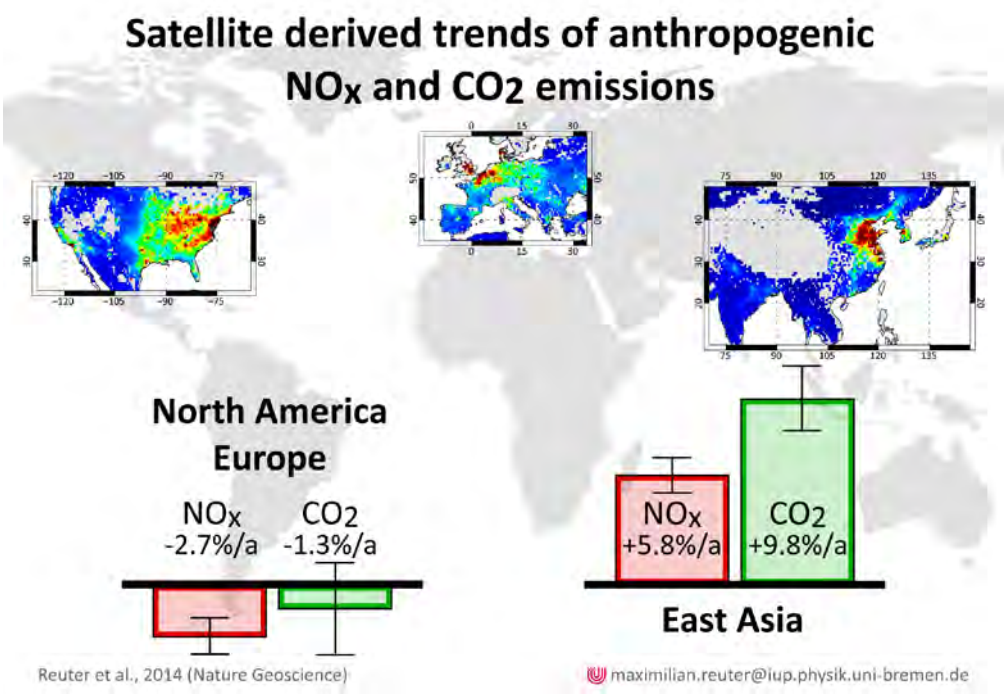

Figure 4.1-4. Overview of the main results of Reuter et al., 2014b. The maps show SCIAMACHY NO_2 converted to XCO_2 using regionally dependent conversion factors obtained from co-located SCIAMACHY XCO_2 and NO_2 column correlations and a filtering method to select ground pixels affected by near-by anthropogenic sources. The histograms show derived emission trends for NOx (red) and CO_2 (green) over the source regions North America / Europe (left) and East Asia (right). Adapted from Reuter et al., 2014b (see Fig. 4.1-5 for the original figure).

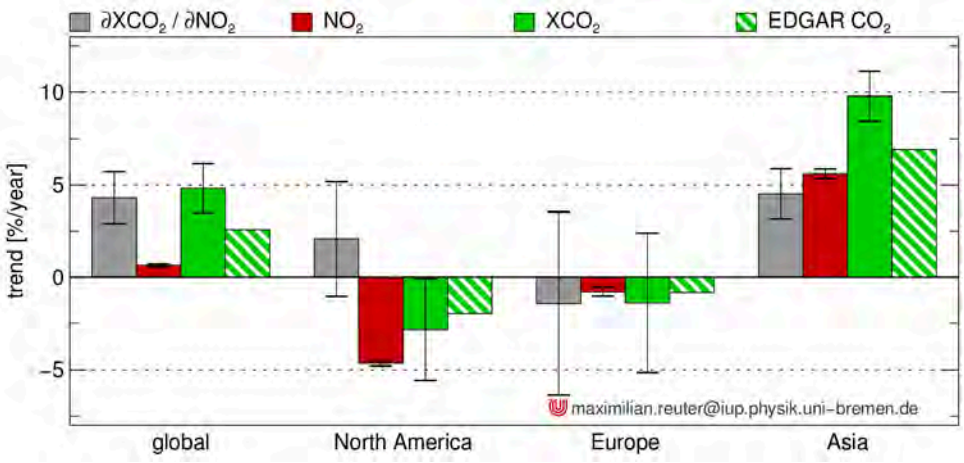

Figure 4.1-5. Trends of CO_2-to-NOx emission ratios (grey), tropospheric NO_2 emissions (red), XCO_2 enhancements (green) and corresponding emission trends from EDGAR (green-white striped). From Reuter et al., 2014b (their Fig. 3). For details see Reuter et al., 2014b.

4.2 Direct space-based Observations of Anthropogenic CO_2 Emission Areas: Global XCO_2 Anomalies

Janne Hakkarainen[1], Iolanda Ialongo[1], and Johanna Tamminen[1]

1) Finnish Meteorological Institute, Earth Observation, Helsinki, Finland

4.2.1 Introduction

Over the past two decades, spaceborne measurements of short-lived air pollutants (such as nitrogen dioxide NO_2 and sulfur dioxide SO_2) have revolutionized the way we monitor atmospheric composition, providing more and more accurate information on the pollution levels on the global scale. In comparison to these short-lived air pollutants that are detected close to the emission sources, the growing trend, strong seasonality, long lifetime, and large atmospheric background, significantly complicate the analysis of the anthropogenic CO_2 emissions from space. This is why most studies employ auxiliary data from models, emission inventories, or other proxies in order to identify anthropogenic CO_2 emission areas from satellite-based CO_2 columns.

Direct methods, i.e. methods that are based on direct usage of space-based observations and not on atmospheric modeling, have proven to have several desirable properties for example in air quality applications. For example direct methods can reveal discrepancies between emission inventories and identify missing sources, as seen e.g. for NO_2 and SO_2 [McLinden et al., 2016] and for methane [Kort et al., 2014]. Superior spatial detail can also be reached from space-based observations, as many inversion methods are based on scaling pre-described *a priori* fields. A great challenge in direct methods, however, is to translate concentration information to emissions.

This section summarizes a recent study [Hakkarainen et al., 2016] that presents a direct observation of anthropogenic CO_2 from Orbiting Carbon Observatory-2 (OCO-2). The study proposes a novel methodology to detect anthropogenic CO_2 emission areas, solely based on spaceborne CO_2 measurements. The fundamental idea is to average-out the CO_2 transport and calculate long-term averages of CO_2 anomalies. These anomalies are obtained by deseasonalizing and detrending the data. The key is to use the observations themselves by removing the regional daily median values. For comparison, OMI (Ozone Monitoring Instrument) NO_2 tropospheric columns are used as an independent tracer of atmospheric pollution and CO_2 and NO_2 information are combined via cluster analysis. The results are also compared with existing anthropogenic CO_2 emission inventories.

4.2.2 Data

The column-averaged dry air mole fraction of CO_2 (XCO_2) data from Orbiting Carbon Observatory-2 (OCO-2) are used in the analysis. The methodology is also applicable to the Greenhouse gases Observing SATellite (GOSAT) data, and this option will be exploited in more

detail in future studies.

4.2.2.1 OCO-2 Data

Recently, measurements of column-averaged dry air mole fraction of CO_2 (XCO_2) have become available from the Orbiting Carbon Observatory-2 (OCO-2) [Crisp et al., 2004]. The instrument provides measurements with eight 2.25 km long footprints along a narrow (0.4 to 1.29 km) swath [Crisp et al., 2008]. The ACOS (Atmospheric CO_2 Observations from Space) retrieval algorithm is used to derive XCO_2 [O'Dell et al., 2012]. The study uses the version 7 reprocessed lite files including bias corrected XCO_2 data available from September 2014 to April 2016. The data have been screened using quality flags set to zero and warning levels smaller than 15.

4.2.2.2 Auxiliary Data

The NO_2 tropospheric column measurements from the Ozone Monitoring Instrument (OMI) are used in the analysis [Levelt et al., 2006]. OMI is a Dutch-Finnish instrument operating on board NASA's Aura satellite since 2004. OMI measures solar backscattered light in the UV-visible spectral region with spatial resolution at nadir of 13×24 km^2 and almost daily global coverage.

The XCO_2 anomalies are compared to the ODIAC (Open-source Data Inventory for Anthropogenic CO_2) emission estimates. ODIAC is a global high-resolution emission data set for fossil fuel CO_2 emissions [Oda and Maksyutov, 2011]. It was originally developed for the GOSAT project and is available at http://www.odiac.org/.

4.2.3 Methods

4.2.3.1 XCO_2 Anomalies

In order to detect the pollution areas, one first subtracts the daily median, calculated from the selected study region, from the individual observations. Hence, the XCO_2 anomalies are derived as

$$\mathbf{XCO_2(anomaly) = XCO_2(individual) - XCO_2(daily\ median).}$$

This step simultaneously deseasonalizes and detrends the data. The approach also reduces the effect of the changing spatial distribution of the data points and the impact of potential regional-scale biases in the OCO-2 data set. Based on the sensitivity analysis, the selection of the background region is not significant. The methodology is further illustrated in Figure 4.2-1.

In the second step, one calculates the mean from all the XCO_2 anomalies within a defined grid box (e.g., $1 \times 1°$ latitude-longitude) for a selected time period (e.g., one year).

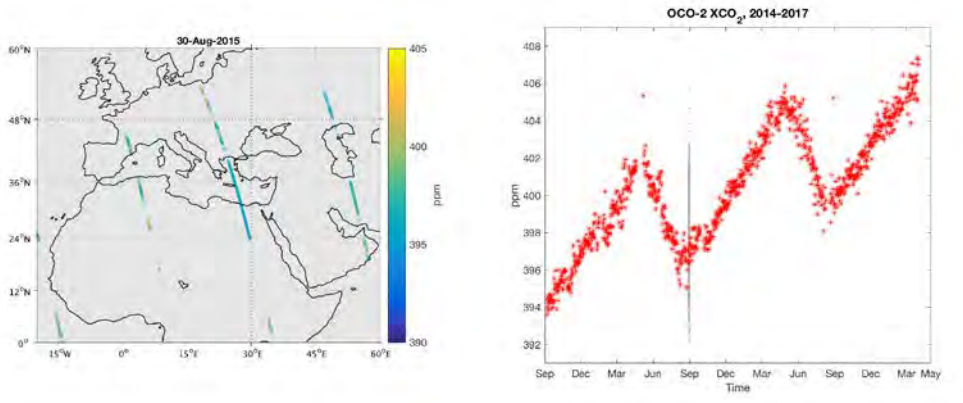

Figure 4.2-1. Map of OCO-2 XCO_2 observations during 30 August 2015 (left). Pixels are enlarged. OCO-2 daily median (red) values (right). Grey points indicate all the valid values observed during 30 August 2015. XCO_2 anomalies are obtained when the daily median is subtracted from these values. Figure adapted from [Hakkarainen et al., 2016].

4.2.3.2 Clustering methods

In order to combine the information from XCO_2 anomalies and NO_2 mean fields, and to discriminate different emission areas, the clustering methods [e.g., Aggarwal, 2015] are used. In particular, the study uses Expectation-Maximization (EM) clustering with mixture of Gaussian distributions. The results are also illustrated on maps in order to better understand the correlation between XCO_2 anomalies and NO_2 tropospheric columns.

4.2.4 Case Studies

4.2.4.1 Global XCO_2 Anomalies

The top row of Figure 4.2-2 displays the mean XCO_2 anomalies calculated for three different regions. One observes elevated values over the main polluted areas worldwide: eastern USA, central Europe, Middle East, China, India, and Japan. As expected from the emission inventories, the XCO_2 anomalies show the highest values over eastern China. Also, the areas in Africa where biomass burning occurs are characterized by elevated anomaly values.

The findings match the spatial distribution of the mean NO_2 tropospheric columns observed by OMI (middle row) and the ODIAC anthropogenic CO_2 emission inventory map (bottom row). The XCO_2 anomaly map shows, for example, the steep gradients in India, Japan, and north of Tibetan Plateau similar to those observed by OMI and emission inventories. Furthermore, it is possible to detect other enhancements over large cities on the U.S. West Coast and in Saudi Arabia.

As an example, Figure 4.2-3 shows a zoomed XCO_2 anomaly map over the Middle East with finer gridding (0.5 × 0.5°). In addition to the large polluted area in Iraq and Persian Gulf, several cities are detectable from the map, e.g., Cairo, Riyadh, and Tehran. In particular, we note that the XCO_2 anomaly values observed over Iraq are comparable to those in central Europe, suggesting

possible missing emission information in the inventories.

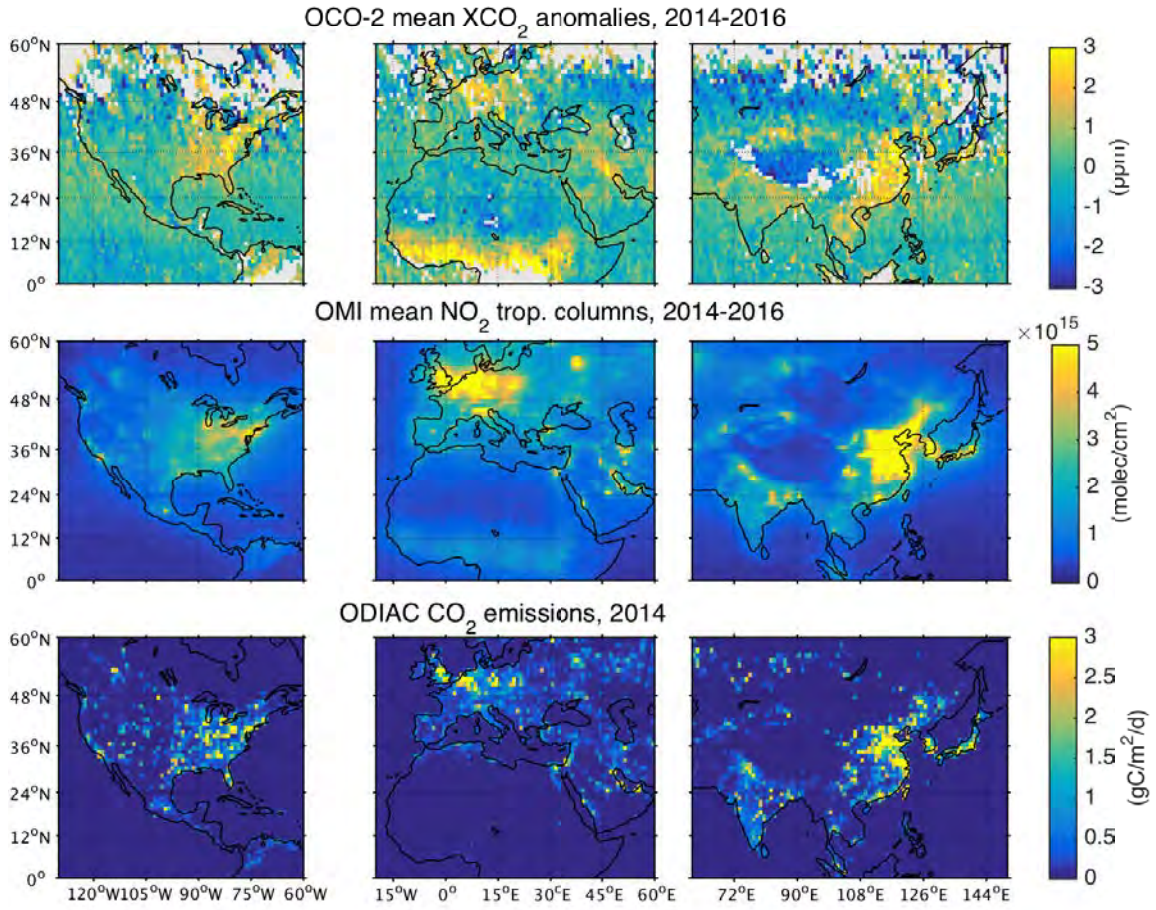

Figure 4.2-2. Mean OCO-2 XCO_2 anomalies (top row). Mean tropospheric OMI NO_2 columns (middle row). ODIAC emission inventory map (bottom row). The spatial resolution is 1 × 1°. Figure from [Hakkarainen et al., 2016].

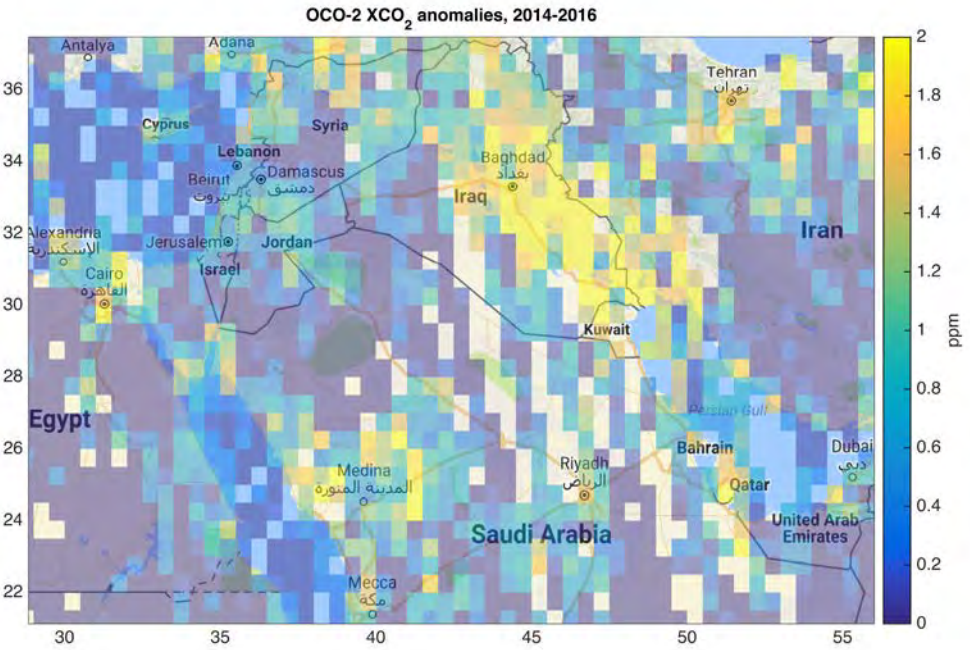

Figure 4.2-3. Mean OCO-2 XCO_2 anomalies over Middle East. Orange-yellow color tones highlight the most polluted areas. The spatial resolution is 0.5 × 0.5°. Figure from [Hakkarainen et al., 2016].

4.2.4.2 Cluster Analysis and Validation

The top row of Figure 4.2-4 shows the direct comparison between the NO_2 and XCO_2 anomaly data. In order to analyze the correlation between the two data sets cluster analysis is employed. In bottom row, the results of the cluster analysis are illustrated on a map. This allows the separation of different populations in the scatter plot (top row) and to identify their corresponding geographical location. As an example, in middle column, central Europe is selected together with Cairo, Istanbul, Moscow, and several Middle Eastern cities and oil extraction sites as the high-polluted cluster (yellow pixels). The rest of Europe and Middle East is selected as the next cluster (green). Another cluster (light blue) includes mainly the area in Africa affected by the emissions from biomass burning. Finally, the last cluster (dark blue) identifies the background.

The middle row of Figure 4.2-4 shows the direct comparison between XCO_2 anomalies and ODIAC CO_2 emissions, grouped according to the same clusters obtained from XCO_2 anomalies and NO_2 observations. The correlation between the mean XCO_2 anomalies and the emission inventories is further illustrated in Figure 4.2-5. The data are binned according to the emission values every 0.5 $gC/m^2/d$, after removing the data with low emissions (below 0.5 $gC/m^2/d$). A part of two outliers (related to number of data points) corresponding to Beijing and Moscow, one can observe a positive correlation between the anthropogenic CO_2 emissions and the XCO_2 anomalies.

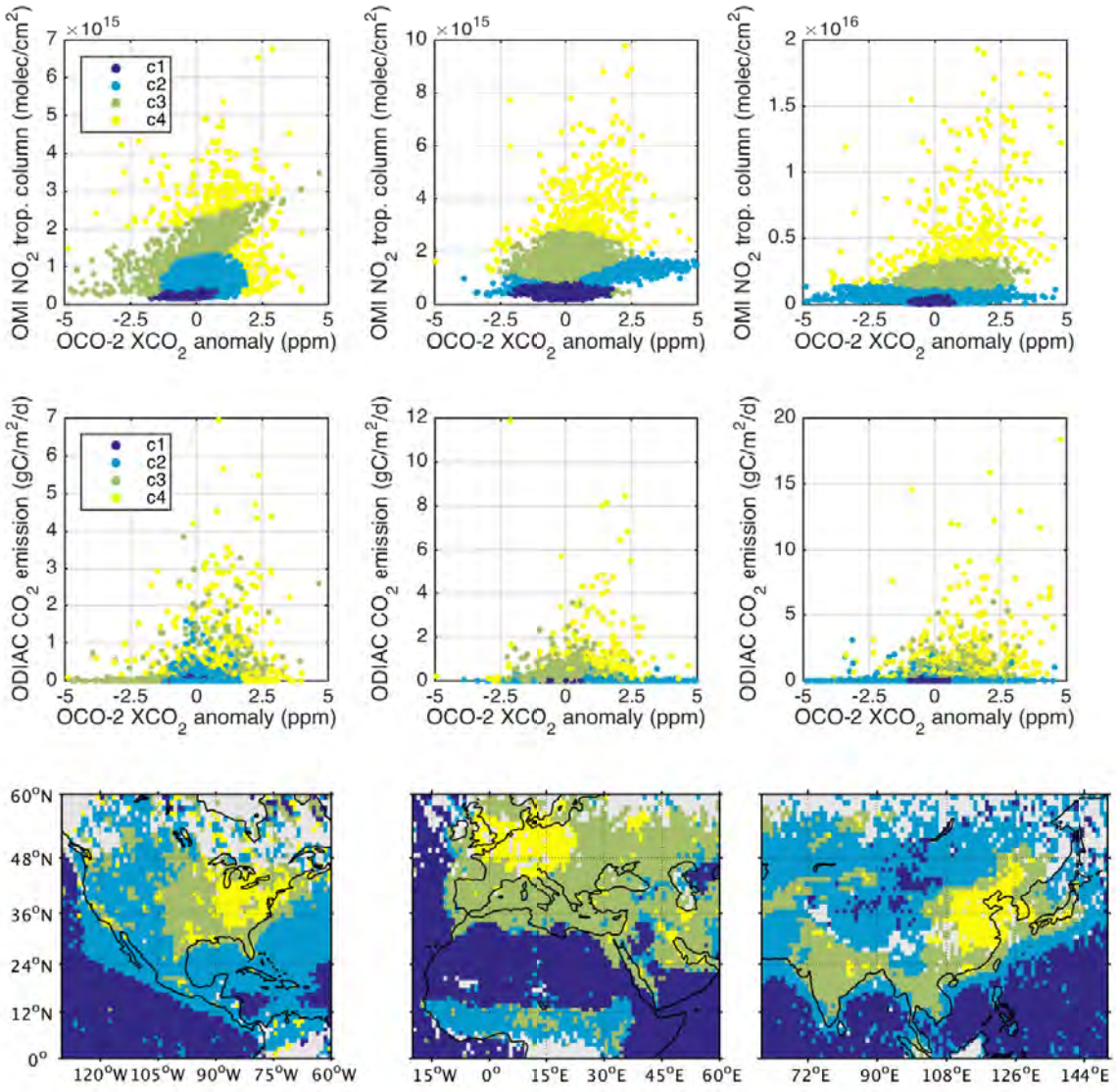

Figure 4.2-4. Scatterplot between mean OCO-2 XCO_2 anomalies and mean tropospheric OMI NO_2 columns (top row). The points are color-coded based on the results of the cluster analysis. Scatterplot between mean OCO-2 XCO_2 anomalies and ODIAC emission with same color-coding (middle row). Maps of the different clusters (bottom row). Figure from [Hakkarainen et al., 2016].

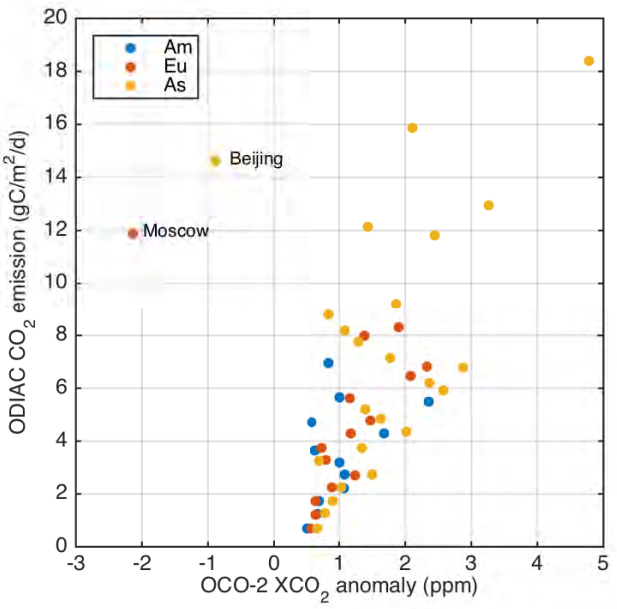

Figure 4.2-5. Scatterplot between mean OCO-2 XCO_2 anomalies and emission estimates for each region. The data are binned according to the emission values every 0.5 $gC/m^2/d$. Figure adapted from [Hakkarainen et al., 2016].

4.2.4.3 Future Outlook

The recent study [Hakkarainen et al., 2016] summarized here showed the first results on global XCO_2 anomalies using OCO-2 data. The study also combined the CO_2 and NO_2 information via cluster analysis. More work is needed to translate these anomalies into emissions using, e.g., statistical model as in many air quality studies. In addition to space-based NO_2 observations, more information can be obtained, e.g., from CO observations related to biomass burning. One can also use the same technique for other satellite instruments and species. As an example, Figure 4.2-6 shows the preliminary analysis of mean GOSAT XCO_2 and XCH_4 anomalies from the years 2009–2014. The long GOSAT data set provides a good opportunity to study trends in XCO_2 and XCH_4 anomalies.

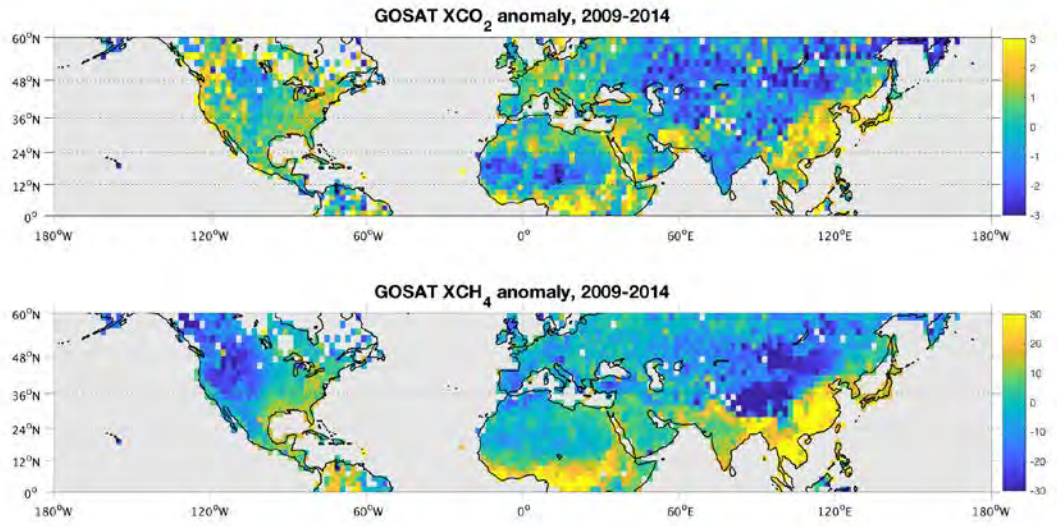

Figure 4.2-6. Mean GOSAT XCO_2 (top row) and XCH_4 (bottom row) anomalies for the years 2009–2014. The spatial resolution is 2 × 2°.

4.3 Using space-based observations to study urban CO_2 emissions and CH_4 emissions from fossil fuel harvesting

Eric A. Kort[1]

1) University of Michigan, Ann Arbor, Michigan, USA

4.3.1 Introduction

Since the pre-industrial era human activities have directly resulted in increased carbon dioxide (CO_2) and methane (CH_4) levels in the atmosphere, and this trend continues today. With better quantification of emissions of these gases, we can both better understand current and future climate trajectories as well as inform mitigation efforts. In some cases, human emissions are spatially localized. For CO_2, cities present large, concentrated sources, whereas for CH_4, regions of fossil-fuel harvesting often present intense, localized sources. These intensely emitting regions provide an opportunity for space-based observation and attribution that can be more challenging when sources are weaker and more distributed. In the following section, we illustrate the capability of space-based CO_2 and CH_4 measurement platforms to directly observe enhancements attributable to cities and fossil-fuel production, respectively [*Kort et al., 2012; 2014*]. These two cases illustrate that it is possible to observe and quantify elevated CO_2 and CH_4 levels from space, and that emission trends are also detectable. These cases also highlight challenges in expanding the use of these techniques, most notably the limitations of current data coverage from existing space-based sensors and the challenge of attributing signals to specific sources/source processes.

4.3.2 Data

Two different space-based platforms have been used in these case studies.

4.3.2.1 GOSAT

For the urban CO_2 example we analyzed column averaged dry air mole fraction of CO_2 (XCO_2) derived from measurements made by the Greenhouse gases Observing Satellite (GOSAT) [*Morino et al., 2011*]. GOSAT spectra were fit using the ACOS v2.9 level 2 algorithm [*Wunch et al., 2011; O'Dell et al., 2012; Crisp et al., 2012*]. Measurements for the urban study were collected between June 2009 and 2011. GOSAT footprints have approximated 10km diameter, and the urban analysis focused on measurements made in and around Los Angeles and Mumbai.

4.3.2.2 SCIAMACHY

For fossil-fuel harvesting CH_4 emissions we analyzed column averaged dry air mole fraction of CH_4 (XCH_4) retrieved from spectra collected by the SCanning Imaging Absorption SpectroMeter for Atmospheric CHartographY (SCIAMACHY) instrument from 2003-2009 [*Frankenberg et al., 2011*]. The United States was analyzed in detail, and in order to remove topographic effects on the

retrieval and to create methane anomaly figures we subtract a topographic dependent value [*Kort et al., 2014*].

4.3.3 Method

4.3.3.1 Urban CO_2 approach

To isolate CO_2 emissions from a concentrated urban source, we leverage GOSAT observations made directly over or downwind of the urban region, compared to observations in the vicinity of the city but not impacted by urban emissions. This complementary data is necessary to establish an enhancement attributable to urban emissions. By subtracting background values from the urban-influenced values, an enhancement attributable to emissions from a particular urban area can be isolated. One additional benefit of this difference method is the cancellation of bias errors shared between these two close observations (for example, a solar zenith angle dependence would be eliminated). In Figure 4.3-1, we show GOSAT data selected for Los Angeles [Kort et al., 2012]. In this case, the urban observations ("basin") were systematically elevated compared to the background value ("desert").

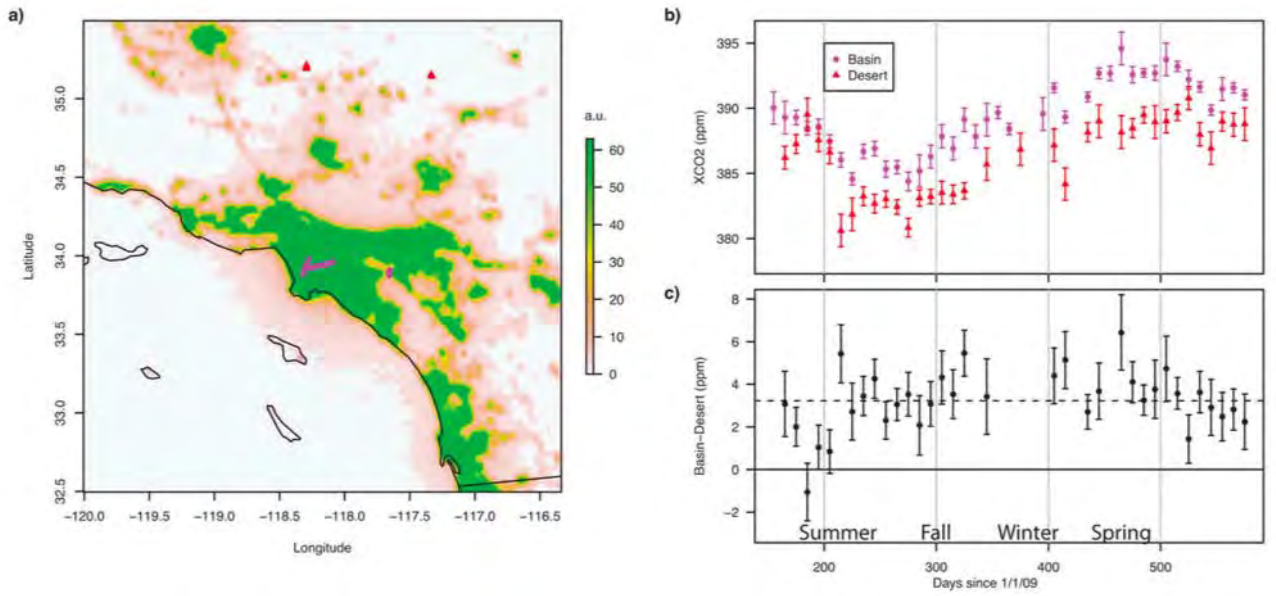

Figure 4.3-1. From Kort et al., 2012. a) Nightlights map of LA, with selected GOSAT observations within the basin (pink) and in the background desert (red triangles). b) Time-series for basin and desert observations averaged in 10-day bins. c) The different between basin and desert, showing an average enhancement of 3.2 ppm.

4.3.3.2 Fossil-fuel production region approach

To investigate methane emissions from the Four Corners region, we combined SCIAMACHY observations with an atmospheric transport model to directly link atmospheric concentrations to underlying fluxes. We used the Weather Research and Forecasting Chemical transport model

(WRF-Chem) [*Grell et al., 2005*] to represent atmospheric dynamics. By simulating atmospheric transport and advecting methane emissions from the EDGAR v4.2 inventory [*EDGAR 2011*], we produce simulated model enhancements that can be compared directly with the satellite observations. Figure 4.3-2 illustrates the observations, inventory, and simulation for the Four Corners regions [Kort et al., 2014].

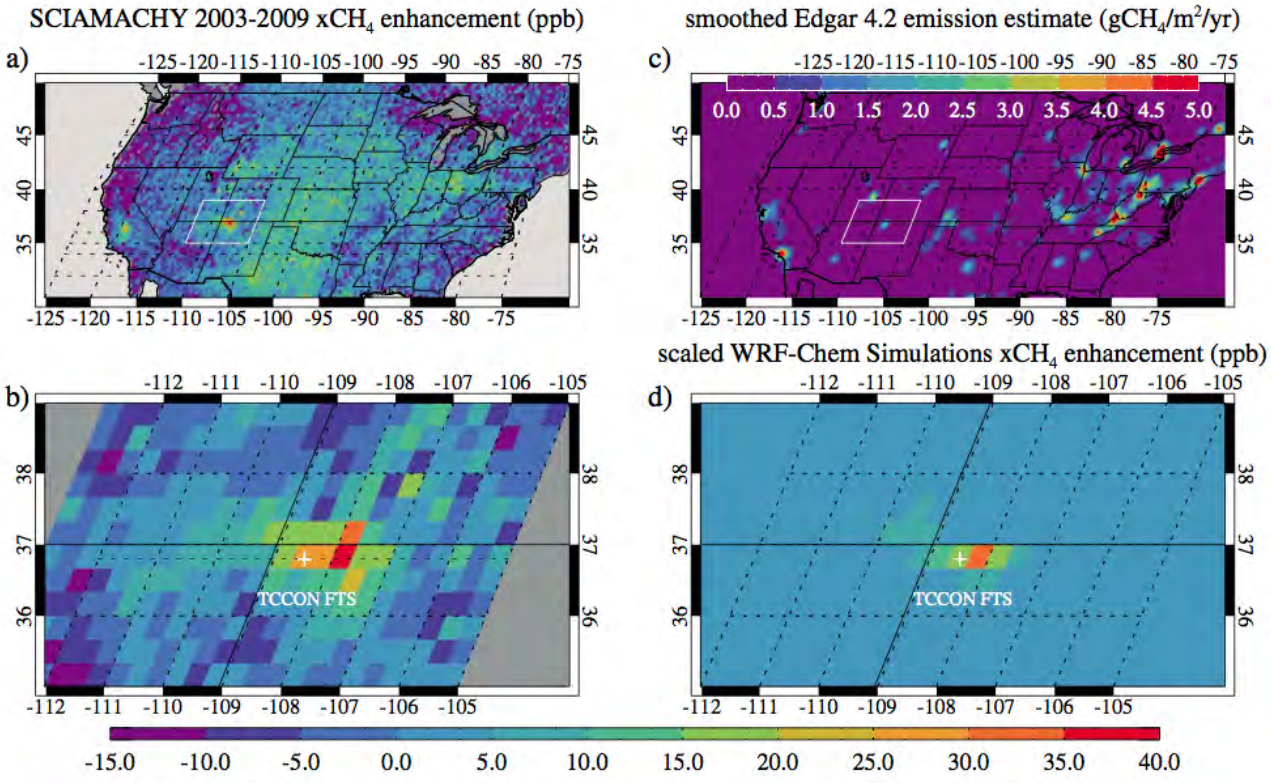

Figure 4.3-2. From Kort et al., 2014. **a)** Average SCIAMACHY anomaly from 2003-2009 gridded at 1/3 degree resolution. **b)** Average SCIAMACHY anomaly over just the Four Corners region from 2003-2009. **c)** EDGAR v4.2 gridded methane emissions (smoothed with a Gaussian filter). **d)** Gridded WRF-Chem simulated methane anomaly using 3.5 times EDGAR v4.2 emissions for the Four Corners region.

4.3.4 Case Studies

4.3.4.1 Urban CO_2: Los Angeles and Mumbai

Kort et al., 2012 found that robust urban enhancements were observable in both Los Angeles and Mumbai. In Mumbai, observations were limited to single soundings, which were still sufficient to detect elevated CO_2 levels over the urban domain. In Los Angeles, more plentiful observations were collected, which enabled authors to infer the average basin enhancement of 3.2 ppm in XCO_2 relative to the desert background. Consistency with ground-based observations confirms this to be a robust observation [*Kort et al., 2012*]. Assuming similar observations were made in a future year, a change in the column of 0.7 ppm would be detectable at the 95% level. This would correspond with

a 22% change in emissions if there is no change in the basin ventilation time or biospheric fluxes. This calculation assumes that the average GOSAT observations of elevated levels in the basin are representative of the entire basin, that sources are stationary in time and space, and meteorology isn't changing. A higher density of observations in space and time would greatly reduce the assumptions necessary, and targeted, high-resolution transport modeling would enable the determination of the relative impact of varying ventilation rates. Thus, this case study demonstrates the capability of space-based observations to observed urban CO_2 emissions, but that for quantification, attribution of sources, and tracking trends in emissions, improved spatial-temporal sampling would be invaluable. For tracking emission trends, it will also be important for long-term, sustained, consistent observations to establish sufficient time series for trend detection.

4.3.4.2 CH_4: Four Corners

In addition to identifying the Four Corners region as an anomalous location of high methane levels (Figure 4.3-2), a valuable demonstration of space-based capability, Kort et al., 2014 directly quantified the methane emissions from this domain. By fitting a linear model between observations and corresponding values simulated with WRF-Chem- EDGAR enables the derivation of a multiplicative factor to apply to the EDGAR inventory to best match the observations (Figure 4.3-3). For Four Corners, this results in an emissions estimate of 0.59 Tg CH_4/yr – a number far exceeding best inventory estimates at the time. Importantly, ground-based validation was applied in the Kort et al., 2014 study. This was further verified with a later, independent set of aircraft measurements, which found emissions consistent with the space-based estimate [*Smith et al., 2017*].

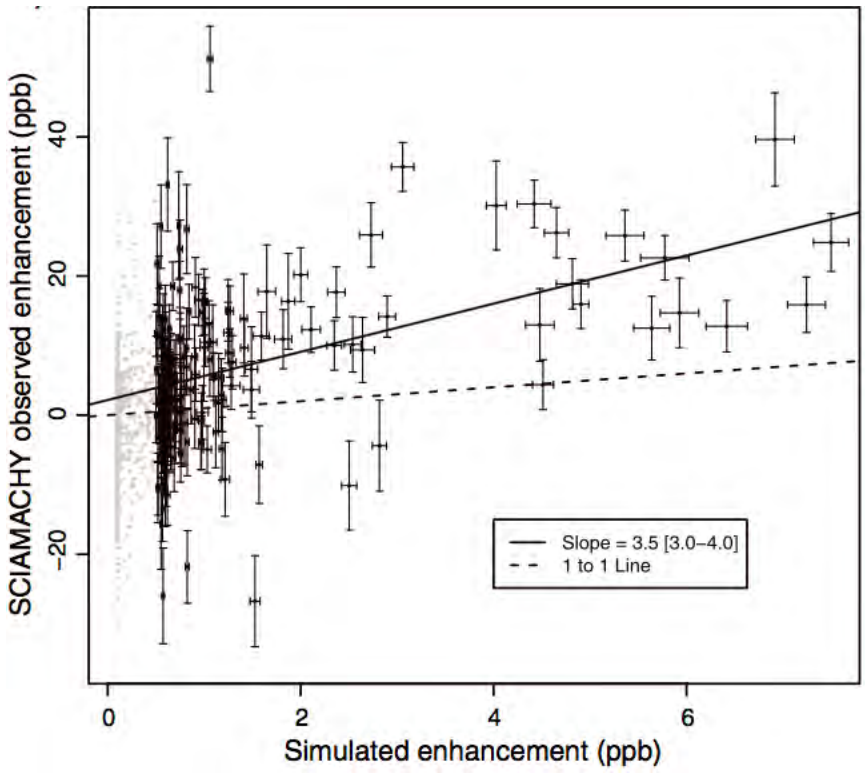

Figure 4.3-3. From Kort et al., 2014. Observed (SCIAMACHY 2003-2009 average) and simulated (WRF-Chem) methane over Four Corners, with slope (scaling factor) shown in solid line.

This case study illustrates that space-based methane observations can be used to identify regions with anomalously high emissions, and combining these measurements with a transport model can lead to direct quantification of emissions. Ground-based validation is essential to validate any space-based sensor and method for this type of regional estimation. Further, with any space-based approach measuring only methane, attribution to specific methane sources cannot be achieved unless the spatial resolution is greatly increased. Higher spatial resolution would allow individual plumes to be directly detected and attributed. In the absence of this resolution improvement overall flux estimates must focus on total emissions only, as opposed to trying to infer specific processes or leak rates.

4.4 Monitoring anthropogenic CO_2 and CH_4 emission by GOSAT observations

Rajesh Janardanan[1], Shamil Maksyutov[1], Tomohiro Oda[2,3], Makoto Saito[1], Akihiko Ito[1], Yukio Yoshida[1], and Tsuneo Matsunaga[1]

1) National Institute for Environmental Studies (NIES), Japan
2) Global Modeling and Assimilation Office, NASA Goddard Space Flight Center, Greenbelt, Maryland, USA
3) Goddard Earth Science Technologies and Research, Universities Space Research Association, Columbia, Maryland, USA

4.4.1 Introduction

The Greenhouse gases Observing SATellite (GOSAT), developed jointly by the Ministry of the Environment (MOE), the National Institute for Environmental Studies (NIES), and the Japan Aerospace Exploration Agency (JAXA) is the world's first satellite designed specifically to monitor greenhouse gases from space. The satellite has continued to fulfill its main mission to monitor atmospheric carbon dioxide (CO_2) and methane (CH_4) concentrations from space since its launch in January 2009.

Here an overview of a study by Janardanan et al., 2016, and Janardanan et al., 2017, demonstrating the capability of GOSAT to observe anthropogenic emission signature as abundance in XCO_2 and XCH_4 respectively from surrounding cleaner background values and compare it with emission inventory-based high-resolution simulation for regional emission monitoring technique, is given.

4.4.2 Data

4.4.2.1 GHG Concentration Data

Janardanan et al., 2016 utilized the National Institute for Environmental Studies GOSAT Short Wavelength InfraRed XCO_2 Level 2 product (NIES SWIR L2 v02.21) during the period of June 2009 to December 2012.

Janardanan et al., 2017 utilized the National Institute for Environmental Studies GOSAT Short Wavelength InfraRed XCH_4 Level 2 product (NIES SWIR L2 v02.21) during June 2009 to December 2012.

The data processing and related information can be found in GOSAT Data Archive Service (GDAS) website, https://data2.gosat.nies.go.jp/.

4.4.2.2 CO_2 emission inventory

Janardanan et al., 2016 used the Open-source Data Inventory for Anthropogenic Carbon dioxide (ODIAC) (Oda and Maksyutov, 2011) as fossil fuel CO_2 emission for the period 2009-2012

at 0.1 degree resolution. To correct GOSAT XCO_2 observations for the contribution of CO_2 emission from biomass burning in the GOSAT XCO_2 ($\Delta XCO_{2,fire}$), they performed Lagrangian retroplume simulation with fire emissions prescribed by the Global Fire Assimilation System (GFAS version 1.1, (Kaiser et al., 2012)). The influence of terrestrial biospheric CO_2 fluxes on XCO_2 ($\Delta XCO_{2,bio}$) is estimated in a similar way using the Vegetation Integrative Simulator of Trace gases (VISIT) (Ito, 2010; Saito et al., 2014). The meteorological reanalysis data used for transport modeling were taken from the Japanese 25 year reanalysis (JRA-25)/Japan Meteorological Agency (JMA) Climate Data Assimilation System (JCDAS, Onogi et al. (2007)).

4.4.2.3 CH_4 emission inventory

Janardanan et al., 2017 used, used the anthropogenic methane emission inventory (Emission Database for Global Atmospheric Research–EDGAR v4.2 FT2010 (Olivier and Janssens-Maehnhout, 2012)), for the period 2009-2010 at 0.1 degree resolution for the high-resolution transport modeling. For the years 2011 and 2012 the data are scaled using the global total value of those years as reported by EDGAR. In order to account for the contribution from wetland emission and soil sink of methane, model simulated values were adjusted in the observations. For this, they used fluxes from Vegetation Integrative SImulator for Trace gases model (VISIT; Ito and Inatomi, 2012).

4.4.3 Method

4.4.3.1 Outline

Janardanan et al., 2016 used a Lagrangian particle dispersion model, FLEXPART (Stohl et al., 1998, 2005) to simulate XCO_2 abundance ($\Delta XCO_{2,sim}$) caused by local emissions from fossil fuel combustion at all satellite observation locations. Based on these model estimates, they select satellite observations influenced substantially by fossil fuel emissions ($\Delta XCO_{2,sim} > 0.1$ ppm). Observed enhancements ($\Delta XCO_{2,obs}$) were computed as deviations from the background defined as a monthly mean of all “clean” (observations that are not influenced by emission from fossil fuel) measurements in the area around the observation point (average of observations with low contribution from fossil fuel sources in $10° \times 10°$ boxes). These simulated and observed XCO_2 abundance was binned for each 0.2 ppm to reduce the stochastic errors of the order of 2 ppm (Yoshida et al., 2013) associated with each individual satellite observation, and subjected to weighted linear regression analysis. The regression slope gives a scale factor which indicates the agreement between observations and inventory based XCO_2 abundance and thus any biases in the inventory. The method is illustrated in Figure 4.4-1. Similarly in Janardanan et al., 2017, XCH_4 abundance were estimated from GOSAT XCH_4 data and the inventory based estimates.

4.4.4 Case Study results

4.4.4.1 Results from Janardanan et al., 2016

The objective of this study was to develop a technique to find XCO_2 abundance from GOSAT observations and to relate it with XCO_2 abundance simulated using a high resolution emission inventory (as shown in Figure 4.4-2). They demonstrated that over sufficiently large regions, the XCO_2 abundance estimated from GOSAT observations can be represented as a function of inventory based simulated XCO_2 abundance and the regression coefficient (slope value) is indicative of potential biases in the emission inventory. In this study, for the global case, observed and simulated enhancements showed good agreement with a slope of 1.21 ± 0.21 ($p < 0.05$); Figure 4.4-3. The error in the slope accounts for combined effect of noisy observational data, errors in background estimate, and dispersion model, and deviation of enhancements from regression line. In the Northern Hemisphere, the slope value is 1.12 ± 0.22 ($p < 0.05$), and for Eurasia they got value of 1.24 ± 0.27 ($p < 0.05$). In the case of these three large domains, though the slope differ from unity (within the uncertainty range), the observed and simulated enhancements are very close to the "identity line" suggesting that the emissions from strong point sources are well captured in the model. However, when this analysis is carried out for East Asia, the S_r value is similar (1.22 ± 0.32, ($p < 0.05$); Figure 4.4-3d), but the regression line has a large offset from the identity line (identity line outside observation uncertainty range)—indicating significant difference between the mean simulated ($\Delta XCO_{2,sim}$) and observed XCO_2 abundance ($\Delta XCO_{2,obs}$). For North America, they found an S_r value of 1.05 ± 0.38 ($p < 0.1$), showing good match between model and observations though the uncertainty is largest among the five regions due to the smaller number of observations (Figure 4.4-3e).

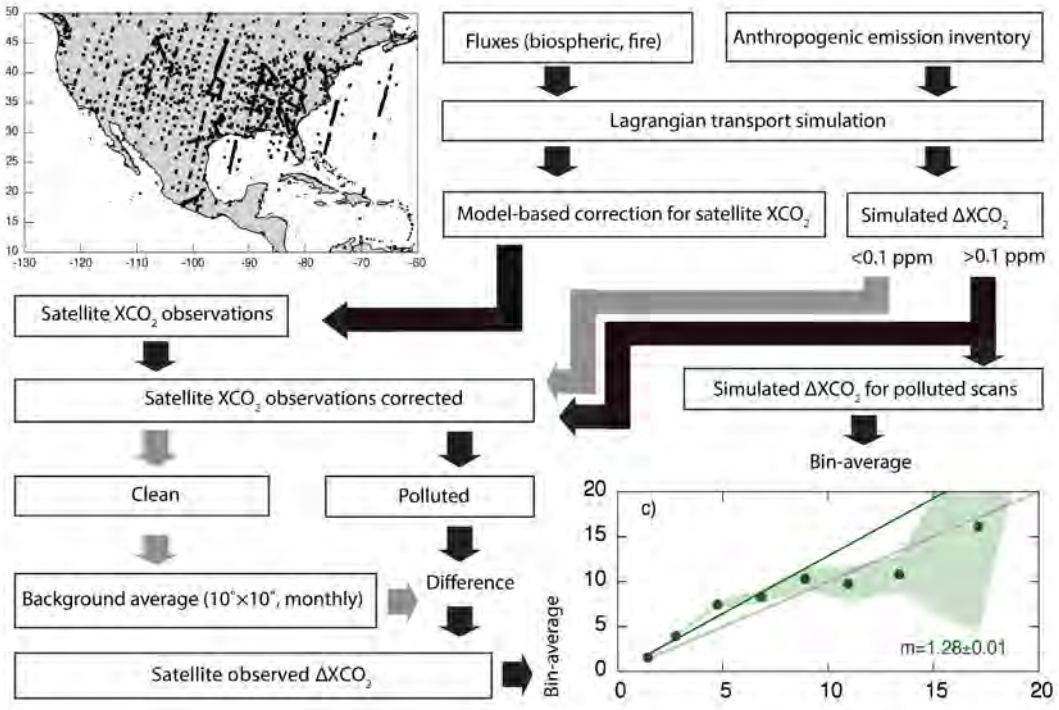

Figure 4.4-1. Schematic showing the procedure of data processing explained in section 4.4.3

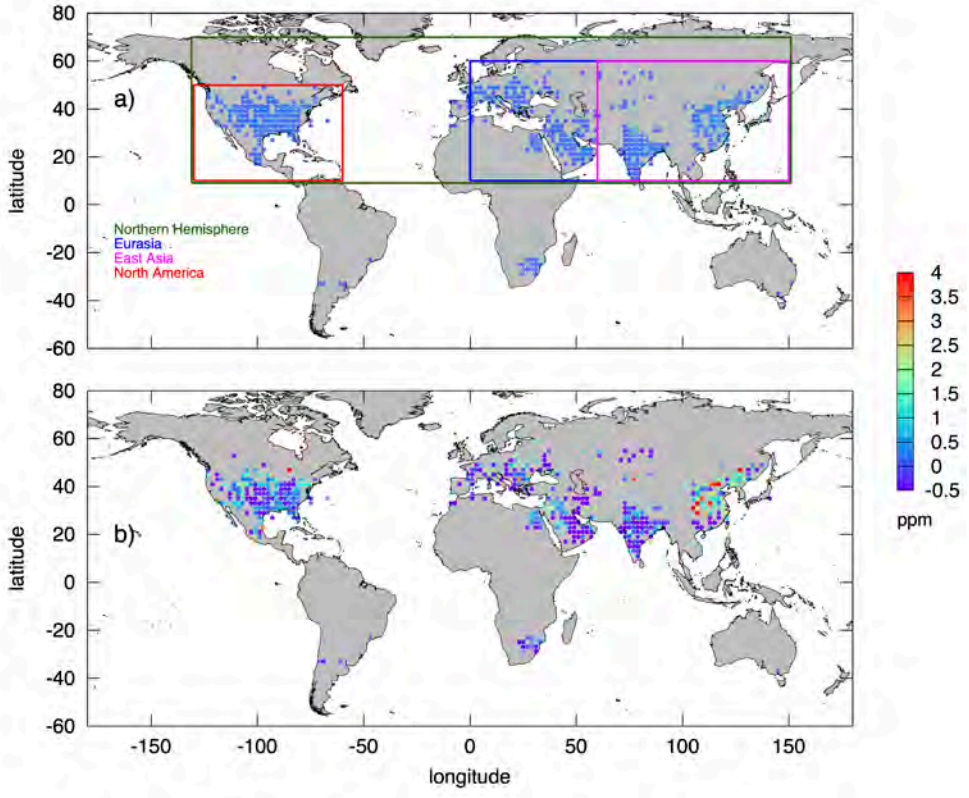

Figure 4.4-2. a) Simulated fossil fuel enhancements in XCO_2 and b) GOSAT observed XCO_2 anomalies averaged over 2° × 2° grid over anthropogenic sources regions over the globe for 2009–2012. The macro regions—East Asia (10–60°N, 60–150°E), Eurasia (10–60°N, 0–150°E), North America (10–50°N, 130–60°W), and the Northern Hemisphere (10–70°N, 130°W–150°E) are shown by colored rectangles. Adapted from Janardanan et. al., 2016.

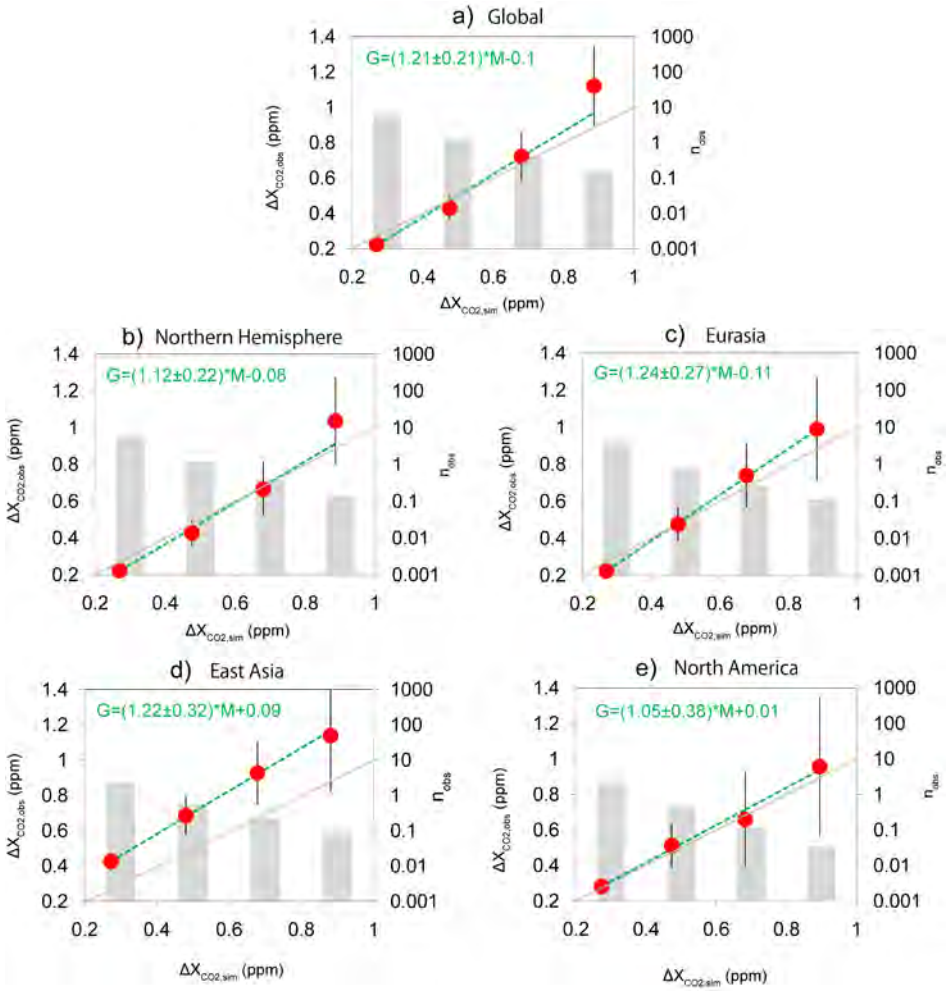

Figure 4.4-3. The regression between observed and simulated XCO_2 abundance averaged over major anthropogenic source regions. Vertical thin lines show the standard error of the mean observed enhancements. The grey dashed line is the identity line and the error-weighted regression is shown as the green dashed line. The grey bars give the number of observations in thousands. Adapted from Janardanan et al., 2016

The difference between the inventory and observations over East Asia suggested by regression analysis imply that ODIAC inventory emissions are lower than needed to match the observations. This region is known for significant differences between various fossil fuel CO_2 emission inventories (eg. Guan et al., 2012; Liu et al., 2015). For example, a recent study (Guan et al., 2012) estimated Chinese provincial total CO_2 emissions of 9.08 Gt yr^{-1} for 2010, which is 1.4 Gt yr^{-1} more than the China's national statistical report. Liu et al. (2015) reported that the Chinese energy consumption was 10% higher than the Chinese national statistics. Another study (Zhao et al., 2012) recompiling the Chinese CO_2 emissions using provincial level energy statistics revealed that CO_2 emission from fossil fuel and cement production showed notable differences with accepted estimates (e.g., 5–10% higher than CDIAC (Boden et al., 2013) during 2005–2009). The discrepancy between simulated and observed XCO_2 abundance (22%) and its uncertainty (32%) over East Asia are comparable to the uncertainties (~15%) associated with fossil fuel CO_2 emission over this region.

4.4.4.2 Results from Janardanan et al., 2017

Janardanan et al., 2017, conducted the study to utilize GOSAT satellite observations to independently monitor methane emissions from anthropogenic sources. The regression is carried out to a maximum XCH_4 abundance of 20 ppb only for a 2 ppb bin averaged values, considering the decreasing number of observations in each bin and the growing error in binned values. The large continental regions having significant emission from anthropogenic sources are north America, East Asia, Europe and the Middle East. In this analysis they selected North America and East Asia based on their contribution to global emissions and availability of large number of useful satellite observations. For the global case, the model-observation regression gives a regression coefficient (slope) of 1.15±0.03 (Figure 4.4-5; R^2 =0.97). For East Asia, the regression slope is 0.70±0.05 (R^2 =0.96) and for North America it is 1.28±0.01 (R^2=0.65). North American regions show the largest difference between the GOSAT observed and EDGAR based XCH_4 anomaly, compared to other regions. The regression slope shows around 28% deviation from unity. This shows a mismatch between observations based and inventory based XCH_4 anomalies over northern America and thereby a potential underestimation in the emission inventory. Over the East Asian region, the model-observation mismatch is approximately 30%, emission being higher than suggested by observation derived enhancements.

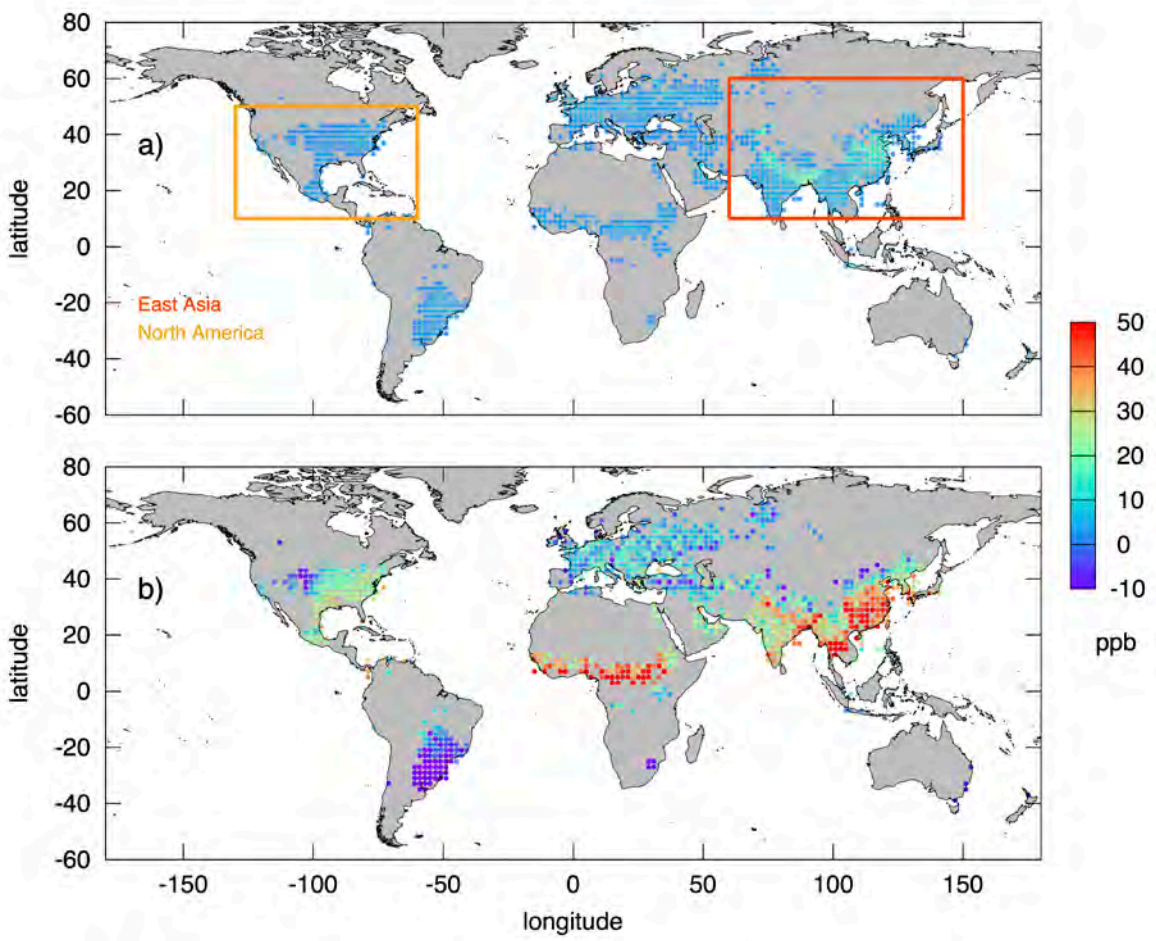

Figure 4.4-4. The simulated (a) and GOSAT observed (b) XCH_4 anomaly (ppb) ($\Delta XCH_{4,sim}$ and $\Delta XCH_{4,obs}$ respectively) aggregated at 2° grid for a period 2009-2012. The grids with simulated XCH_4 abundance greater than 5 ppb in average are shown. The regions used in analysis are marked as rectangles in upper panel. Adapted from Janardanan et al., 2017

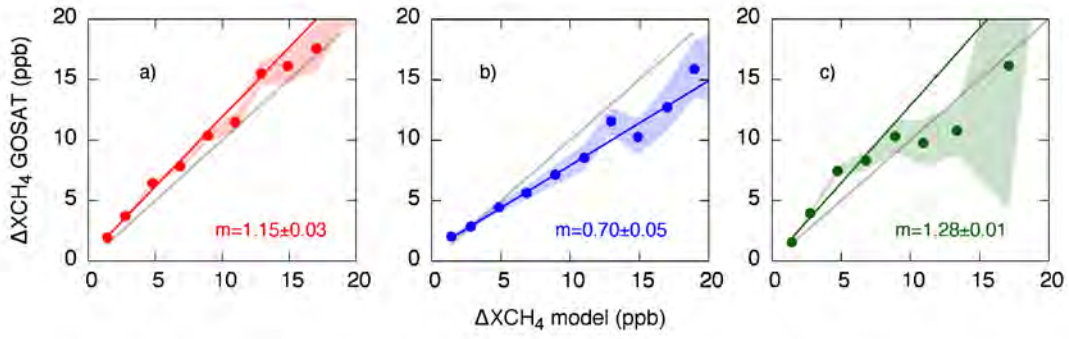

Figure 4.4-5. The regression between modeled (EDGAR) and observed (GOSAT) XCH_4 abundance for a) the Globe, b) East Asia and c) North America. The inset values (m) are the regression coefficient (unit less) with the associated estimation error. The light shading represents the standard error in each bin. The colored lines show the regression model and the grey lines show the identity line. Adapted from Janardanan et al., 2017

4.5 Anthropogenic methane emissions from SCIAMACHY and GOSAT

M. Buchwitz[1], O. Schneising-Weigel[1], M. Reuter[1], H. Bovensmann[1], and J. P. Burrows[1]
1) Institute of Environmental Physics (IUP), University of Bremen, Germany

4.5.1 Introduction

SCanning Imaging Absorption spectroMeter for Atmospheric CHartographY (SCIAMACHY) (Burrows et al., 1995; Bovensmann et al., 1999) onboard of the European environmental satellite ENVISAT was operational from March 2002 to April 2012. SCIAMACHY was a passive remote sensing spectrometer observing backscattered, reflected, transmitted or emitted radiation from the atmosphere and Earth's surface, in the wavelength range between 240 and 2380 nm. The spatial resolution depends on spectral region but was typically 30 km along track and 60 km across track. Global coverage at the equator was achieved after six days (swath width 960 km; nominal measurement sequence: 50% nadir (downlooking) and 50% limb (scanning the atmosphere while looking to the horizon and above)). For the retrieval of column-averaged dry-air mole fractions of methane (CH_4), i.e., XCH_4, two spectral regions have been used: the 1.6 μm region containing CH_4 (and CO_2) absorption lines and the 0.76 μm spectral region covering the oxygen (O_2) A-band. Details on the retrieved XCH_4 are given in a number of peer-reviewed publications (e.g., Buchwitz et al., 2000, 2015, 2016; Schneising et al., 2009, 2011).

In addition, an ensemble of GOSAT (Kuze et al., 2009) XCH_4 retrievals (see Buchwitz et al., 2016, and references given therein) have been used.

In the following results from two studies related to anthropogenic CH_4 emissions, which have been published in the peer-reviewed scientific literature (Schneising et al., 2014a; Buchwitz et al., 2017), are summarized.

4.5.2 Data

4.5.2.1 GHG Concentration Data

Schneising et al., 2014a, used SCIAMACHY XCH_4 retrievals during the time period 2006-2011.

Buchwitz et al., 2017, used an ensemble of SCIAMACHY and GOSAT XCH_4 retrievals (described in Buchwitz et al., 2016), which has been generated within the framework of the GHG-CCI project (http://www.esa-ghg-cci.org/) of ESA's Climate Change Initiative (Hollmann et al., 2013). Buchwitz et al., 2017, also used CAMS (Copernicus Atmosphere Monitoring Service; http://atmosphere.copernicus.eu/) a posteriori methane emissions and corresponding atmospheric methane version v10-S1NOAA as generated via the TM5-4DVAR assimilation system assimilating National Oceanic and Atmospheric Administration (NOAA) CH_4 surface observations (an earlier version of this method and resulting data products is described in Bergamaschi et al., 2009). In

addition, a high-resolution methane model data set over the USA has been used (Turner et al., 2015).

4.5.2.2 Other Data

Schneising et al., 2014a, used meteorological information (primarily near surface winds) as provided by the ERA-Interim reanalysis product (Dee et al., 2011) of the European Centre for Medium-RangeWeather Forecasts (ECMWF). Furthermore, Schneising et al., 2014a, used well positions taken from the Fracking Chemical Database (SkyTruth, 2013) complemented by data for the Canadian part of the Bakken basin (U.S. Energy Information Administration, 2012).

Buchwitz et al., 2014, used EDGAR version 4.2 anthropogenic methane emissions (obtained from http://edgar.jrc.ec.europa.eu/gallery.php?release=v42&substance=CH4&sector=TOTALS).

4.5.3 Methods

4.5.3.1 Outline

Different methods have been used in each of the two publications. These methods are shortly described in the following sub-sections.

4.5.3.2 Methodology used by Schneising et al., 2014a

Schneising et al., 2014a, used a simple mass-balance approach to obtain estimates of methane emission differences between two three-year time periods (2006-2008 and 2009-2011) from SCIAMACHY XCH_4 retrievals for three major North American oil and gas production regions.

For details please see Schneising et al., 2014a.

4.5.3.3 Methodology used by Buchwitz et al, 2017

Buchwitz et al., 2017, also used a simple data-driven mass-balance approach to obtain estimates of annual methane emissions during 2003-2014 from annually averaged maps generated from an ensemble of SCIAMACHY and GOSAT XCH_4 retrievals. The method has been applied to four methane “hot spot” regions, i.e., regions showing regionally elevated XCH_4 in satellite-derived XCH_4 maps. The emission results have been compared with EDGAR and information available in the peer-reviewed literature. For details please see Buchwitz et al., 2017.

4.5.4 Case Study Results

In the following two sub-sections the results from these two case studies are shortly presented and summarized.

4.5.4.1 Results obtained by Schneising et al., 2014a

The main results obtained by Schneising et al., 2014a, are shown in Fig. 4.5-1. Shown on the left hand side is the absolute methane emission increase for 2009–2011 relative to 2006–2008 along with the 1-sigma uncertainty range for the two "fracking areas" Bakken and Eagle Ford in the USA as obtained from the SCIAMACHY XCH_4 retrievals. On the right relative methane leakage rates are shown for Bakken and Eagle Ford in comparison to published values from other gas and/or oil production regions in the USA and EPA estimates for natural gas and petroleum. Schneising et al., 2014a, conclude that current inventories likely underestimate fugitive methane emissions.

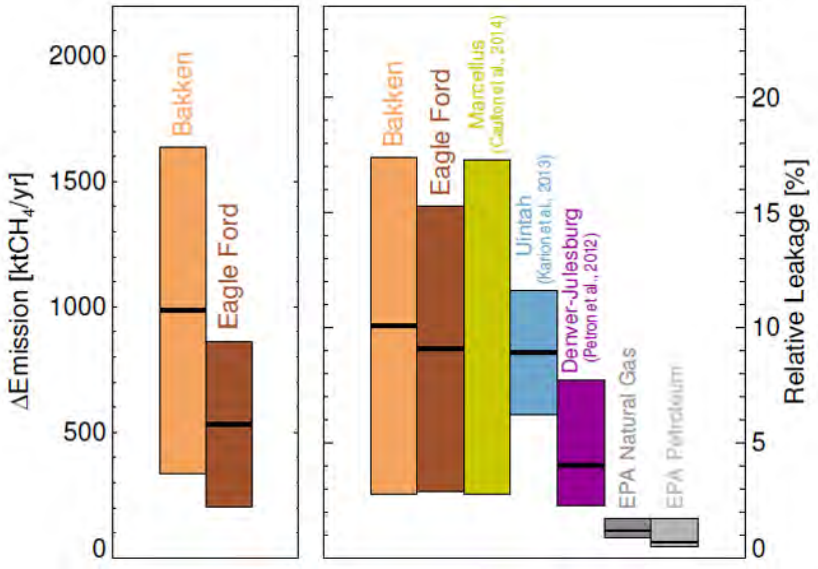

Figure 4.5-1. Estimated methane emissions are shown for the targeted regions Bakken in light brown, and Eagle Ford in dark brown. Shown is the absolute emission increase (2009–2011 relative to 2006–2008) in the left panel, and the leakage rate relative to production in the right panel, in each case together with the 1σ-uncertainty ranges. For comparison, leakage estimates from previous studies in Marcellus (2012) (Caulton et al., 2014), Uintah (2012) (Karion et al., 2013), and Denver-Julesburg (2008) (Pétron et al., 2012) (yellow, blue, and magenta) are shown together with the EPA bottom-up inventory estimates for natural gas and petroleum systems (2011) (U.S. Environmental Protection Agency, 2014) (grey) in the right panel. (from: Schneising et al., 2014a; their Fig. 7).

4.5.4.2 Results obtained by Buchwitz et al., 2017

Buchwitz et al., 2017, obtained annual methane emissions during 2003-2014 from an ensemble of SCIAMACHY and GOSAT XCH_4 retrievals. Their main results are shown in Fig. 4.5-2 and summarized in Tab. 4.5-1. They applied their method to four source areas: Four Corners in the south-western USA, the southern part of the Central Valley in California, Azerbaijan, and Turkmenistan. They found that their estimated emissions are in good agreement with independently derived estimates for Four Corners and Azerbaijan. For the Central Valley and Turkmenistan their estimated annual emissions are higher compared to the EDGAR v4.2 anthropogenic emission inventory. For Turkmenistan they found on average about 50% higher emissions with their annual emission uncertainty estimates overlapping with the EDGAR emissions. For the region around Bakersfield located in the Central Valley of California, a region of significant oil and gas production and large expected methane emissions from dairy and livestock operations, Buchwitz et al., 2017, obtained mean emissions in the range 1.05–1.55 MtCH4/yr, depending on satellite data product. This is about a factor of 5–8 higher than the total methane emissions as given in the EDGAR v4.2 inventory but of similar magnitude as reported in Jeong et al. (2013) (0.85–0.94 MtCH4/yr) based on inverse modelling of tower measurements. The Buchwitz et al., 2017, findings also corroborate published results from CalNex campaign aircraft observations during May to June 2010 (Wecht et al., 2014b) showing high methane concentrations over the southern part of the Central Valley, in the San Joaquin Valley, compared to other parts of California and concluding that EDGAR emissions in this area need to be scaled with factors up to around 5. They conclude that livestock emissions in EDGAR are significantly underestimated. Another more recent study (Jeong et al., 2014) presented a new bottom-up methane inventory for the year 2010 for California, concluding that their emissions are 3–7 times higher compared to official California bottom-up inventories for the petroleum and natural gas production sectors. Also the new US Environmental Protection Agency (EPA) methane emission inventory (Maasakkers et al., 2016) shows significantly larger emission in the area around Bakersfield compared to EDGAR v4.2. Nevertheless, the Buchwitz et al., 2017, results need to be interpreted with care as the uncertainty of their annual emission estimates is large and it cannot be entirely ruled out that their estimates are somewhat overestimated e.g. due to possible methane accumulation in the valley.

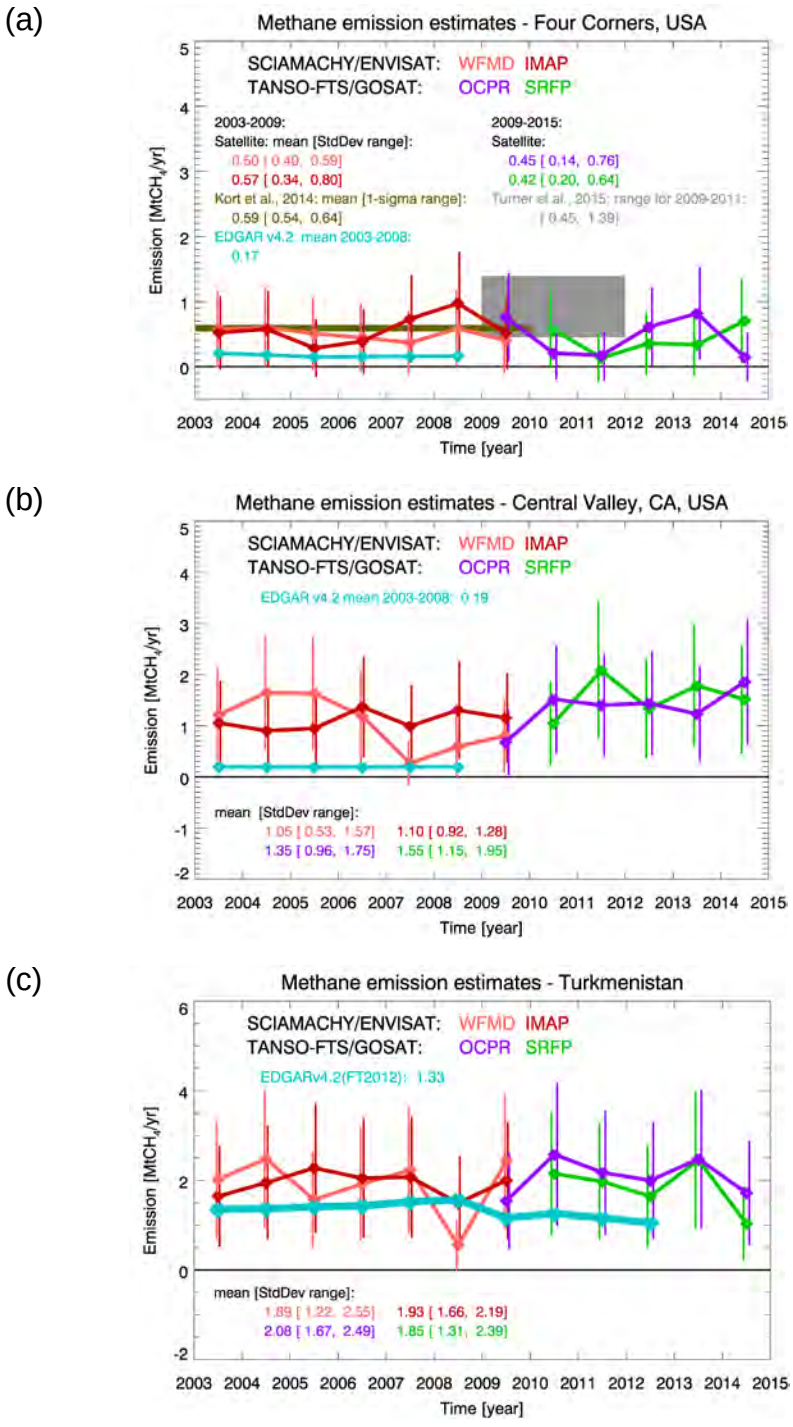

Figure 4.5-2: Annual methane emissions as obtained from SCIAMACHY and GOSAT for the three regions: (a) Four Corners in the USA, (b) Central Valley, California, USA, and (c) Turkmenistan compared with EDGAR and literature values. The results are summarized in Tab. 4.5-1, where additional details are given. Source: Buchwitz et al., 2017.

Table 4.5-1. Summary of the main results of the study of Buchwitz et al., 2017, listing the estimated methane emissions for four methane "hot spot" areas in terms of annual mean value and 1-sigma range obtained from computing the standard deviation of the annual emissions. The satellite-derived annual methane emissions are covering the time period 2003-2009 for SCIAMACHY and 2009-2014 for GOSAT. The results have been obtained using two data sets from SCIAMACHY (obtained with the WFMD and IMAP retrieval algorithms) and two from GOSAT (obtained with the algorithms OCPR and SRFP (also known as RemoTeC)); for details (and references) on the algorithms and corresponding data products see Buchwitz et al., 2016. Source: Buchwitz et al., 2017.

	Estimated methane emissions [$MtCH_4$/year]				
	SCIAMACHY		**GOSAT**		**Comments /**
Source region	**WFMD**	**IMAP**	**OCPR**	**SRFP (RemoTeC)**	**Other estimates**
Four Corners	0.50 [0.40, 0.59]	0.57 [0.34, 0.80]	0.45 [0.14, 0.76]	0.42 [0.20, 0.64]	Kort et al., 2014 (*): 0.59 [0.54, 0.64] Turner et al., 2015: [0.45, 1.39] EDGAR v4.2: 0.17
Central Valley (southern part)	1.05 [0.53, 1.57]	1.10 [0.92, 1.28]	1.35 [0.96, 1.75]	1.55 [1.15, 1.95]	EDGAR v4.2: 0.19 Jeong et al., 2013: 0.85 – 0.94 (for their region R12)
Azerbaijan	0.60 [-0.01, 1.21]	0.53 [0.23, 0.83]	0.51 [-0.16, 1.18]	-	EDGAR v4.2 (FT2012): 0.74
Turkmenistan	1.89 [1.22, 2.55]	1.93 [1.66, 2.19]	2.08 [1.67, 2.49]	1.85 [1.31, 2.39]	EDGAR v4.2 (FT2012): 1.33

(*) Kort et al., 2014, report the 2-sigma range [0.50, 0.67], not the (approximate) 1-sigma range listed here.

4.6 A case study estimating global and regional methane emissions using GOSAT

Alexander J. Turner[1]

1) Department of Earth and Planetary Sciences, University of California, Berkeley, CA, USA.

4.6.1 Introduction

Methane is a greenhouse gas emitted by a range of natural and anthropogenic sources (Kirschke et al., 2013; Saunois et al., 2016). A difficulty in quantifying anthropogenic emissions is that they tend to originate from a large number of relatively small and often transient point sources such as livestock operations, oil/gas leaks, landfills, and coal mine ventilation. Atmospheric methane observations from surface and aircraft have been used to detect and quantify emissions (e.g., Houweling et al., 2016; Miller et al., 2013; Caulton et al., 2014; Karion et al., 2013, 2015; Lavoie et al., 2015; Conley et al., 2016; Peischl et al., 2012, 2015, 2016) but are limited in spatial and temporal coverage. Satellite measurements are attractive for the dense and continuous coverage they provide.

Satellite-based observations by solar backscatter in the shortwave infrared (SWIR) from low-Earth orbit have been available since 2003 from the SCIAMACHY instrument (2003–2012; Frankenberg et al., 2005) and from the GOSAT instrument (2009–present; Kuze et al., 2009, 2016). SWIR instruments measure the atmospheric column of methane with near-unit sensitivity down to the surface. SCIAMACHY and GOSAT demonstrated the capability for high-precision (<1%) measurements of methane from space (Buchwitz et al., 2015). GOSAT has higher precision and pixel resolution than SCIAMACHY (0.6% and 10 km×10 km vs. 1.5% and 30 km×60 km), but the observations are not as dense. The GOSAT retrievals are in good agreement with surface-based column measurements (Parker et al., 2011; Butz et al., 2011; Schepers et al., 2012; Fraser et al., 2013; Monteil et al., 2013; Cressot et al., 2014; Alexe et al., 2015). Here we discuss results using GOSAT to estimate global and regional methane emissions sources as well as the mathematical framework for estimating methane sources using satellite observations. Results presented here were originally published in Turner et al. (2015) and Turner and Jacob (2015).

4.6.2 Inversion methodology

4.6.2.1 Background

Inverse models quantify the state variables driving the evolution of a physical system by using observations of that system. This requires a physical model $\mathbf{F}$, known as the forward model, that relates a set of input variables $\mathbf{x}$ (state vector) to a set of output variables $\mathbf{y}$ (observation vector),

$$\mathbf{y} = \mathbf{F}(\mathbf{x}) + \boldsymbol{\varepsilon}. \quad (1)$$

The observational error $\boldsymbol{\varepsilon}$ includes contributions from both the forward model and the measurements. Solution to the inverse problem involves statistical optimization to achieve a best error-weighted estimate of $\mathbf{x}$ given $\mathbf{y}$.

A critical step in solving the inverse problem is determining the amount of information contained in the observations and choosing the state vector accordingly. This is a non-trivial problem when using large observational data sets with large errors, such as those from satellite observations. Methane concentrations can be predicted on the basis of emissions by using a chemical transport model (CTM) that solves the 3-D continuity equation for methane concentrations. Here the CTM is the forward model $\mathbf{F}$, the satellite provides a large observation vector $\mathbf{y}$, and we need to choose the resolution at which to optimize the methane emission vector $\mathbf{x}$.

Reducing the dimensionality of the state vector in the inverse problem has two main advantages. It improves the observational constraints on individual state vector elements and it facilitates analytical solution. Reduction can be achieved by aggregating state vector elements. For a state vector of gridded time-dependent emissions, the state vector can be reduced by aggregating grid cells and time periods. However, this introduces error in the inversion as the underlying spatial and temporal patterns of the aggregated emissions are now imposed from prior knowledge and not allowed to be optimized as part of the inversion. The resulting error is called the aggregation error (Kaminski and Heimann, 2001; Kaminski et al., 2001; Schuh et al., 2009).

4.6.2.2 Formulating the inverse problem

Inverse problems are commonly solved using Bayes' theorem,

$$P(\mathbf{x}\,|\,\mathbf{y}) \propto P(\mathbf{y}\,|\,\mathbf{x})P(\mathbf{x}), \tag{2}$$

where $P(\mathbf{x}\,|\,\mathbf{y})$ is the posterior probability density function (pdf) of the state vector $\mathbf{x}$ $(n\times 1)$ given a vector of observations $\mathbf{y}$ $(m\times 1)$, $P(\mathbf{x})$ is the prior pdf of $\mathbf{x}$, and $P(\mathbf{y}\,|\,\mathbf{x})$ is the conditional pdf of $\mathbf{y}$ given the true value of $\mathbf{x}$. Assuming Gaussian distributions for $P(\mathbf{y}\,|\,\mathbf{x})$ and $P(\mathbf{x})$ allows us to write the posterior pdf as

$$P(\mathbf{x}\,|\,\mathbf{y}) \propto \exp\left\{-\frac{1}{2}\left(\mathbf{y}-\mathbf{F}(\mathbf{x})\right)^T \mathbf{S}_{\mathrm{O}}^{-1}\left(\mathbf{y}-\mathbf{F}(\mathbf{x})\right)-\frac{1}{2}\left(\mathbf{x}_{\mathrm{a}}-\mathbf{x}\right)^T \mathbf{S}_{\mathrm{a}}^{-1}\left(\mathbf{x}_{\mathrm{a}}-\mathbf{x}\right)\right\}, \tag{3}$$

where $\mathbf{x}_{\mathrm{a}}$ is the $n\times 1$ prior state vector, $\mathbf{S}_{\mathrm{O}}$ is the $m\times m$ observational error covariance matrix, and $\mathbf{S}_{\mathrm{a}}$ is the $n\times n$ prior error covariance matrix. Here and elsewhere, our notation and

terminology follow that of Rodgers (2000). The most probable solution $\hat{\mathbf{x}}$ (called the maximum a posteriori or MAP) is defined by the maximum of $P(\mathbf{x}\,|\,\mathbf{y})$, i.e., the minimum of the cost function $\mathrm{J}(\mathbf{x})$:

$$\mathrm{J}(\mathbf{x}) = \frac{1}{2}\big(\mathbf{y}-\mathbf{F}(\mathbf{x})\big)^T \mathbf{S}_\mathrm{O}^{-1}\big(\mathbf{y}-\mathbf{F}(\mathbf{x})\big) + \frac{1}{2}\big(\mathbf{x}_\mathrm{a}-\mathbf{x}\big)^T \mathbf{S}_\mathrm{a}^{-1}\big(\mathbf{x}_\mathrm{a}-\mathbf{x}\big). \tag{4}$$

This involves solving

$$\nabla_\mathbf{x}\mathrm{J} = \nabla_\mathbf{x}\mathbf{F}(\mathbf{x})^T \mathbf{S}_\mathrm{O}^{-1}\big(\mathbf{F}(\mathbf{x})-\mathbf{y}\big) + \mathbf{S}_\mathrm{a}^{-1}\big(\mathbf{x}_\mathrm{a}-\mathbf{x}\big) = \mathbf{0}. \tag{5}$$

Solution to Eq. (5) can be done analytically if $\mathbf{F}$ is linear; i.e., $\mathbf{F}(\mathbf{x}) = \mathbf{K}\mathbf{x} + \mathbf{c}$ where $\mathbf{K} \equiv \nabla_\mathbf{x}\mathbf{F} = \partial\mathbf{y}/\partial\mathbf{x}$ is the Jacobian of $\mathbf{F}$ and $\mathbf{c}$ is a constant that can be set to zero in the general case by subtracting $\mathbf{c}$ from the observations. This yields

$$\hat{\mathbf{x}} = \mathbf{x}_\mathrm{a} + \mathbf{G}\big(\mathbf{y}-\mathbf{K}\mathbf{x}_\mathrm{a}\big), \tag{6}$$

where $\mathbf{G} = \hat{\mathbf{S}}\mathbf{K}^T\mathbf{S}_\mathrm{O}^{-1}$ is the gain matrix and $\hat{\mathbf{S}}$ is the posterior error covariance matrix,

$$\hat{\mathbf{S}} = \big(\mathbf{K}^T\mathbf{S}_\mathrm{O}^{-1}\mathbf{K} + \mathbf{S}_\mathrm{a}^{-1}\big)^{-1} \tag{7}$$

The MAP solution can also be expressed in terms of the true value $\mathbf{x}$ as

$$\hat{\mathbf{x}} = \mathbf{x}_\mathrm{a} + \mathbf{A}\big(\mathbf{x}-\mathbf{x}_\mathrm{a}\big) + \mathbf{G}\boldsymbol{\varepsilon}, \tag{8}$$

where $\mathbf{A}$ is the averaging kernel matrix that measures the error reduction resulting from the observations

$$\mathbf{A} = \mathbf{G}\mathbf{K} = \mathbf{I} - \hat{\mathbf{S}}\mathbf{S}_\mathrm{a}^{-1} \tag{9}$$

and $\mathbf{G}\boldsymbol{\varepsilon}$ is the observation error in state space with error covariance matrix $\mathbf{G}\mathbf{S}_\mathrm{O}\mathbf{G}^T$. We have assumed here that errors are unbiased, as is standard practice in the inverse modeling literature. An observational error bias $\mathbf{b}_\mathrm{O}$ would propagate as a bias $\mathbf{G}\mathbf{b}_\mathrm{O}$ in the solution $\hat{\mathbf{x}}$ in Eq. (8).

The analytical solution to the inverse problem thus provides full error characterization as part of the solution. It does require that the forward model be linear. The Jacobian matrix must generally be constructed numerically, requiring n sensitivity simulations with the forward model. Subsequent matrix operations are also of dimension n. This limits the practical size of the state vector. The matrix operations also depend on the dimension m of the observation vector, but this can be easily addressed by splitting that vector into uncorrelated packets, a method known as sequential updating (Rodgers, 2000). Turner and Jacob (2015) provides a detailed description of the aggregation and smoothing errors for reduced-dimension state vectors.

4.6.2.3 Aggregation methods

Aggregation of state vector elements to reduce the state vector dimension introduces aggregation error, as described in Turner and Jacob (2015). The aggregation error can be reduced by grouping elements with correlated errors. Analyzing the off-diagonal structure of a precisely constructed prior error correlation matrix would provide the best objective way to carry out the aggregation, as described by Bocquet (2009), Bocquet et al. (2011), and Wu et al. (2011). We generally lack such information but do have some qualitative knowledge of prior error correlation that can be used to optimize the aggregation. By aggregating regions that have correlated errors we can exploit additional information that would otherwise be neglected in a native-resolution inversion assuming (by default) uncorrelated errors. Here we discuss how one can use Gaussian Mixture Models to reduce the dimension of the state vector.

This method enable consideration of similarity factors besides spatial proximity when aggregating state vector elements. These similarity factors are expressed by vectors of dimension n describing correlative properties of the original native-resolution state vector elements. In the case of a methane source inversion, for example, we can choose as similarity vectors latitude and longitude to account for spatial proximity, but also wetland fraction to account for error correlations in the bottom-up wetland emission estimate used as prior.

Table 4.6-1 lists the similarity vectors chosen for our example problem of estimating methane emissions (Turner et al., 2015). The first two vectors account for spatial proximity, the third represents the scaling factors from the first iteration of an adjoint-based inversion at native resolution (Wecht et al., 2014a), and the others are the source type patterns from the bottom-up inventories used as prior. All similarity vectors are normalized and then weighted by judgment of their importance. We choose here to include initial scaling factors from the adjoint-based inversion because we have them available and they can serve to correct any prior patterns that are grossly inconsistent with the observations, or to identify local emission hotspots missing from the prior. One iteration of the adjoint-based inversion is computationally inexpensive and is sufficient to pick up major departures from the prior.

Table 4.6-1: Similarity vectors for inverting methane emissions in North America [a].

Similarity vector		Weighting factor [b]
1.	Latitude [c]	1.00
2.	Longitude [d]	1.00
3.	Initial scaling factors [e]	0.15
4.	Wetland	0.31
5.	Livestock	0.22
6.	Oil/gas	0.16
7.	Waste	0.15
8.	Coal	0.06
9.	Soil absorption	0.05
10.	Termites	0.02
11.	Biomass burning	0.02
12.	Biofuel	0.01
13.	Rice	0.01
14.	Other	0.01

[a] The $K = 14$ similarity vectors describe prior error correlation criteria for the native-resolution state vector, representing here the methane emission in North America at the $1/2^\circ \times 2/3^\circ$ resolution of the GEOS-Chem chemical transport model. The criteria are normalized and then weighted (weighting factor). Criteria 4–14 are prior emission patterns used in the GEOS-Chem model (Wecht et al., 2014a; Turner et al., 2015).

[b] The weighting factors (dimensionless) measure the estimated relative importance of the different similarity criteria in determining prior error correlations in the state vector. For the prior emission patterns these weighting factors are the fractional contributions to total prior emissions in North America.

[c] Distance in kilometers from the equator.

[d] Distance in kilometers from the prime meridian.

[e] Initial scaling factors from one iteration of an adjoint inversion at the native resolution.

Let $\{\mathbf{c}_1, \ldots, \mathbf{c}_K\}$ represent the K similarity vectors chosen for the problem ($K = 14$ in our example of Table 4.6-1). We assemble them into a $n \times K$ similarity matrix $\mathbf{C}$. We will also make use of the ensemble of similarity vector values for individual state vector elements, which we assemble into vectors $\{\mathbf{c}_1', \ldots, \mathbf{c}_n'\}$ representing the rows of $\mathbf{C}$. Thus:

$$\mathbf{C} = \left[\begin{pmatrix} \vdots \\ \mathbf{c}_1 \\ \vdots \end{pmatrix} \begin{pmatrix} \vdots \\ \mathbf{c}_2 \\ \vdots \end{pmatrix} \cdots \begin{pmatrix} \vdots \\ \mathbf{c}_K \\ \vdots \end{pmatrix} \right] = \begin{bmatrix} (\cdots & \mathbf{c}'_1 & \cdots) \\ (\cdots & \mathbf{c}'_2 & \cdots) \\ & \vdots & \\ (\cdots & \mathbf{c}'_n & \cdots) \end{bmatrix} \tag{10}$$

In this work all of the aggregation methods except for grid coarsening will use the same similarity matrix to construct the restriction operator.

This approach of using a similarity matrix $\mathbf{C}$ to account for prior error covariances bears some resemblance to the geostatistical approach for inverse modeling (e.g., Michalak et al., 2004, 2005; Gourdji et al., 2008; Miller et al., 2012). The geostatistical approach specifies the prior estimate as $\mathbf{x}_a = \mathbf{C}\beta$, where β is a vector of unknown drift coefficients to be optimized as part of the inversion. Here we use the similarity matrix to reduce the dimension of the state vector, rather than just as a choice of prior constraints.

Here we use a Gaussian mixture model (GMM; Bishop 2007) to project the native-resolution state vector onto p Gaussian pdfs using radial basis functions (RBFs). Mixture models are probabilistic models for representing a population comprised of p subpopulations. Each subpopulation is assumed to follow a pdf, in this case Gaussian. The Gaussians are K-dimensional where K is the number of similarity criteria. Each native-resolution state vector element is fit to this ensemble of Gaussians using RBFs as weighting factors.

The first step in constructing the GMM is to define a $p \times n$ weighting matrix $\mathbf{W} = [\mathbf{w}_1, \mathbf{w}_2, \ldots, \mathbf{w}_p]^T$. Each element $w_{i,j}$ of this weighting matrix is the relative probability for native-resolution state vector element j to be described by Gaussian subpopulation i; i.e., "how much does element j look like Gaussian i?". It is given by

$$w_{i,j} = \frac{\pi_i \mathsf{N}(\mathbf{c}'_j \mid \mu_i, \mathbf{\Lambda}_i)}{\sum_{k=1}^{p} \pi_j \mathsf{N}(\mathbf{c}'_j \mid \mu_k, \mathbf{\Lambda}_k)}. \tag{11}$$

Here $\mathbf{c}'_j$ is the jth row of the similarity matrix $\mathbf{C}$, μ_i is a $1 \times K$ row vector of means for the ith Gaussian, $\mathbf{\Lambda}_i$ is a $K \times K$ covariance matrix for the ith Gaussian, and $\boldsymbol{\pi} = [\pi_1, \ldots, \pi_p]^T$ is the relative weight of the p Gaussians in the mixture. $\mathsf{N}(\mathbf{c}'_j \mid \mu_i, \mathbf{\Lambda}_i)$ denotes the probability density of vector $\mathbf{c}'_j$ on the normal distribution of Gaussian i. We define a $p \times K$ matrix M with rows μ_i and a $K \times K \times p$ third-order tensor $\mathsf{L} = [\mathbf{\Lambda}_1, \ldots, \mathbf{\Lambda}_p]$ as the set of covariance matrices.

Projection of the native-resolution state vector onto the GMM involves four unknowns: $\mathbf{W}$, $\boldsymbol{\pi}$, M, and L. This is solved by constructing a cost function to estimate the parameters of the Gaussians in the mixture model using maximum likelihood:

$$\mathrm{J}_{\mathrm{GMM}}(\mathbf{C} \mid \pi, \mathsf{M}, \mathsf{L}) = \sum_{j=1}^{n} \ln\left\{ \sum_{i=1}^{p} \pi_i \mathsf{N}(\mathbf{c}'_j \mid \mu_i, \boldsymbol{\Lambda}_i) \right\} \tag{12}$$

Starting from an initial guess for $\boldsymbol{\pi}$, M, and L we compute the weight matrix $\mathbf{W}$ using Eq. (11). We then differentiate the cost function with respect to $\boldsymbol{\pi}$, M, and L, and set the derivative to zero to obtain (see Bishop, 2007)

$$\mu_i = \Psi_i \sum_{j=1}^{n} w_{i,j} \mathbf{c}'_j \tag{13}$$

$$\boldsymbol{\Lambda}_i = \Psi_i \sum_{j=1}^{n} w_{i,j} \left(\mathbf{c}'_j - \mu_i\right)^T \left(\mathbf{c}'_j - \mu_i\right) \tag{14}$$

$$\pi_i = \frac{1}{n \Psi_i} \tag{15}$$

where:

$$\Psi_i = \sum_{j=1}^{n} \frac{1}{w_{i,j}} \tag{16}$$

The weights are re-calculated from the updated guesses of $\mathbf{W}$, $\boldsymbol{\pi}$, M, and L from Eqs. (13) to (16), and so on until convergence. The final weights define the restriction operator as $\boldsymbol{\Gamma}_{\omega} = \mathbf{W}$. The computational complexity for the expectation-maximization algorithm is $\mathsf{O}(nK + pn^2)$ (Chen et al., 2007); however, the actual runtime will be largely dictated by the convergence criteria. Here we use an absolute tolerance of $\tau < 10^{-10}$ where

$$\begin{aligned} \tau = & \sum_i \sum_j \left| \mathsf{M}_{i,j} - \mathsf{M}^{\mathring{a}}_{i,j} \right| \\ & + \sum_i \sum_j \sum_k \left| \mathsf{L}_{i,j,k} - \mathsf{L}^{\mathring{a}}_{i,j,k} \right| \\ & + \sum_i \left| \pi_i - \pi_i^{\mathring{a}} \right|, \end{aligned} \tag{17}$$

and the superscript star indicates the value from the previous iteration.

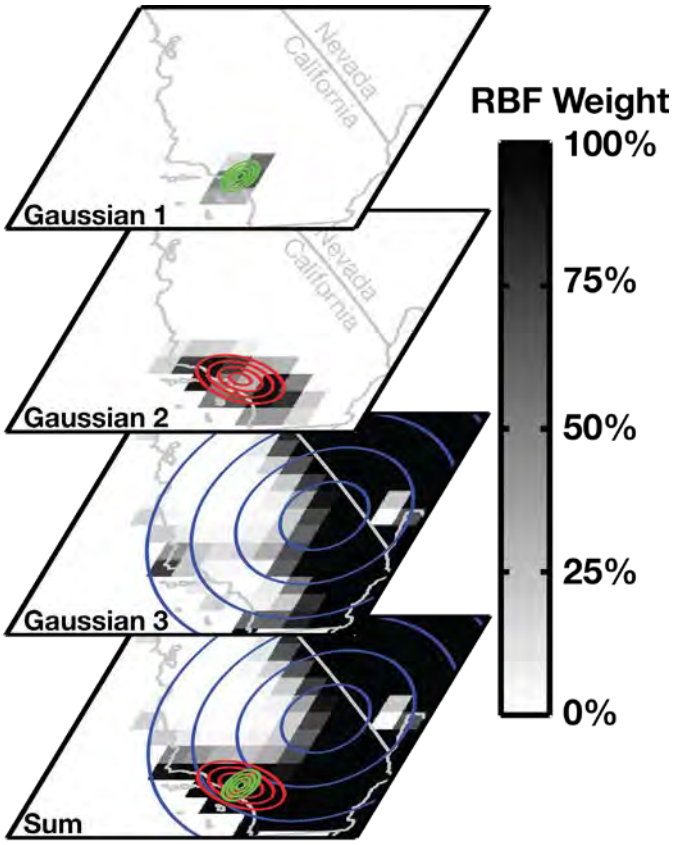

Figure 4.6-1: Gaussian mixture model (GMM) representation of methane emissions in Southern California with Gaussian pdfs as state vector elements. The Gaussians are constructed from a similarity matrix for methane emissions on the 1/2°×2/3° horizontal resolution of the GEOS-Chem CTM used as forward model for the inversion. The figure shows the dominant three Gaussians for Southern California with contours delineating the 0.5, 1.0, 1.5, and 2.0 σ spreads for the latitude–longitude dimensions. The RBF weights $\mathbf{w}_1$, $\mathbf{w}_2$, and $\mathbf{w}_3$, and of the three Gaussians for each 1/2°× 2/3° grid square are also shown along with their sum. (from: Turner and Jacob, 2015; their Fig. 2).

The GMM allows each native-resolution state vector element to be represented by a unique linear combination of the Gaussians through the RBFs. For a state vector of a given dimension, defined by the number of Gaussian pdfs, we can achieve high resolution for large localized sources by sacrificing resolution for weak or uniform source regions where resolution is not needed. This is illustrated in Fig. 4.6-1 with the resolution of Southern California in an inversion of methane sources for North America. The figure shows the three dominant Gaussians describing emissions in Southern California and the corresponding RBF weights for each native-resolution grid square. Gaussian 1 is centered over Los Angeles and is highly localized, Gaussian 2 covers the Los Angeles Basin, and Gaussian 3 is a Southern California background. The sum of these three Gaussians accounts for most of the emissions in Southern California and Nevada (which is mostly background). Additional Gaussians (not shown) resolve the southern San Joaquin Valley (large livestock and oil/gas emissions) and Las Vegas (large emissions from waste).

4.6.3 Estimating methane emissions

4.6.3.1 Global inversion of methane emissions

Returning to the problem of estimating methane sources, we begin by using the GOSAT data to infer global methane emissions at 4°×5° resolution. We use an adjoint-based four-dimensional variational data assimilation system (Henze et al., 2007; Wecht et al., 2012, 2014a) to infer the global sources and will use the GMM-based methodology to infer regional sources.

Table 4.6-2: 2009–2011 methane emissions[a].

Source Type	Contiguous US		North America		Global	
	Prior	Posterior[b]	Prior	Posterior[b]	Prior	Posterior
Total	31.4	51.3–52.5	63.3	88.5–91.3	537	539
Wetlands	5.9	9.0–10.1	20.4	22.9–23.7	164	169
Livestock	8.9	12.6–17.0	14.5	20.0–25.7	111	116
Oil/Gas	5.4	8.7–13.4	10.8	15.5–22.3	69	67
Waste[c]	5.5	8.0–8.5	9.7	13.4–14.5	60	65
Coal	4.0	4.7–6.5	4.3	5.0–6.8	47	30
Rice	0.4	0.8–0.9	0.5	0.9–1.0	38	45
Open Fires	0.1	0.1	1.0	0.9	17	16
Other[d]	1.1	1.6–1.7	2.2	3.0–3.3	31	32
Natural[e]	7.5	9.8–11.1	25.0	25.1–26.2	176	181
Anthropogenic[f]	25.0	40.2–42.7	41.9	62.3–66.2	361	358

[a] Emissions are in Tg a^{-1}. Prior emissions are mainly from EDGARv4.2 for anthropogenic sources and Pickett-Heaps et al. (2011) for wetlands (see Appendix).

[b] Range from two inversions with different assumptions for prior error (see text).

[c] Including landfills and waste water.

[d] Including fuel combustion, termites, and soil absorption.

[e] Including wetlands, open fires, termites, and soil absorption.

[f] Including livestock, oil/gas, waste, coal, rice, and fuel combustion.

The state vector for the global inversion consists of scaling factors for emissions at 4°×5° resolution for June 2009–December 2011. The prior emissions are mainly from the EDGARv4.2 inventory for anthropogenic sources (European Commission, 2011), and Pickett-Heaps et al. (2011) for wet- lands. The error covariance matrices are taken to be diagonal, implying no error correlation on the 4°×5° grid. We assume 50% error variance on the prior for 4°×5° grid cells as in Monteil et al. (2013).

Observational error variances are estimated following Heald et al. (2004) by using residual standard deviations of the differences between observations and the GEOS-Chem simulation with prior emissions. As shown by Heald et al. (2004), this residual error provides an estimate of the total observational error needed for the inversion, summing the contributions from instrument retrieval, representation, and model transport errors. We find that the resulting observational error variances are lower than the local retrieval error variances reported by Parker et al. (2011) for 58% of the observations, and in those cases we use the latter instead. The implication is that the Parker et al. (2011) error estimates may be too high but provide a conservative estimate of the observational error.

The GEOS-Chem forward model and its adjoint are as described by Wecht et al. (2014a). We optimize methane emissions from 1 June 2009 to 1 January 2012. The forward model is initialized on 1 January 2009 with concentrations from Wecht et al. (2014a). The 5-month spin-up allows for the establishment of gradients driven by synoptic motions and effectively removes the influence of the initial conditions.

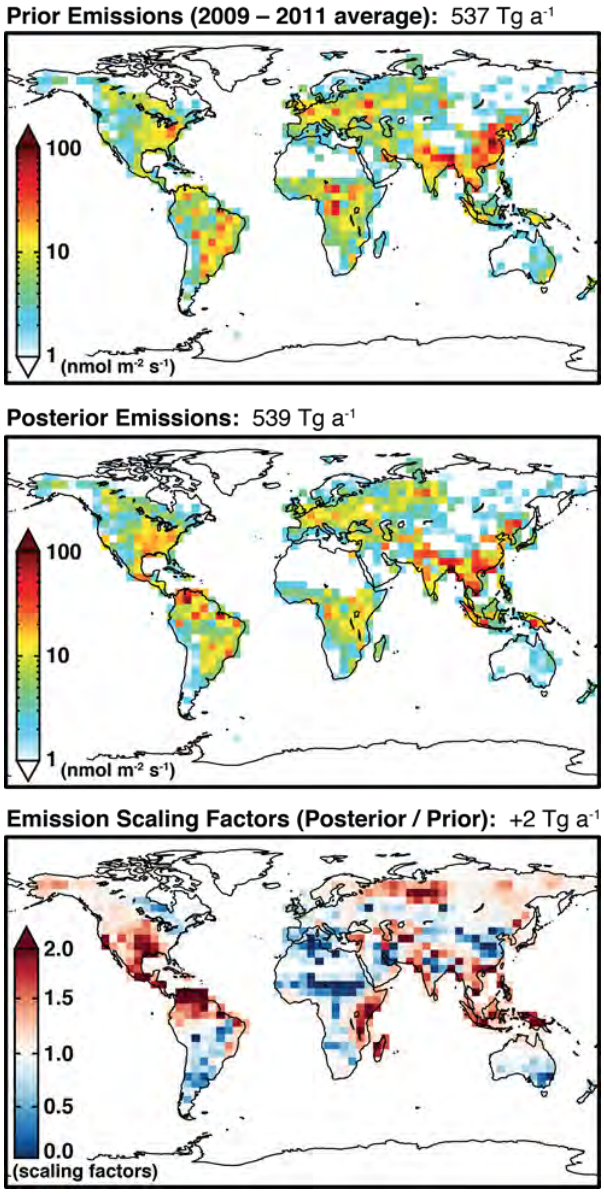

Fig. 4.6-2. Optimization of methane emissions for 2009–2011 at 4°×5° horizontal resolution using GOSAT observations. The panels show prior emissions, posterior emissions, and the ratio between the two. (from: Turner et al., 2015; their Fig. 3).

Figure 4.6-2 shows the prior and posterior 2009–2011 emissions. The total posterior methane emission is 539 Tg a^{-1}, unchanged from the prior (537 Tg a^{-1}). This source is within the 548^{+21}_{-22} Tg a^{-1} range of current estimates reported by Kirschke et al. (2013) and IPCC (2013). However, we find large regional differences compared to the prior. Emissions from China are revised downward by 50% from 29.2 to 14.7 Tg a^{-1}, consistent with Bergamaschi et al. (2013), who find that EDGARv4.2 Chinese coal emissions are too large. This overestimate in Chinese methane emissions is also seen by Bruhwiler et al. (2014), who assimilated the 2000–2010 NOAA surface observations into CarbonTracker using an ensemble Kalman filter. Emissions in India are also too high, while emissions in Southeast Asia are too low. Emissions from wetlands in central Africa are

too high. Emissions in northern South America are too low. Corrections in North America are discussed in the next section.

We inferred the contributions from different source types to our posterior emissions by assuming that the prior inventory correctly partitions the methane by source type in each 4°×5° grid cell. This does not assume that the global distribution of source types is correct in the prior, only that the local identification of dominant sources is. We find only modest changes to the global partitioning by source types, with the exception of coal and rice, partly reflecting regional offsets. For example, wetland emissions increase globally by only 5 Tg a^{-1} but decrease by 24 Tg a^{-1} in the African wetlands, while increasing by 10 Tg a^{-1} in northern South America.

4.6.3.2 North American inversion of methane emissions

We then optimize methane emissions over North America by using the nested GEOS-Chem simulation at 1/2°×2/3° horizontal resolution (~50 km × 50 km) over North America. Time-dependent boundary conditions for this nested simulation are from the global model at 4°×5° horizontal resolution using the posterior emissions derived above. We only solve for the spatial distribution of emissions, assuming that the prior temporal distribution is correct.

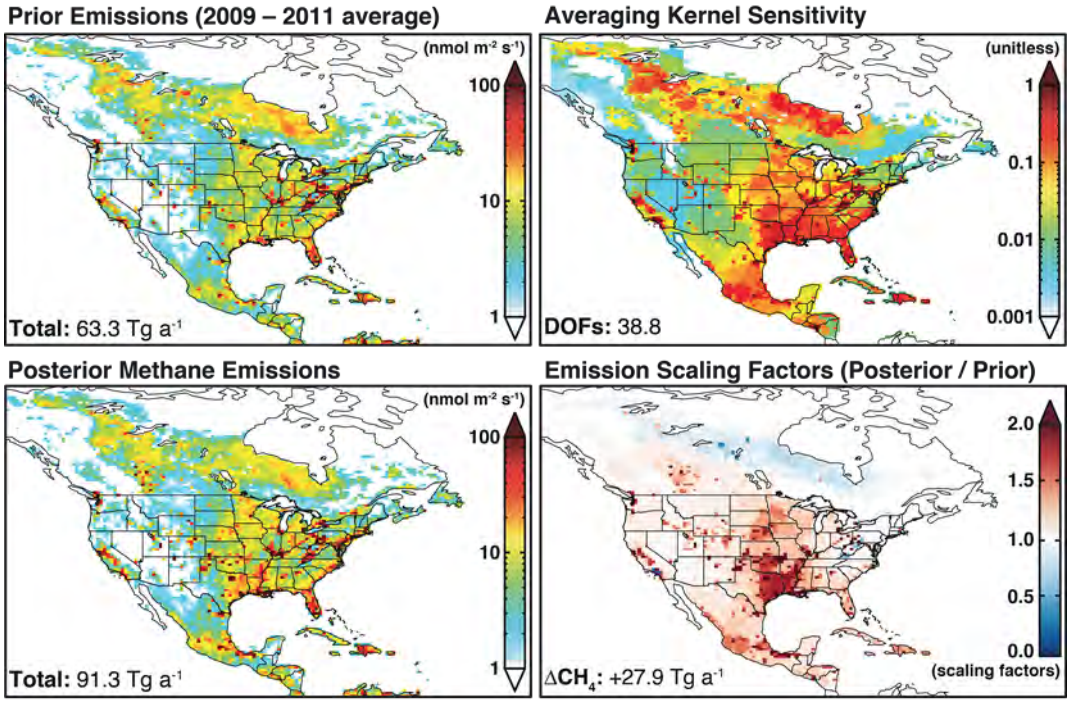

Fig. 4.6-3. Methane emissions in North America in 2009–2011. The left panels show the prior and posterior emissions and the bottom right panel shows the scaling factors. The top right panel shows the diagonal elements of the averaging kernel matrix for the methane emission inversion. The degrees of freedom for signal (DOFS) is the trace of the averaging kernel matrix. (from: Turner et al., 2015; their Fig. 4).

As discussed in Section 4.6.2.3, the dimension of the emissions state vector for the nested North American inversion is optimally reduced from the native 1/2°×2/3° resolution (n = 7366) in order to (1) improve the observational constraints on individual state vector elements and (2) enable an analytical inversion with full error characterization. This is done by aggregating similar state vector elements with a Gaussian mixture model (Bishop, 2007). We find that an optimal reduction with negligibly small aggregation error can be achieved using 369 radial basis functions (RBFs) with Gaussian kernels. The RBFs are constructed from estimation of the factors driving error correlations between the native-resolution state vector elements including spatial proximity, correction from one iteration of an adjoint-based inversion at 1/2°×2/3° resolution, and prior source type distributions. Including the correction from the adjoint-based inversion allows us to account for sources not included in the prior. Each 1/2°×2/3° native-resolution grid square is projected onto an aggregated state vector using the RBFs. This preserves native resolution where needed (in particular for large point sources) and aggregates large regions where emissions are uniformly small.

Our optimal estimate of North American emissions was obtained by analytical solution to Eq. (5) using the methodology described in Section 4.6.2.1. This analytical approach provides the posterior covariance matrix $\hat{\mathbf{S}}$ and averaging kernel matrix $\mathbf{A}$ as part of the solution and thus fully characterizes the errors and information content of the inversion results.

The observational error covariance matrix is assumed diagonal with terms specified as the larger of the residual error variance and the retrieval error variance, same as for the global inversion. The prior error covariance matrix is assumed diagonal because the radial basis functions are designed to capture spatial correlations in the emissions. We assume 100% error on emissions at the native 1/2°×2/3° resolution. For RBFs encompassing larger spatial regions, we assume that the error is reduced following the central limit theorem:

$$S_{\mathrm{a},\{i,i\}} = \frac{s_{\mathrm{a}}}{\sqrt{\sum_j w_{i,j}}}, \tag{18}$$

where $S_{\mathrm{a},\{i,i\}}$ is the ith diagonal of $\mathbf{S}_{\mathrm{a}}$, s_{a} is the prior uncertainty at the native resolution (100%), and the summation is for the weights of the ith RBF over all 1/2°×2/3° grid squares (index j). This error reduction assumes that the errors on the native-resolution grid cells are independent and identically distributed, which may be overly optimistic. We examined the sensitivity to this assumption by conducting an alternate inversion with a relative error of 30% for all state vector elements, similar to the approach taken by Wecht et al. (2014a) using a hierarchial clustering method for the state vector.

Figure 4.6-3 shows the prior and posterior 2009–2011 emissions. Total posterior emissions in North America (Table 4.6-2) are 44% higher than the prior, with large increases in the southern–

central US and weak decreases for the Canadian wetlands. Contiguous US emissions are 52 Tg a^{-1}, 70% higher than the prior. The broad correction patterns are consistent with the coarse global results in Fig. 4.6-2 that used a completely different inversion method. Our sensitivity inversion assuming 30% prior error on all state vector elements yields the same North American and contiguous US totals to within 3%.

We evaluated the posterior emissions in a GEOS-Chem simulation over North America by comparison to the independent observations from the NOAA network. We find great improvement in the ability of the model to reproduce these observations, as illustrated by the scatterplots of Fig. 4.6-4. The reduced-major-axis (RMA) regression slopes improve from 0.72 to 1.03 for the NOAA/ESRL tall tower network, from 0.75 to 0.94 for the NOAA/ESRL aircraft profiles, and from 0.67 to 1.01 for the NOAA surface flasks.

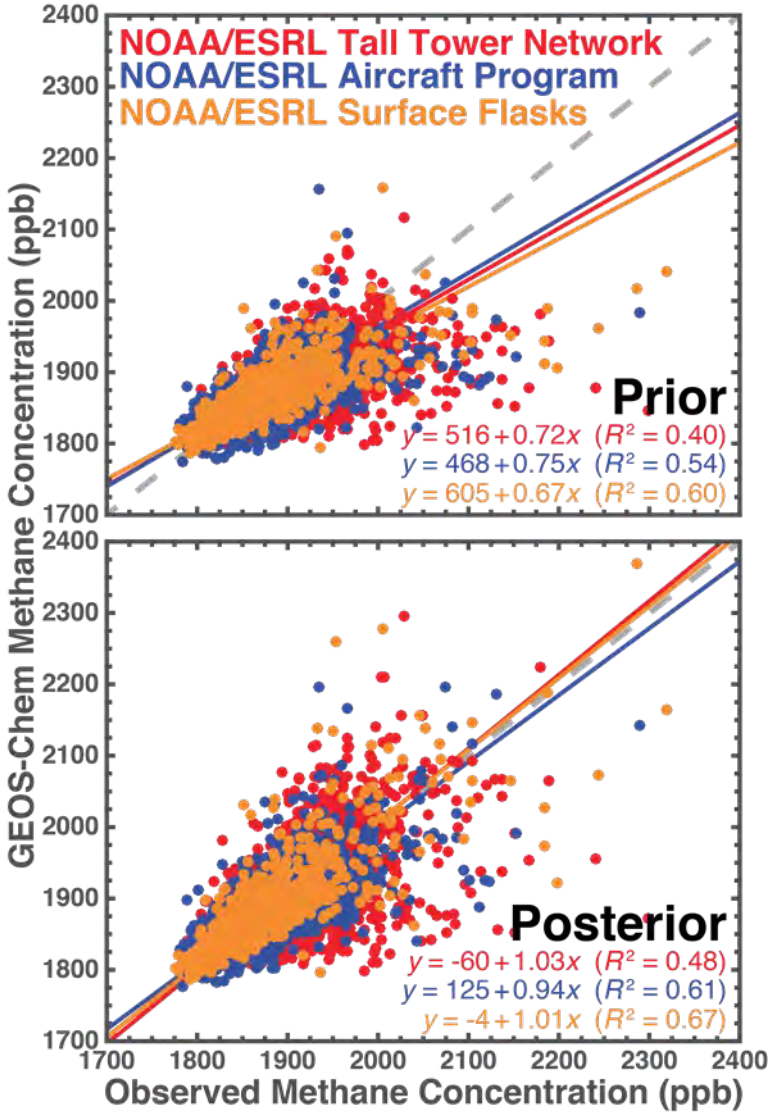

Fig. 4.6-4. Evaluation of the GOSAT inversion of methane emissions for North America with independent data sets. The scatterplots show comparisons of GEOS-Chem (1/2°×2/3° resolution) methane concentrations with observations from the NOAA/ESRL tall tower network (red), NOAA/ESRL aircraft program (blue), and the NOAA/ESRL surface flask network (orange), using prior emissions (top) and posterior emissions (bottom). The 1 : 1 lines (dashed) and reduced-major-axis (RMA, solid) linear regressions are also shown. (from: Turner et al., 2015; their Fig. 5).

Another independent evaluation of our posterior emissions is the estimate for California. California's methane emissions have been extensively studied with aircraft and ground-based observations over the past few years in order to address statewide greenhouse gas regulation targets (Zhao et al., 2009; Wunch et al., 2009; Hsu et al., 2010; Peischl et al., 2012; Wennberg et al., 2012;

Jeong et al., 2012, 2013; Peischl et al., 2013; Santoni et al., 2014; Wecht et al., 2014b). Figure 4.6-5 shows that our posterior emissions are 20% higher than the EDGARv4.2 prior inventory for the state of California and 50% lower for the Southern California Air Basin (SoCAB). Other studies constrained with dense aircraft and ground-based observations are consistent with ours. Wecht et al. (2014b) previously found that GOSAT observations were not sufficiently dense to constrain methane emissions in California. However, they only used a 2-month record and tried to constrain emissions at 1/2°×2/3° resolution, incurring large smoothing error. By using a longer time record and an optimally defined state vector, we achieve much better success.

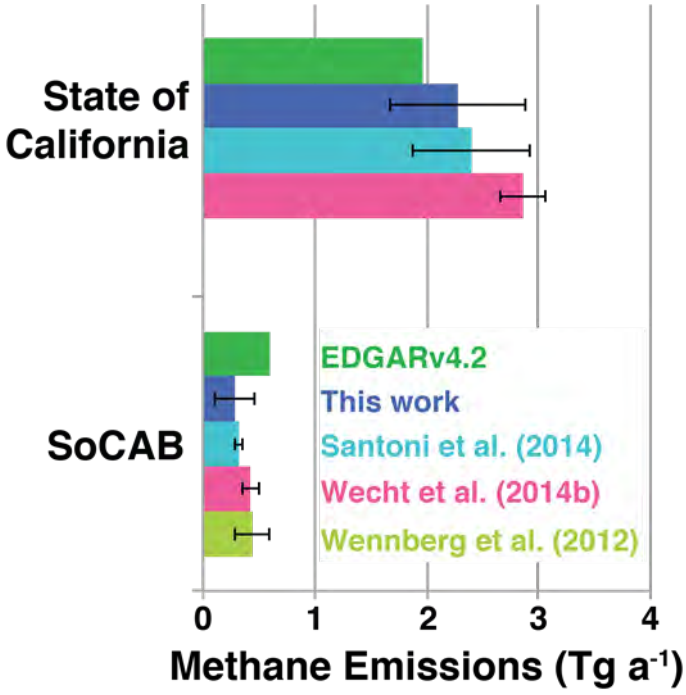

Fig. 4.6-5. Methane emissions for the state of California (top) and for the Southern California Air Basin (SoCAB; bottom). Our posterior emissions (this work) are compared to prior emissions (EDGARv4.2) and to previous inverse estimates constrained by surface and aircraft observations. SoCAB is defined following Wennberg et al. (2012) as the domain 33.5–34.5° N, 117–119° W. (from: Turner et al., 2015; their Fig. 6).

Figure 4.6-3 (top right panel) shows the averaging kernel sensitivities for the North American methane emission inversion, defined as the diagonals of the averaging kernel matrix. The inversion has 39 degrees of freedom for signal (DOFs), meaning that we can exactly constrain 39 pieces of information in the distribution of methane emissions. This information is spread over the continent and mixed with prior constraints as described by the averaging kernel matrix. We can use the averaging kernel sensitivities in Fig. 4.6-3 to determine which regions are most responsive to the inversion. These include California, the Canadian wetlands, and the southeastern and central US.

Large isolated point sources such as the US Four Corners (a large source of coalbed methane at the corner of Arizona, New Mexico, Colorado, and Utah) are also strongly sensitive to the inversion.

We see from Fig. 4.6-3 that the prior underestimate of North American methane emissions is largely due to the central US, the Canadian Oil Sands, central Mexico, California, and Florida. Various large point sources such as the US Four Corners also contribute. We also find regions where the prior is too high, including the Hudson Bay Lowlands, SoCAB, and parts of Appalachia. This suggests that oil/gas and livestock emissions are higher than given in EDGARv4.2, while coal emissions are lower. The overestimate in SoCAB is likely because EDGARv4.2 uses urban and rural population as a spatial proxy for landfills and waste water (Wunch et al., 2009). The underestimate in Florida is most likely due to wetland sources.

As with the global inversion, we infer the contributions from different methane source types by assuming that the prior inventory correctly attributes the source types in a given $1/2^{\circ}\times2/3^{\circ}$ grid cell. Again, this does not assume that the prior distribution is correct, only that the identification of locally dominant sources is correct. Results are shown in Fig. 4.6-6. We see that the increase relative to the prior is mainly driven by anthropogenic sources. This can be compared to the US EPA anthropogenic inventory (EPA, 2014), which is based on more detailed bottom-up information than EDGARv4.2 but is only available as a national total. We find an anthropogenic source for the contiguous US of 40.2–42.7 Tg a^{-1}, as compared to 27.0 Tg a^{-1} in the US EPA inventory. The largest differences are for the oil/gas and livestock sectors. Depending on the assumptions made regarding the prior error, oil/gas emissions from our inversion are 13–74% higher than the EPA estimate and contribute 17–26% of contiguous US methane emissions. Livestock emissions are 36–85% higher than the EPA estimate and contribute 24–33% of contiguous US methane emissions. Waste and coal emissions are also higher in our posterior estimate than in the EPA inventory.

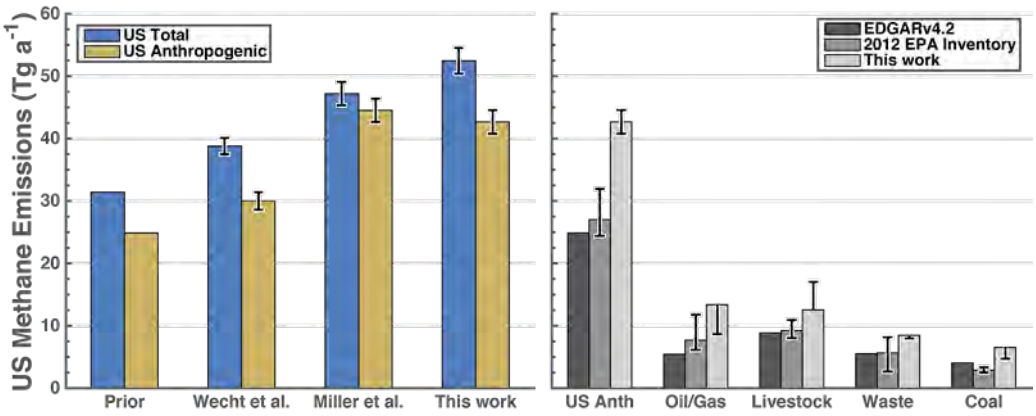

Fig. 4.6-6. Methane emissions in the contiguous US. The left panel shows our best estimates of total and anthropogenic emissions (this work) compared to the prior (EDGARv4.2 for anthropogenic sources, Pickett-Heaps et al. (2011) for wetlands) and the previous inverse studies of Wecht et al. (2014a) and Miller et al. (2013). The right panel partitions US anthropogenic emissions by source types and compares our results (this work) to EDGARv4.2 and to the 2012 EPA inventory (EPA, 2014). Error bars on sectoral emissions for our results are defined by the sensitivity inversion with 30% prior uncertainty for all state vector elements. (from: Turner et al., 2015; their Fig. 7).

4.6.4 Conclusions

The sources and sinks of atmospheric methane have proved difficult to constrain (Turner et al., 2017). Here we presented results from a case study examining global and regional methane emissions sources. 31 months of observations from GOSAT were used to quantify the methane sources and were found to be in good agreement with regional estimates obtained from focused field campaigns. The observations were used in both an adjoint-based and analytical inversion methodology. The analytical inversion used a reduced-dimension state vector with the state vector defined by radial basis functions using a Gaussian mixture model. The case study presented here demonstrates the potential for further monitoring of methane emissions using satellite observations.

4.7 Joint analysis of CO_2 and CH_4 inversion fluxes to refine anthropogenic CO_2 emissions: A case study of East Asia

Tazu Saeki[1] and Prabir K. Patra[2]

1) National Institute for Environmental Studies (NIES), Japan

2) Japan Agency for Marine-Earth Science and Technology (JAMSTEC), Japan

4.7.1 Introduction

An atmospheric inverse modeling, so called a top-down approach, is an effective way to estimate global and regional greenhouse gas (GHG) emissions by an atmospheric transport model and precise measurements of GHG concentrations. The inverse modeling assumes anthropogenic emissions due to fossil fuel consumption and cement production (FFC) are a known quantity, because the emissions are calculated from better known industrial indicators, e.g. the gross domestic product (GDP), import/mining of energy resources, and energy intensity (energy consumed per unit of GDP). Thus, any bias (uncertainty is assumed 0 in inverse models) in the FFC emissions would introduce systematic bias in estimation of the terrestrial (residual) fluxes by inverse modelling.

Recent bottom-up studies have pointed out that the maximum uncertainty in FFC CO_2 emissions is clearly found for China (Guan et al. 2012; Liu et al. 2015; Korsbakken et al. 2016). A top-down model assessment from seven inverse models found that an annual CO_2 sink in East Asia (China, Japan, Korea and Mongolia) increased between 1996–2001 and 2008–2012 by 0.56 PgC on an average (Thompson et al., 2016). The effort to validate the inverted CO_2 fluxes using independent aircraft CO_2 observations did not provide conclusive results as the modeled concentrations fairly matched the observed vertical gradients between the surface and middle troposphere as well as the concentrations near the surface layer for a large range (~1 PgC/yr) of residual CO_2 sinks over East Asia alone.

On the other hand, we found the inversion results of CH_4 emissions could be successfully validated using independent aircraft observations over Japan, which suggested an overestimation of East Asian CH_4 emission increase by bottom-up inventories (Patra et al., 2016; Section 4.8 in this issue). Here we introduce a new approach to use the CH_4 inversion results to refine the increase rate of bottom-up FFC CO_2 emissions for East Asia, and show that no systematic increase in land CO_2 uptake over East Asia may be required (as in Saeki and Patra, 2017). The current study used only surface data for GHG concentrations in inversion analysis, but the results have equal implications for the use of satellite measurements in an inverse modelling system.

4.7.2 Data

We use CO_2 observations from 66 sites from GLOBALVIEW-CO2 (2013) data products for

CO_2 inversion analysis to derive CO_2 fluxes as described in 4.7.3.2. The GLOBALVIEW dataset consists of interpolated and smoothed data created from weekly or biweekly flask measurements at each site. The data uncertainties are assigned to monthly-mean CO_2 to account for the ability of transport models to simulate atmospheric data and the observational accuracy.

4.7.3 Method

4.7.3.1 Outline

First, we conduct CO_2 inversions with 3-sets of a priori FFC emissions. We then derive a scaling factor from CH_4 inversion results to correct an increase rate of FFC CO_2 emissions. The CH_4 inversion has been validated by independent atmospheric measurements. Because CO_2 and CH_4 emissions have strong correlations for some of the emission categories, we took liberty to apply the CH_4-derived scaling factor to refine the a priori FFC CO_2 emissions. The CH_4-based FFC emission corrections to inverted CO_2 fluxes are applied a posteriori.

4.7.3.2 CO_2 inversion

CO_2 inversions are performed for 2001–2012 to optimize fluxes from 84 regions of the globe using the JAMSTEC's atmospheric chemistry-transport model (ACTM) and CO_2 observations from 66 sites taken from GLOBALVIEW-CO2 (2013) data products (Saeki and Patra, 2017; Thompson et al. 2016). We have used three a priori FFC CO_2 emission maps from (1) CDIAC: emissions of top-20 countries from CDIAC (Boden et al. 2016) distributed using EDGAR4 emission maps (Olivier et al. 2014; 2010 emission maps repeated for the latter years), (2) CARBONES: a project of the European Union (I. van der Laan-Luijkx, personal communication, 2015; as in Thompson et al. 2016), and (3) the IEA (International Energy Agency) emissions for South Asia, East Asia, Southeast Asia and rest of the world distributed using CARBONES emission maps (as in Thompson et al. 2016; referred to as IEA) (Fig. 4.7-1).

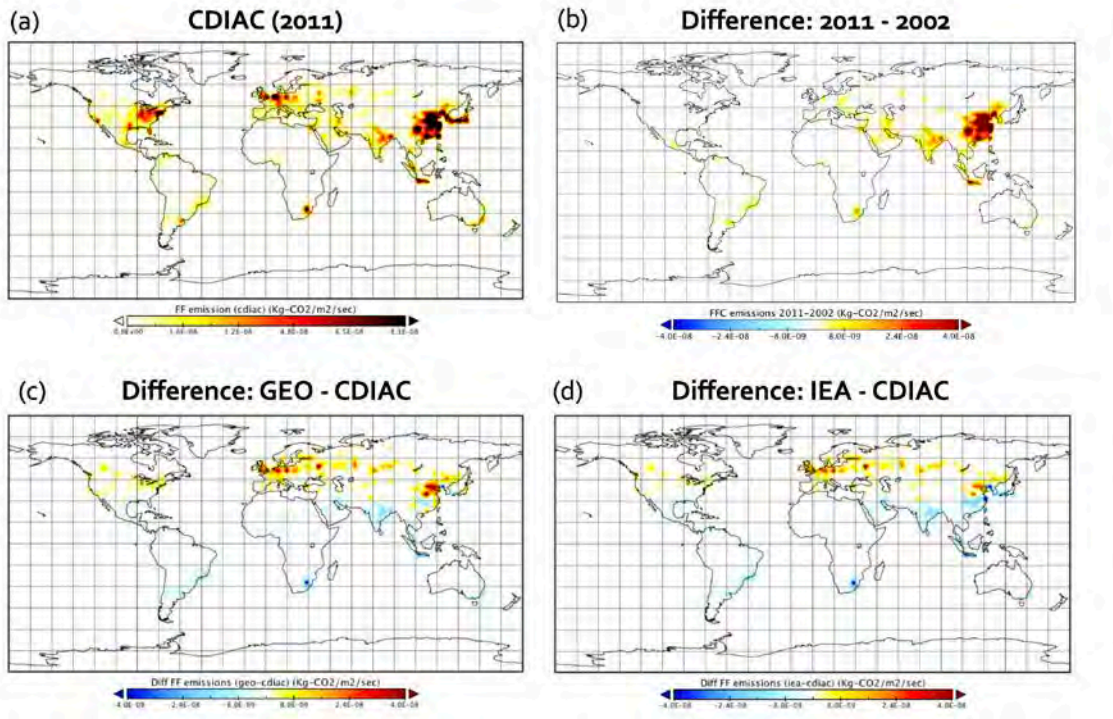

Figure 4.7-1. FFC CO_2 emission map of the CDIAC inventory in 2011 (a), and the differences between CDIAC emissions for 2011 and 2002 (b), GEOCARBON and CDIAC emissions in 2011 (c), and IEA and CDIAC emissions in 2011 (d).

4.7.3.3 FFC CO_2 emission scaling factor from CH_4 inversion

CH_4 inversions are performed for 53-land regions only, using ACTM forward simulations and atmospheric data from 39 sites (Patra et al. 2016; Section 4.8. in this issue;). The CH_4 inversions suggested that increase rate of estimated CH_4 emissions are 39% (9 Tg) lower than that of a EDGAR42FT inventory during 2002-2012 (Fig. 4.7-2a). The EDGAR42FT inventory, used as a priori, suggested an increase of 23 Tg-CH_4 emissions from East Asia, which is contributed entirely by the anthropogenic emission increase rate in China. The validation using independent aircraft measurement over Sendai by Tohoku University (Umezawa et al. 2014) showed clearly that forward simulations with the a priori fluxes overestimated the observed CH_4 increase but that with the inverted flux showed good agreement for the net concentration increase during 2002-2012 (see Section 4.8. for details). We derive a scaling factor of 0.59 (=1.53/2.61, a ratio of slopes of the linear fits for a posteriori and a priori emissions in Fig. 4.7-2a) to correct an increase rate of a priori CH_4 emissions in East Asia during 2002-2012. The slope of the fitted line to a posteriori CH_4 emissions agrees well with a recent inventory emission estimate by Peng et al. (2016). They find smaller number of deep mining fields in China, which have high CH_4 emission factors, compared that previously assumed.

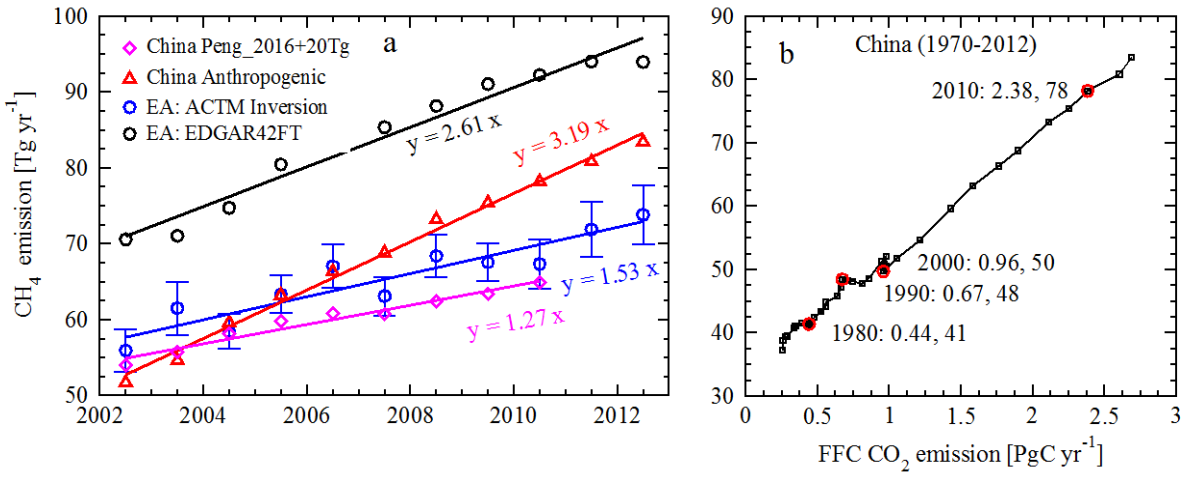

Figure 4.7-2. (a) Comparisons of CH_4 inversion results (black: a priori; blue: a posteriori) for the East Asia (EA) region with the EDGAR estimated anthropogenic emissions for China. The linear fits to the annual mean values are shown as lines, with slopes being marked along the fitted lines. Recent inventory based CH_4 emissions are plotted for a comparison (magenta line; source: Peng et al., 2016). (b) The linear relationship of anthropogenic CO_2 and CH_4 emissions for China over the period of 1970-2012 is evident in the emission inventories, e.g., EDGAR42FT. The inter-decadal values are marked by text and red circles.

4.7.3.4 Refinement of inverted CO_2 fluxes by revised FFC CO_2 emissions

Since the anthropogenic emissions of both CO_2 and CH_4 increase linearly in the emission inventory, we apply a scaling factor of 0.59 derived from the validated CH_4 inversion results, to FFC CO_2 emission "increase rate" for the period 2003–2014, relative to the emissions for 2002 from CDIAC inventory. The application of this CH_4-inversion-derived scaling factor to the CO_2 emission increase rate assumes constant CH_4/CO_2 emission ratio over the periods of our analyses and is deemed valid as per the linearity maintained in anthropogenic emission inventories of CO_2 and CH_4 over the period of 1970–2012 (EDGAR4; Fig. 4.7-2b). The increase in emissions of both CO_2 and CH_4 in East Asia is linked to the Chinese coal industry (Fig. 4.7-3); CH_4 is emitted during the coal mining, while emissions of CO_2 occur during the consumption of coal primarily in power plants and industrial combustions (EDGAR42FT2010). About 75% of FFC CO_2 emissions and up to 40% of anthropogenic CH_4 emissions are caused due to the coal/oil industry (mining and burning), which have produced 82% and 72% of the increase in their emissions, respectively, in the period 2002–2010 (EDGAR42FT).

The inverse model land (residual) fluxes are corrected for the FFC CO_2 emission bias (following Peylin et al. 2013; Thompson et al. 2016). Note that the method is a good approximation when biases in assumed FFC CO_2 emission only in influence land CO_2 flux of the same region, but

this is probably not the case because our regional fluxes are poorly constrained by observational data (Saeki and Patra 2017).

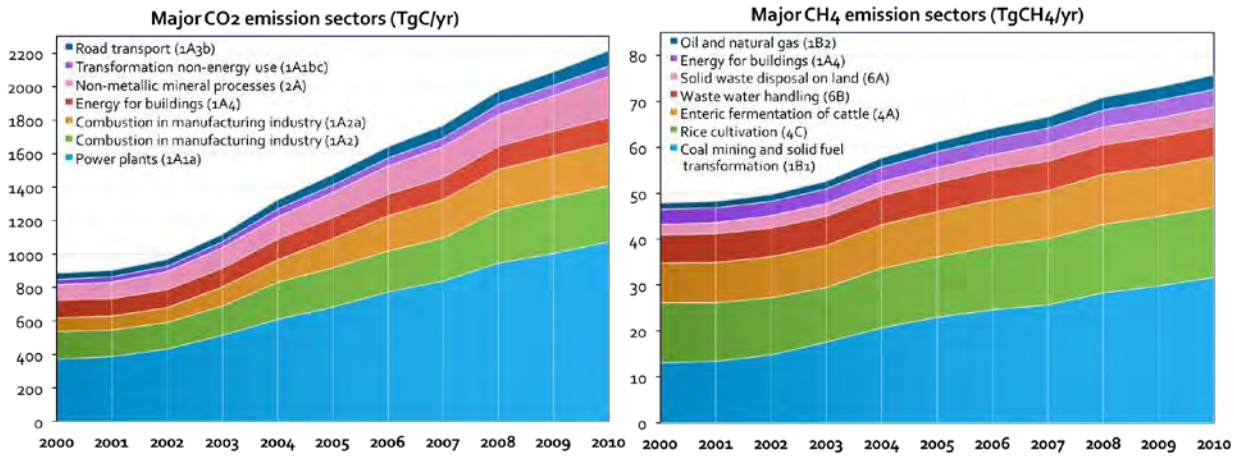

Figure 4.7-3. Time series of Chinese CO_2 and CH_4 emissions for the major anthropogenic activity sectors as provided by the EDGAR database. The CO_2 emission increase rate from power plants sector shows very close correspondence with CH_4 emission increase due to coal mining and solid fuel transformation. The total anthropogenic emissions for CO_2 and CH_4 are also closely correlated in EDGAR (Fig. 4.7-2b).

4.7.4 Case Studies

4.7.4.1 A case study for East Asian CO_2 balance

We estimated land CO_2 fluxes with three different a priori FFC CO_2 emissions by the 84-region inversion with JAMSTEC's ACTM. We find the FFC CO_2 emissions as per the CDIAC inventory method are always higher compared to the CARBONES and IEA inventories. A fairly compensatory land CO_2 fluxes are estimated for the East Asia region with the interannual variations (IAVs) being opposite in phase. A biased higher (lower) FFC CO_2 emission will lead to artificially stronger (weaker) biospheric CO_2 sink over a given land region. Our results suggested only about 60–67% of the FFC CO_2 emission bias is transferred to land uptake increase for the East Asia region, implying that the estimated land fluxes by inversion for other parts of the world are not free from FFC emission uncertainties in China.

Figure 4.7-4a shows corrected FFC emission increase rate by applying the CH_4 scaling factor after 2003 on the CDIAC FFC emissions (=GCP bottom-up), which has about 0.6 Pg/yr lower than the original CDIAC estimates. When scaled anthropogenic CO_2 emissions are used, we find no systematic increase in land CO_2 uptake over East Asia during 1993-2010 or 2000-2009, and that there is a need of higher emission increase rate for 2010-2012 compared to those calculated by the inventory methods (Fig. 4.7-4b). The global mean CO_2 exchange simulated by TRENDY2 global dynamic vegetation models (DGVMs) are also shown, confirming no significant increase in carbon

uptake in East Asia due to CO_2 fertilization and climate (S2 simulation). The forest carbon storage rates based on the country statistics of Land use and land cover to the U.N. Food and Agriculture Organization - Forest Resource Assessment (FAO-FRA2015; country-level inventory estimates) also suggest no significant change in carbon sequestration in the East Asia region (symbols with bars; different colors are for different data sources; Calle et al., 2016).

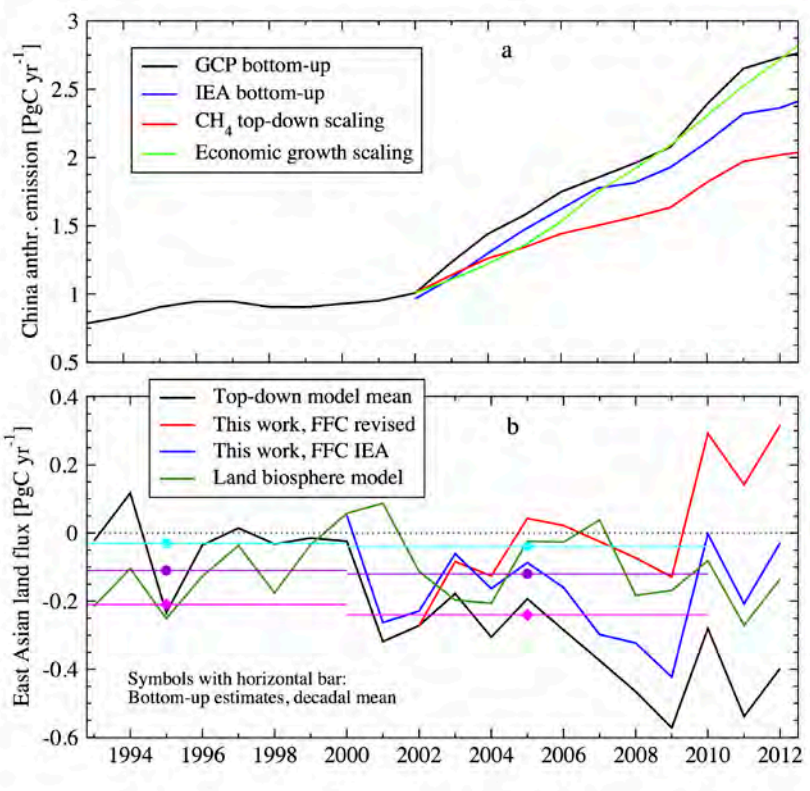

Figure 4.7-4. Effect of FFC CO_2 emission increase rate on regional carbon budget of East Asia. (a) Time series of anthropogenic CO_2 emission scenarios for China for 4 scenarios based on a scaling factor from CH_4 inversion results for East Asia, the economic (GDP) growth, and those estimated by GCP (CDIAC) and IEA emission inventories. (b) Effect of FFC CO_2 emission increase rate on regional carbon budget of East Asia. Decadal mean CO_2 fluxes estimated by independent bottom-up models (Calle et al., 2016) and TRENDY2 (land biosphere model) are also shown for a comparison.

4.7.4.2 A case study for global CO_2 balance

Further, the land CO_2 sink bias due to uncertainties in FFC CO_2 emission should influence our understanding of the global and regional carbon budgets. Figure 4.7-5 shows sectoral CO_2 sources/sinks budget obtained from the Global Carbon Project (GCP; Le Quéré et al. 2015). The corrected anthropogenic CO_2 emissions also produce measurable reductions in the rate of global land CO_2 sink increase post-2002, leading to a better agreement with the terrestrial biospheric model simulations by the TRENDY2 project (Sitch et al. 2015). This raises a question on the validity of proposed stabilization in FFC CO_2 emissions, and consequently a large increase the inferred terrestrial uptake during 2003-2012 (e.g., Le Quere et al., 2015).

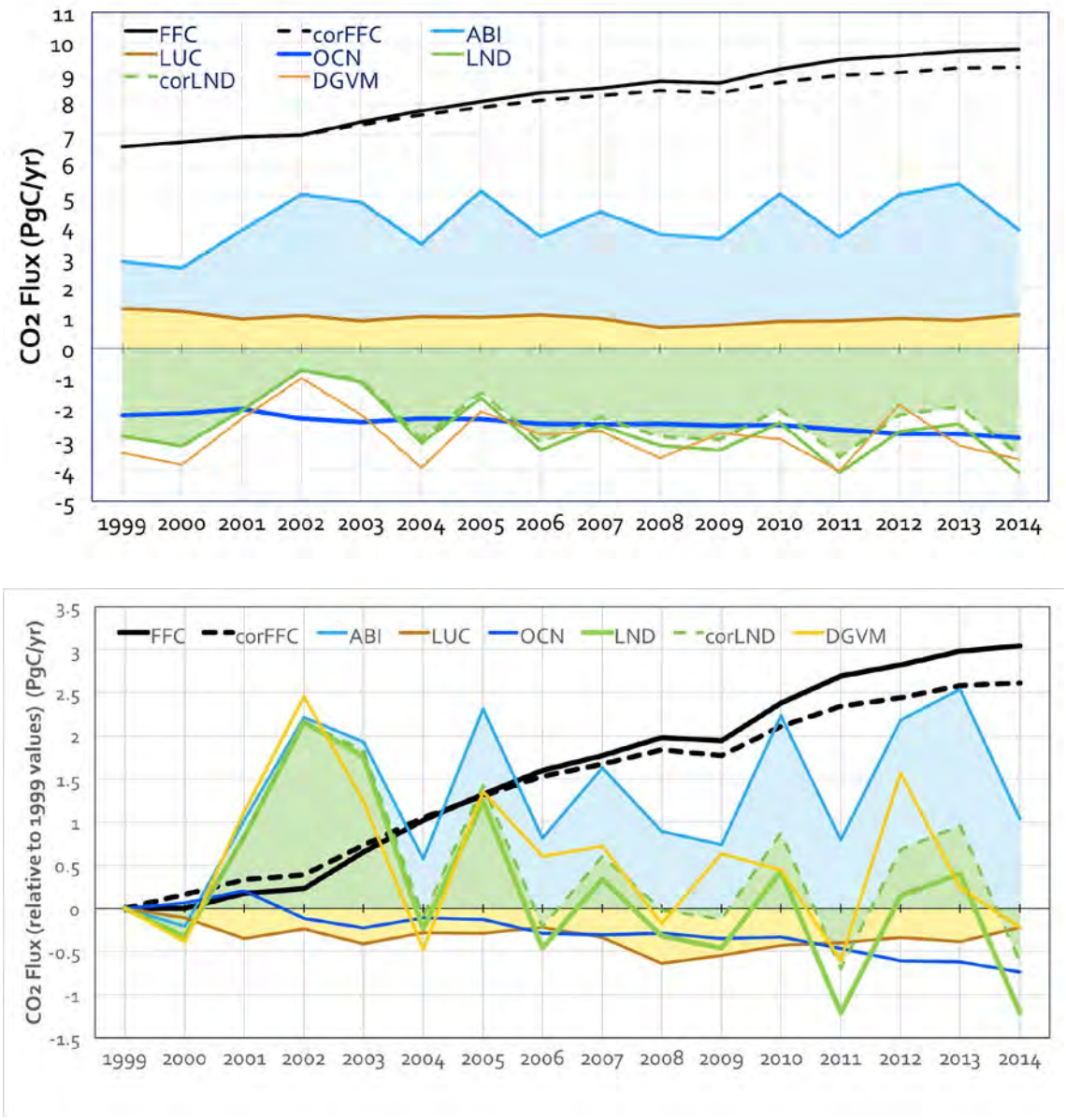

Figure 4.7-5. Time series of CO_2 fluxes as estimated by the Global Carbon Project for fossil fuel and cement (FFC), land-use change (LUC), atmospheric burden increase (ABI), oceanic exchange (OCN), residual land biosphere (LND = FFC + LUC – ABI − OCN), ensemble mean land fluxes simulated by the global dynamic vegetation models (DGVMs from TRENDY project) during the period 1999–2014 (top). FFC corrected by CH_4 inversion scaling (corFFC) are also shown. Corrected land fluxes (corLND) is based on residuals calculated using corFFC emissions. Relative values to the year 1999 are also shown in the lower panel for better clarity on the improved agreement of corLND fluxes with those simulated by the state-of-the-art DGVMs (bottom).

4.8 Inversion modeling of global CH_4 emissions: results for sub-continental regions of Asia and outlook for satellite data utilization

Prabir K. Patra[1], Tazu Saeki[2], Shuji Aoki[3], Shinji Morimoto[3], Takakiyo Nakazawa[3], Edward J. Dlugokencky[4], Andre Butz[5], and Ronald G. Prinn[6]

1) Japan Agency for Marine-Earth Science and Technology (JAMSTEC), Yokohama, Japan

2) National Institute for Environmental Studies (NIES), Tsukuba, Japan

3) Graduate School of Science, Tohoku University, Sendai, Japan

4) ESRL, National Oceanic and Atmospheric Administration (NOAA), Boulder, USA

5) Institute of Atmospheric Physics, German Aerospace Center (DLR), Munich, Germany

6) Massachusetts Institute of Technology, Cambridge, USA

4.8.1 Introduction

Methane (CH_4) is an important greenhouse gas, second only to carbon dioxide (CO_2) for the net increase in radiative forcing of the Earth's atmosphere since the preindustrial time (circa. 1750). The radiative forcing due to naturally occurring water vapour has not changed apparently in the era of direct measurement [IPCC, 2013]. Methane also participate strongly in the chemistry of tropospheric air pollution and in modulating stratospheric water vapour budget. Sources and sinks budgeting of CH_4 is thus seen as more challenging compare to CO_2, because the latter has the sources and sinks located on the Earth's surface and no chemical production/loss is considered in modelling atmospheric-CO_2 [Heimann and Keeling, 1989], while about 90% of CH_4 is lost by reacting with hydroxyl radical (OH) in troposphere. The third most important GHG, nitrous oxide (N_2O) is emitted from the Earth's surface and has no known loss processes within the troposphere [Ishijima et al., 2010]; thus no direct link between the photo-chemical loss of N_2O and surface emissions. In contrast to CO_2 and N_2O, for deriving atmospheric observational constraint on emission of CH_4 on the Earth's surface requires full knowledge of its chemical loss in the troposphere. Thus, the distribution and trends in OH should be independently verified for quantification of chemical sink of CH_4, particularly in the troposphere, before performing inverse modelling of atmospheric-CH_4 for estimating surface emissions [Patra et al., 2014].

Inverse modeling, the so called a top-down approach, is commonly employed for estimation of global and regional greenhouse gases (GHGs) emission by using an atmospheric chemistry-transport model (CTM) and measurements of GHG concentrations. The accuracy of CH_4 sources and sinks modelling depends on the uncertainties in representation of model transport, OH concentration and size of observational network. For a very long time, small number of in situ measurements from about 100 sites were the source of atmospheric data for inverse modelling of CH_4 emissions (Patra et al., 2016 and references therein). Only recently, dedicated satellites sensors are launched for GHGs measurements, e.g., the Greenhouse gases Observation SATellite (GOSAT)

by JAXA (Kuze et al., 2009). However, the both downward-looking satellites or upward-looking Fourier-Transform Spectrometers (FTS) measure the total columnar in the atmosphere, which significantly weakens the link between the variabilities in atmospheric measurements and surface emissions, compared to the is situ measurements. Thus, a much greater dependence on CTM simulation is envisaged for inferring surface sources from total column measurement.

4.8.2 Data and Method

4.8.2.1 Atmospheric chemistry-transport model (ACTM)

Methane in atmosphere is simulated using the Center for Climate System Research/National Institute for Environmental Studies/Frontier Research Center for Global Change (CCSR/NIES/FRCGC) atmospheric general circulation model (AGCM)-based CTM (i.e., JAMSTEC's ACTM; Patra et al., 2009). The following continuity equation is solved for time (t) evolution of CH_4 at different latitude (y), longitude (x) and altitude (z) in the earth's atmosphere.

$$\frac{dCH_4(x,y,z,t)}{dt} = S_{CH4}(x,y,t) - L_{CH4}(x,y,z,t) - \nabla \bullet \Phi_{CH4}(x,y,z,t) \qquad \text{(Eq. 1)}$$

where, CH_4 is methane mole fraction in the atmosphere, S is emissions/sinks of CH_4 at the surface, taken from bottom-up emission inventories and terrestrial ecosystem model simulations, L is temperature (T) dependent loss rates of CH_4 due to reaction with OH, $O(^1D)$ and Cl, and the last term: defines transport of CH_4 by advection, convection and diffusion. The loss and transport terms in Equation 1 should be critically evaluated before optimizing bottom-up emissions of CH_4. Details of the ACTM setup are given in Patra et al. (2016).

4.8.2.2 CH_4 observations

We use atmospheric CH_4 measurements in units of dry-air mole fraction (in ppb, parts per billion) from 37 NOAA/ESRL cooperative global air sampling network sites and 2 Japan Meteorological Agency sites for estimating monthly-mean emissions by inversion (**Fig. 4.8-1**). Both measurement networks reported data on the WMO mole fraction scale (Dlugokencky et al., 2005). These remote background measurement sites are chosen based on minimal data gap, typically less than 2 months, for the period of inverse calculation, 2001–2013.

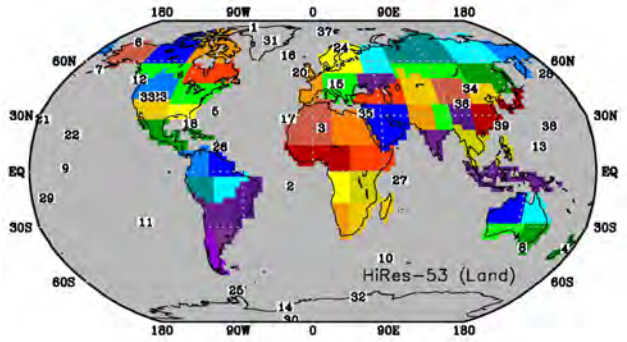

Fig. 4.8-1. Map of 53 land region divisions used in CH_4 inverse modelling by ACTM (Patra et al., 2016). Locations of 39 measurement sites are marked by numbers. Observational data are available from the WMO World Data Center for Greenhouse Gases (WDCGG).

For independent validation of the estimated CH_4 emissions by inverse modelling, we use the long-term aircraft profile measurements over Sendai (38.3°N, 140.9°E) by Tohoku University (Umezawa et al., 2014). These measurements are located strategically in the region of maximum emission increase due to anthropogenic activities as suggested by the inventory emissions.

We use the RemoTeC's CH_4 Full Physics GOSAT product, jointly developed at SRON Netherlands Institute for Space Research and the Karlsruhe Institute for Technology (KIT). The algorithm retrieves simultaneously CH_4 and CO_2, as well as three aerosol parameters representing their amount, height distribution and size distribution from four spectral regions: the 0.77 μm oxygen band, two CO_2 bands at 1.61 and 2.06 μm, as well as a CH_4 band at 1.64 μm. The XCO_2 and XCH_4 products have been extensively validated with ground-based measurements (Butz et al., 2011).

4.8.2.2 CH_4 inversion

The imbalance between a priori emissions and loss rates produces significant (much greater than observational data uncertainty) mismatches between the observed and simulated growth in CH_4 in the Earth's atmosphere (**Fig. 4.8-2**). Thus, inverse model calculations are often performed to correct for deficiencies in bottom-up emission estimates. In the Bayesian method, we estimated emissions (S) and their uncertainties (C_S) using the following equations:

$$C_S = (G^T C_D^{-1} G + C_{S_0}^{-1})^{-1}$$

$$S = S_0 + \left(G^T C_D^{-1} G + C_{S_0}^{-1}\right)^{-1} G^T C_D^{-1} (D - D_{ACTM})$$

(Eq. 2 and Eq. 3)

where, S_0 is regional prior sources, C_{S0} = Prior source covariance (square of uncertainty), set at 70% of region-total emission for each month (S_0), D is atmospheric observations, C_D is data covariance and is set to variable depending on the site behaviour, D_{ACTM} is ACTM simulation using a priori emissions (S_0), and G is Green's functions, defining the regional source-receptor relationships. The sources are calculated for 53 basis land regions as depicted in **Fig. 4.8-1**. The CH_4 emissions from the ocean regions are not optimized due to its small contribution (~10 Tg yr^{-1}) to the global total emission.

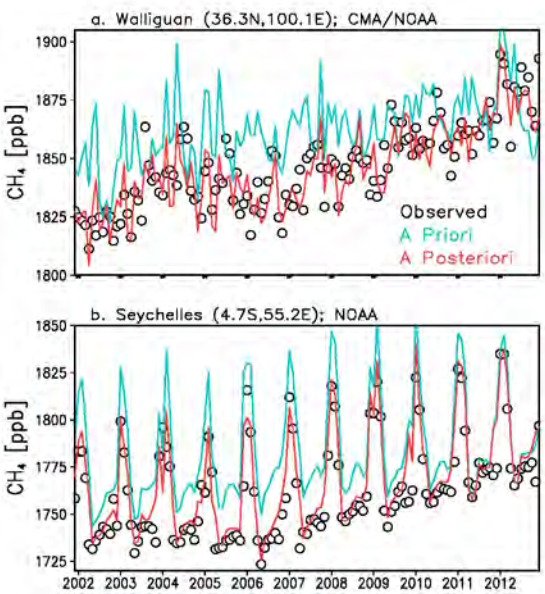

Fig. 4.8-2. Time series of CH_4 mole fractions as observed at selected two of the 39 measurement sites used in the emission inversion. ACTM simulated values are also shown for a priori and a posteriori CH_4 emissions from inverse model.

4.8.3 Results and discussions

4.8.3.1 CH_4 inversion results and validation using independent aircraft data

We combined emissions from natural and anthropogenic activities, and subtracted the surface sinks due to bacterial consumption in the soil to prepare an ensemble of 7 cases of a priori emissions (**Fig. 4.8-3**a,b; grey lines). The a priori emission case (CH_4e42) with highest emission and rapid increase rate corresponds to anthropogenic emissions from EDGAR42FT (2013) and the most of the increase can be attributed to the East Asia region (mainly China). Different assumptions of sectorial anthropogenic and natural emissions are made while preparing the total CH_4 emissions for the 7 a priori cases (details in Patra et al., 2016). Figure **4.8-3a** (coloured lines) shows that 6 of the 7 inversion ensembles agreed very well for the global totals and interannual variations (r^2=0.81 for CH_4ags and CH_4e42, r^2>0.97 between CH_4ags and 6 others). The inversions show significant increases in the global CH_4 flux starting in 2007 by greater than 20 Tg yr^{-1} compared to ~12 Tg yr^{-1} of 1-σ standard deviation for IAV. The CH_4ctl case generated interannual variation that does not exist in the prior (grey straight line). Although the CH_4e42 case followed very similar emission trajectories as the 6 other cases, it remained separated for the both global and East Asian total emissions.

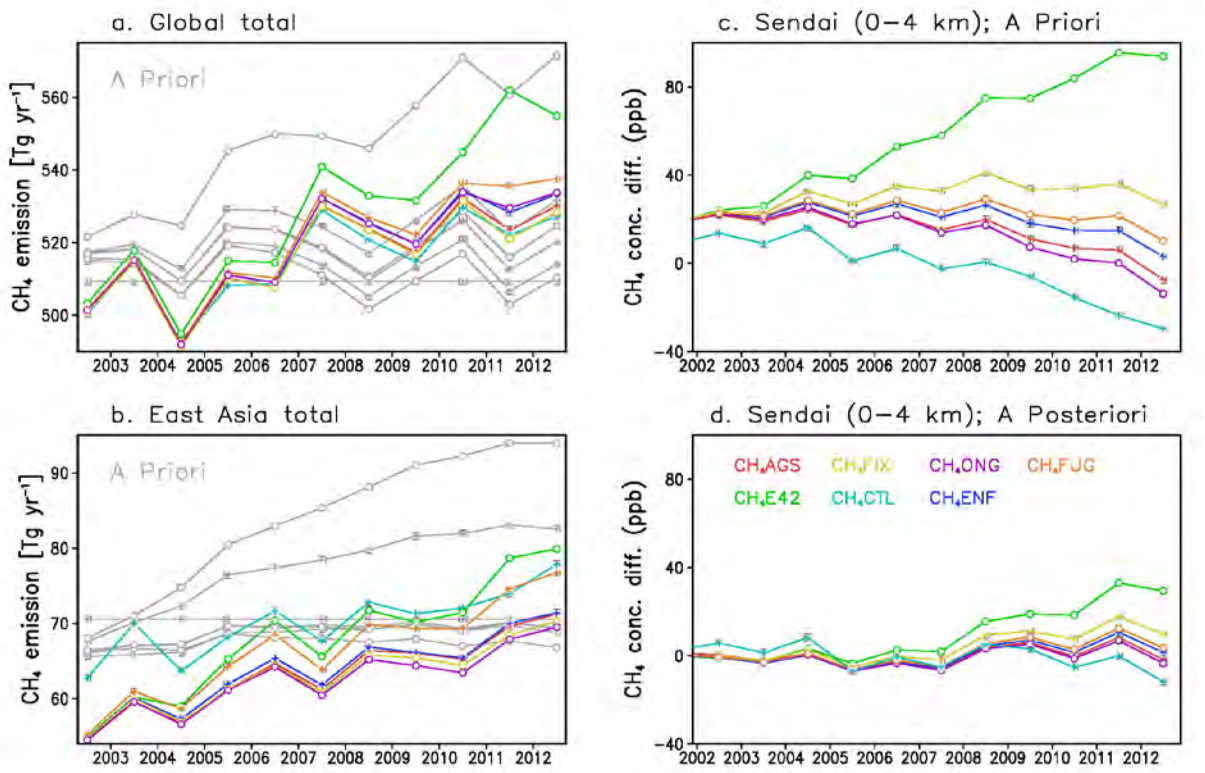

Fig. 4.8-3. Time evolution of total CH_4 emissions of all source types for global and East Asia (a,b). The a priori emissions of 7 ensemble members are shown as the grey lines, and those following the inversion are shown in coloured lines. The ACTM simulations corresponding to the a priori and a posteriori emissions are depicted in panels c and d, relative to the observed CH_4 concentrations over Sendai in the lower troposphere. All coloured line legends are common to those given in panel d.

For validating the CH_4 emission increase rate, we show model – measurement differences of CH_4 over Sendai, Japan in **Fig. 4.8-3c,d**. The simulated mole fractions calculated with a posteriori emissions agree with the measured values within 0.3% (5 ppb) for individual years, except for CH_4e42 case. The vertical gradients are also well simulated for 2002–2012 (not shown) with typical model-observation differences lower than 20 ppb. These comparisons clearly indicate that the CH_4e42 inversion case still overestimates emissions of CH_4 from the East Asia region. Our best estimated emission increase is 7–8 Tg yr^{-1} over the periods of 2002–2006 and 2008–2012, by excluding the CH_4e42 case. It should be pointed out here that a posteriori uncertainty (C_S) was about 22 Tg yr^{-1} for the East Asia region, which does not truly reflect the quality of mean a posteriori flux by the 6 inversion ensembles. The quality of the mean fluxes is better evaluated (within 10 Tg yr^{-1}) using independent aircraft measurements. The net increase in CH_4 emissions by inversion for East Asia has large implications for CO_2 inversions (Saeki and Patra, 2017).

4.8.3.2 Linking inter-hemispheric CH_4 balance with north-south hemispheric OH gradient

As mentioned earlier, most of CH_4 in atmosphere are lost due to reaction with OH. Because of its very short lifetime (~1 sec) and very low abundance (~10^6 molecules cm^{-3}) in the troposphere, an accurate characterization of OH distributions and strength has remained elusive. Use of methyl chloroform (CH_3CCl_3) is found to be ideal for characterizing OH, because emission of this man-made species is regulated stringently by the Montreal Protocol in 1988 due its strong ozone depletion potential, and the local lifetimes of CH_3CCl_3 is 1–3 years in the tropical troposphere, which is of similar magnitude as the interhemispheric transport time of ~1.3 years. The latter condition is important for evaluating northern-to-southern (NH/SH) ratio of hemispheric mean OH. Using the time evolution of CH_3CCl_3 simulation, the balance between global total emissions and global mean OH concentrations can be established (**Fig. 4.8-4a**). We use pre-defined tropospheric OH concentrations from Spivakovsky et al. (2000) (referred to as ACTM_0.99 as the NH/SH OH ratio is 0.99) and Sudo et al. (2002) (referred to as ACTM_1.26 as the NH/SH OH ratio is 1.26). From the observed differences in CH_3CCl_3 between MHD and CGO from two ACTM simulations (**Fig. 4.8-4b**), equal amount OH in both the hemispheres is suggested (Patra et al., 2014).

One of the important implications of correctly estimating the NH/SH OH ratio is for the budgets of many important short-lived species that affect the Earth's radiative budget and air pollution chemistry. Impact of using ACTM_0.99 and ACTM_1.26 OH fields on CH_4 emission estimation is studied using our newly developed inverse modeling system [*Patra et al.*, 2016]. The inverse estimated CH_4 emissions are clearly biased high in the NH mid-high latitude regions and generally biased low (compensatory for global totals) in the tropical and SH land regions when ACTM_1.26 is used in forward modelling of CH_4, compared to the use of more accurate representation of OH in ACTM_0.99 (**Fig. 4.8-5**). The NH total CH_4 emission estimated to be 18 Tg

yr^{-1} higher for ACTM_1.26 (and 15 Tg yr^{-1} lower in the SH), compared that for ACTM_0.99.

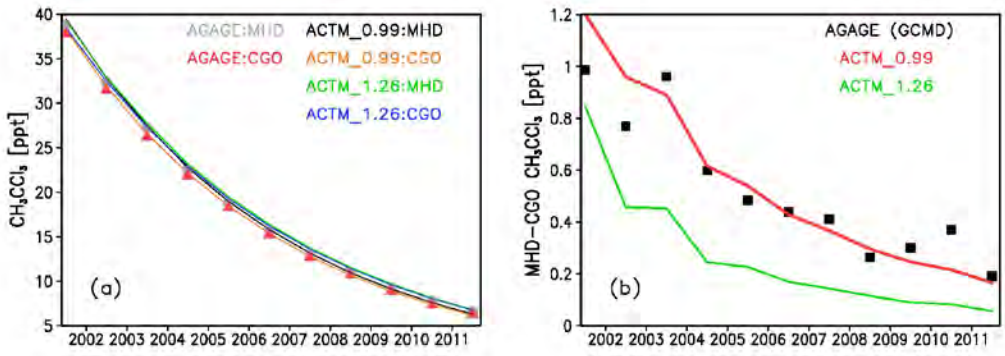

Fig. 4.8-4. Time series of CH_3CCl_3 concentrations (a) and inter-sites gradients (b) as observed by AGAGE network (Prinn et al., 2000) at Mace Head (MHD) and Cape Grim (CGO) and simulated by ACTM_0.99 and ACTM_1.26 simulations.

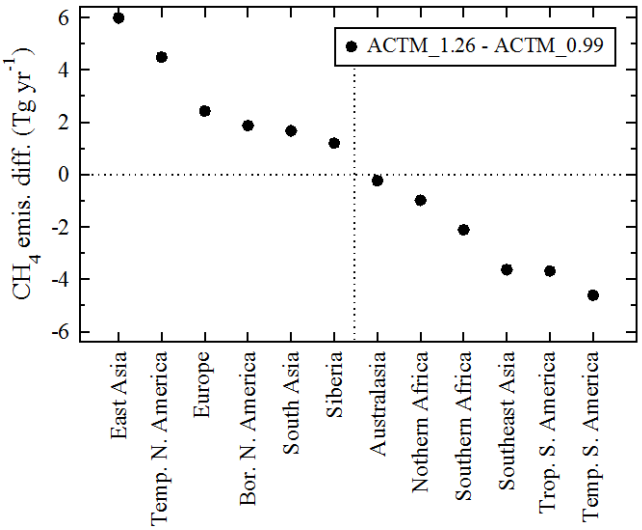

Fig. 4.8-5. Differences in inversion estimated CH_4 emissions due to the use of two different OH distributions in ACTM simulations. The 12 regions identified as the x-tick labels are obtained by aggregating 53 regions of the inverse model as depicted in **Fig. 4.8-1**.

4.8.4 Outlook for GOSAT CH_4 utility

One of the major limitations for inverse modelling of GHG sources/sinks is the lack of sufficient in situ measurement stations, say covering each of the 53-regions of the inverse model (**Fig. 4.8-1**). However, this limitation should be relaxed provided high density and high-quality measurements of CH_4 are made from space. Although progress is being made in understanding the information content in GOSAT XCH_4 retrievals over the Asian regions (Ishizawa et al., 2016; Chandra et al., 2017), various retrieval biases and uncertainties in forward model simulations still keep the GOSAT data usage at minimal for CH_4 inverse modelling (e.g., Pandey et al., 2016).

An overall agreement is found between the maps of CH_4 emissions and GOSAT XCH_4 distributions for the high emissions and CH_4 over the Indo-Gangetic Plain (IGP) and most parts of eastern China (**Figure 4.8-6a,b,d**). The east-west gradients in CH_4 over IGP by model simulations show different feature when simulated by ACTM_0.99, where simulation using CH_4ags emission case show much higher XCH_4 over Bangladesh compared to the ACTM simulation using CH_4ctl

case and the retrievals by SRON/KIT. The XCH_4 seasonality using CH_4ags emission also peaks earlier compared to the observations due to early peak in emissions (**Figure 4.8-6c,g,h**). This suggests the GOSAT XCH_4 values contains information for constraining regional CH_4 emission over the South Asia region. It may be noted here that the data density over the South Asia region is sparse during the summer monsoon season (June-Sept.) due to dense cloud cover. Further analysis is needed for understanding the causes for large differences found between the GOSAT XCH_4 and both the ACTM simulations over the northern Southeast Asia and southern China. These regions are largely unconstrained by the in situ measurement sites used the inversion.

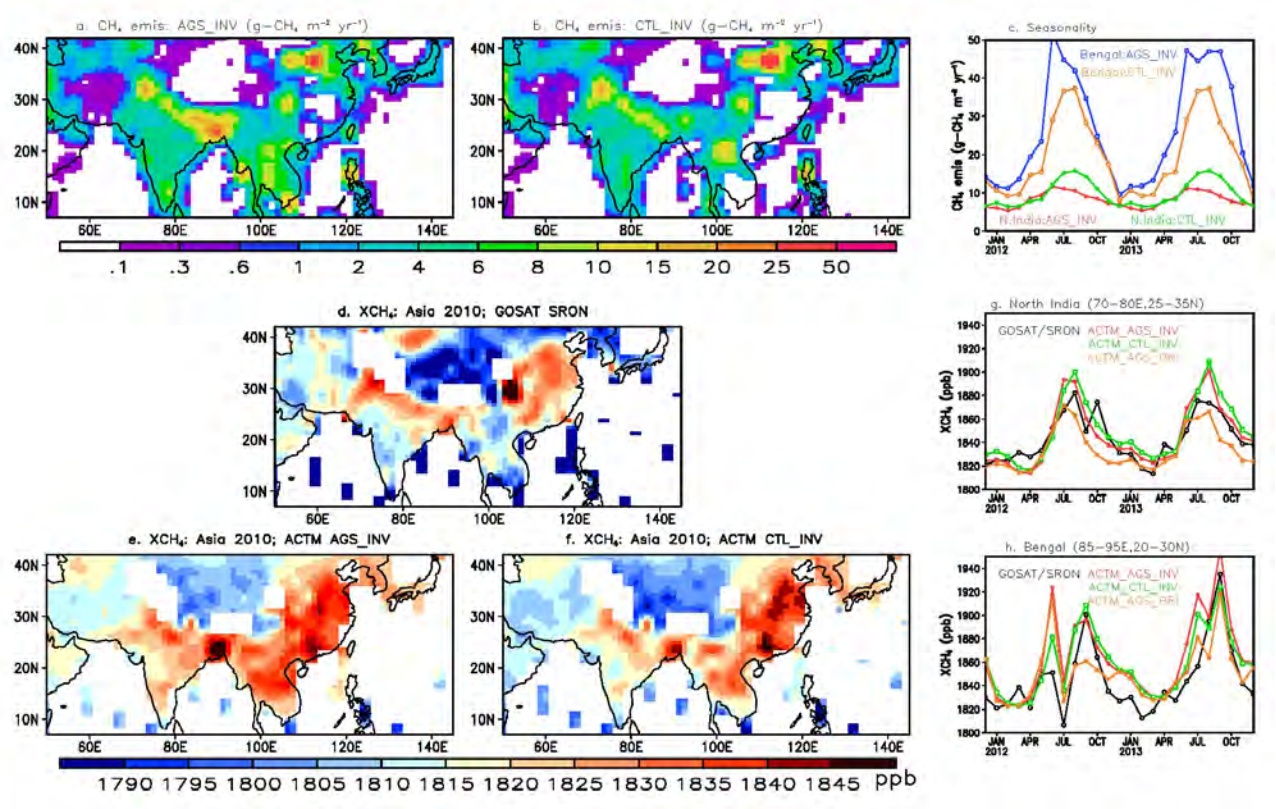

Fig. 4.8-6. Maps of CH_4 emissions (a,b) and total column XCH_4 concentrations (d,e,f) are compared. Time series of CH_4 fluxes and XCH_4 time series are shown for seasonal cycle comparisons (c,g,h). The simulations are conducted by ACTM_0.99 version of the model.

4.9 Quantifying CO_2 Emissions from Individual Power Plants from Space

Ray Nassar[1], Timothy G. Hill[2], Chris A. McLinden[1], Debra Wunch[3], Dylan B.A. Jones[3], and David Crisp[4]

1) Environment and Climate Change Canada, Toronto, ON, Canada

2) University of Waterloo, Waterloo, ON, Canada

3) University of Toronto, Toronto, ON, Canada

4) Jet Propulsion Laboratory, California Institute of Technology, Pasadena, CA, USA

4.9.1 Introduction

Although the Orbiting Carbon Observatory 2 (OCO-2) was not designed for quantifying emissions at the scale of an individual power plant, its limited potential to do so was foreseen in "Verifying Greenhouse Gas Emissions: Methods to Support International Climate Agreements" [*Pacala et al.*, 2010]. In selected clear-sky cases, where direct OCO-2 overpasses or close flybys of individual mid- and large-sized coal power plants occur, OCO-2's narrow swath can image a segment of the CO_2 emission plume, enabling quantification of the emissions with a method adapted from studies for CarbonSat [*Bovensmann et al.*, 2010]. This is first demonstrated by quantifying daily CO_2 emissions from US power plants by fitting the observed XCO_2 enhancements from OCO-2 to enhancements simulated by a Gaussian plume model, along with a system for estimating uncertainties. These daily emission estimates and uncertainties are compared with publicly-available CO_2 emission data from the US Environmental Protection Agency (EPA). Next, the approach is used to derive emissions from a large coal power plant in India that has less detailed publicly available emission data and higher uncertainties. Although more complex modeling or data analysis could improve emission estimates, *Nassar et al.* [2017] demonstrates for the first time, the ability to quantify emissions from individual power plants with CO_2 satellite data. The potential of some upcoming and proposed CO_2 satellites to provide improved capabilities is also discussed. Overall, the *Nassar et al.* [2017] results affirm that a future constellation of CO_2 imaging satellites, optimized for point sources, could contribute to the monitoring, reporting and verification (MRV) of CO_2 emissions from individual power plants to support the transparency framework of climate agreements and the implementation of emission reduction policies.

4.9.2 Data

4.9.2.1 GHG Concentration Data and Other Data

A list of coordinates for mid- to large-sized coal power plants (emitting > 10 $MtCO_2$/yr) is generated from EPA data (https://ghgdata.epa.gov/ghgp/main.do#/listFacility/) for the US and from the Carbon Monitoring for Action (CARMA) (www.carma.org) [*Wheeler & Ummel*, 2008; *Ummel*, 2012] and the Global Energy Observatory (GEO) databases (www.globalenergyobservatory.org)

elsewhere. CARMA has global power plant CO_2 emission data for 2004, 2009 and 'Future', but its power plant locations can be unreliable, while the GEO database has more accurate location information (verified by inspection of sites in Google Earth) but little to no CO_2 emission data. We search OCO-2 L2 version 7r XCO_2 standard files from Sep 2014 – Dec 2016 inclusive for overpasses near sites of interest from the databases identified above. Aqua MODIS imagery of clouds, smoke, and surface properties can be viewed together with OCO-2 data since the Aqua satellite follows OCO-2 by 6 minutes in the A-Train. For each date and time of an OCO-2 overpass of a power plant found, ERA-Interim (~0.75°, 60 vertical levels) [*Dee et al.*, 2011] and MERRA2 (0.5°x0.625°, 72 levels) [*Molod et al.*, 2015] meteorological reanalysis files are acquired.

4.9.3 Method

4.9.3.1 Meteorology and Data Visualization

CO_2 transport from a power plant depends on the horizontal wind speed at the plume height. A power plant can have multiple stacks, so we calculate the emission-weighted mean stack height from available information or assume 250 m. We read the *u* and *v* winds for the levels above and below the mean stack height from the two meteorological data sets and vertically linearly interpolate to the mean stack height. ERA-Interim winds are reported as instantaneous values at 6-hour intervals, so we also linearly interpolate between the two nearest temporal points. For MERRA2, which is provided as 3-hour average winds, we use the closest time directly. The interpolated *u* and *v* wind vectors are converted to a scalar wind speed and direction/bearing (0-360°) with 0° defined as due North. KML files are generated to visualize the parallelogram-shaped OCO-2 soundings in Google Earth with a customized XCO_2 color scale and wind vector arrows centered on each source. The XCO_2 value mapped with the KML file and used in the emission estimate is a bias corrected value, but uncorrected XCO_2 and two variations on the bias correction are also included in the file. We view the KML files to look for overpasses or flybys with an enhancement in the approximate wind direction. We reject overpasses where the wind blows away from the swath, those in regions with complex terrain, or where the swath is broken up due to cloud or aerosol, since neighbouring observations could be biased, but if nadir observations are lost over a small body of water, we retain confidence in the remaining observations. KML files for these case studies are available at ftp://ccrp.tor.ec.gc.ca/pub/RNassar/GRL_Power_Plants/.

4.9.3.2 Plume Model and Fitting

For each good overpass or flyby, we take the magnitude of the vector mean of the ERA-Interim and MERRA2 winds as the wind speed to model the plume. The plume model equations used are slightly modified from those in *Bovensmann et al.* [2010]:

$$V(x,y) = \frac{F}{\sqrt{2\pi}\sigma_y(x)u} e^{-\frac{1}{2}\left(\frac{y}{\sigma_y(x)}\right)^2} \quad \text{and} \quad \sigma_y(x) = a \cdot \left(\frac{x}{x_o}\right)^{0.894} \quad \text{[Eq. 1 and 2]}$$

where V is the CO_2 vertical column in (g/m^2) at and downwind of the point source. The x-direction is parallel to the wind direction and the y-direction perpendicular to the wind direction. V depends on the emission rate F (in g/s), the across wind distance y (in m), wind speed u (in m/s), and the standard deviation in the y-direction, σ_y (in m). Here x is specified in m and x_o=1000 m is a characteristic length so that the argument of the exponent is dimensionless. a is the atmospheric stability parameter, which we determine by classifying a source environment by the Pasquill-Gifford stability, which depends on the surface wind speed, cloud cover and time of day [*Pasquill*, 1961]. The surface wind speed and cloud cover are taken from ERA-Interim.

We select a region of the OCO-2 swath (preferably upwind and thus not affected by the source) as the background and average the XCO_2 from these points. The model plume is then defined as the area from the x-axis (wind vector) down to a threshold of 1% intensity in the positive/negative y-directions. We then define the observed plume based on the points that correspond to the model plume, accounting for the light path. We determine where the incoming and reflected solar radiation would intersect the plume, assuming a 2-dimensional plume at the mean stack height and ignoring plume rise. Once the observed plume is defined as the points geometrically corresponding to a 1% cut-off of the model plume, the background XCO_2 average in ppm is subtracted from it to get the observed XCO_2 enhancement in ppm. To convert the model enhancements from g/m^2 to ppm, we use the mean conversion factor k, which we calculate from the background values in g/m^2 and ppm given in the data files, where $k = V_{CO2} / XCO_2$. This is reliable only if there are no large or abrupt changes in topography for the background. If the wind is nearly parallel to the swath, we truncate the plume at some distance from the source to avoid very small relative enhancements and plume modeling over long space/time scales.

With the observed and model plume defined as XCO_2 enhancements in ppm, we then calculate the model versus observation correlation coefficient (R). This process is repeated testing adjustments to the wind direction to maximize the correlation. We accept a rotation to the wind if it improves R, passes visual inspection and is consistent with the level of disagreement between the ERA-Interim and MERRA2 winds. Fitting for the wind direction reduces the impact of errors in the wind direction from the meteorological fields. Using the optimized wind direction, we determine the a posteriori emissions by carrying out a weighted linear least squares fit between the model and observed enhancements calculated per unit emissions. The weights in the least squares fit are the reciprocal of the XCO_2 uncertainty values from the OCO-2 full files. We estimate emissions as $ktCO_2$/day (1 kt = 10^6 kg).

4.9.3.2 Emission Uncertainties

Bovensmann et al. [2010] state that since the emission estimate is linearly-dependent on wind speed, an error in the wind speed contributes linearly to an error in the emission estimate (i.e. a 10% error in the wind speed contributes a 10% error to the emission estimate). In actuality, the error dependence is slightly more than linear because the wind speed indirectly affects σ_y via a. We calculate the wind uncertainty contribution (ε_w) to the emission estimate as the percent difference of the two different wind fields from the mean and convert this to an emission rate uncertainty in $ktCO_2$/day. The background CO_2 concentration is a source of uncertainty in this work and in any work where an enhancement is defined with respect to the background, whether determining the emissions from a power plant, megacity or volcano. We define the background in 4 different yet plausible ways, calculating the spread in emission estimates from this small ensemble to get a standard deviation (ε_b) in $ktCO_2$/day. If the ensemble gives a large spread, then ε_b is large and results in a large overall uncertainty for the emission estimate. If ε_b is too large, a good background cannot be established and we reject the overpass for quantifying emissions.

The emission uncertainty due to uncertainties in the OCO-2 observations (ε_e) is also considered using an ensemble. The enhancement relative to the background is calculated multiple times with an ensemble of 4 bias correction approaches, as described in the supporting information. Our ensemble approach effectively quantifies the sensitivity of the multi-step emission estimate to biases of the sizes and patterns that could result by applying the different bias corrections, which provides a good estimate of the potential uncertainty in the emission estimate arising from the OCO-2 data. Another source of uncertainty is that due to secondary sources (ε_s), but as it is only non-zero for one example, it is explained later. The total error is then determined from the wind, background, enhancement and secondary source terms: $\varepsilon = \sqrt{{\varepsilon_w}^2 + {\varepsilon_b}^2 + {\varepsilon_e}^2 + {\varepsilon_s}^2}$ [Eq. 3]. Uncertainty related to neglecting plume rise due to thermal lifting in determining the altitude selected for the wind speed is difficult to quantify and has not been included above, but is discussed in *Nassar et al.* [2017] supporting information.

4.9.4 Case Studies

4.9.4.1 A Direct Overpass of a Power Plant in the U.S.

For a direct OCO-2 nadir overpass with the wind nearly aligned with the orbit track, both the base and center of the plume are imaged, and the background is the portion of the swath upwind from the source. This alignment is very rare for OCO-2 due to its narrow swath. One occurrence was a flyover on 2015-12-04 of the Westar Jeffrey Energy Center (Fig. 4.9.1), a mid-sized sub-bituminous coal-fired power plant in Kansas with three 175-m tall stacks and annual 2015 emissions of 12.5 $MtCO_2$. The observed enhancement is small (~1 ppm) since the emissions were dispersed quickly by strong winds (~11 m/s). The EPA provides hourly to annual CO_2 emissions for

individual facilities (https://ampd.epa.gov/ampd/) and on this date, reported 26.7 ktCO_2/day. A model fit to the observations gave a daily estimate of 31.2±3.7 kt, with uncertainty contributions due to wind speed (0.85 kt), the background definition (1.8 kt) and the enhancement (3.1 kt).

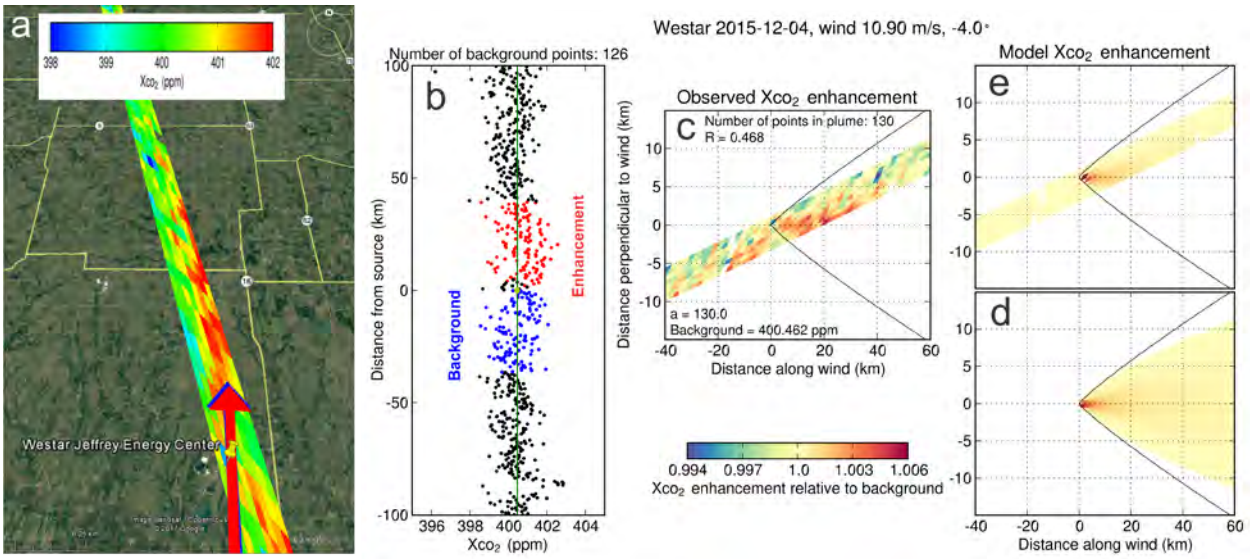

Figure 4.9-1. Direct OCO-2 overpass in the U.S. (a) XCO_2 from OCO-2 near the Westar Jeffrey Energy Center shown in Google Earth with ERA-Interim (red) and MERRA2 (blue) wind vectors. (b) Plume points (red), background points (blue), and the background mean (green line). (c) Observed XCO_2 relative to the background. (*R* is the correlation coefficient and *a* is the atmospheric stability parameter). (d) Gaussian plume model XCO_2 plume relative to the background. (e) Gaussian plume model XCO_2 relative to the background as would be viewed by OCO-2. Solid lines in panels c–e show the model 1% plume density cutoff from the axial value.

4.9.4.2 A Close Flyby of a Power Plant in the U.S.

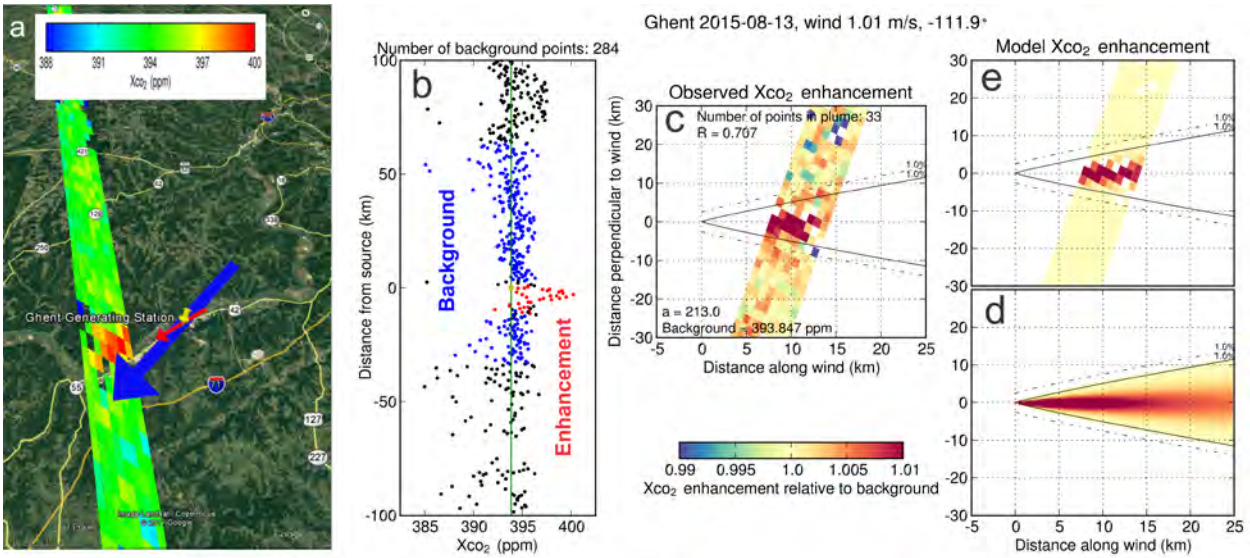

Figure 4.9-2. Same as Figure 1 for a flyby of the Ghent Generating Station. The dotted lines in panels c–e show an offset for defining the background with respect to the plume edges.

In a close flyby, OCO-2's swath does not pass directly over the source. An example is a flyby ~8 km from the Ghent Generating Station (Fig. 4.9.2), a coal-fired generating station in Kentucky that emitted 11.0 $MtCO_2$ in 2015. OCO-2 observes a strong enhancement on 2015-08-13 since the wind speed is very low, yet uncertain (0.50 m/s ERA-Interim, 1.54 m/s MERRA2). Reported CO_2 emissions on this date were 29.2 kt and we estimate 29.5±15.6 kt. Uncertainties in wind speed contribute the majority (15.0 kt) of the large emission uncertainty in this result.

4.9.4.3 Application of the Method to a Large Power Plant in India

Our best example of quantifying emissions from a power plant using OCO-2 comes from a flyover of the Singrauli region of India (Fig. 4.9.3) with multiple large coal plants in close proximity. Our initial aim was to quantify emissions from the Vindhyachal and Singrauli power plants, which emitted 32.4 and 14.8 $MtCO_2$/yr respectively (CARMA future values). However, due to the spatial gradients and the strength of the XCO_2 enhancement (~10 ppm) in a 2014-10-23 flyby of these power plants, we found another major source directly below the enhancement using Google Earth. The new source detected was the Sasan Ultra Mega Power Plant (UMPP), which was commissioned between 2013 and 2015. Sasan only appears in CARMA as a future emitter with an estimate of 33.7 $MtCO_2$/yr, but this estimate assumes a very high emission intensity (1.26 tCO_2/MWh).

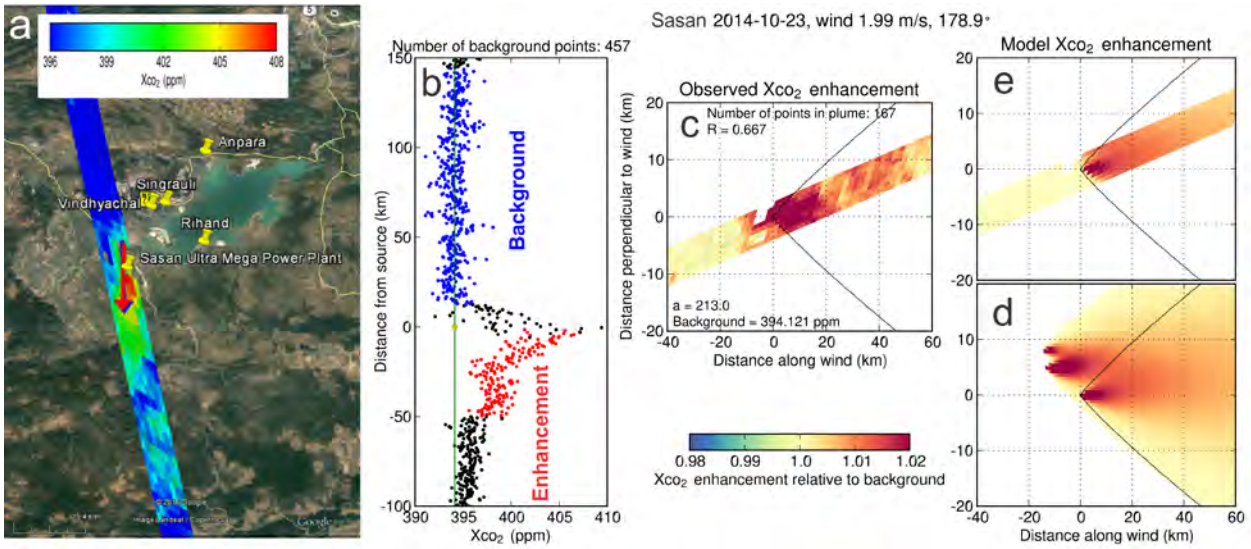

Figure 4.9-3. Same as Figure 1 for a direct overpass of a large power plant in India with multiple other power plants nearby. Model simulations here include the primary source (Sasan) plume and two secondary source (Vindhyachal and Singrauli) plumes superimposed.

Sasan's Clean Development Mechanism (CDM) application to the UNFCCC (Greenhouse Gas Reductions Through Super-Critical Technology - Sasan Power Ltd. Clean Development Mechanism

Project Design Document Form (CDM-PDD), version 3, 2006-07-28) states that at full capacity it was expected to emit 26.38 $MtCO_2$/yr. It has since received credits for certified emission reductions since its supercritical coal technology is claimed to emit ~9% less CO_2 than standard coal combustion. Vindhyachal and Singrauli are 14 and 16 km northeast and upwind of Sasan respectively, so we account for their emissions in the OCO-2 swath (Fig 4.9.3d, e), but two other large coal power plants, Rihand (20.3 $MtCO_2$/yr) and Anpara (16.8 $MtCO_2$/yr), are farther away and due to the wind direction, we consider their impact to be negligible. Only 5 of 6 units at Sasan were commissioned at the time of the flyover, so we assume 5/6 of the total output or a mean daily emission rate of 60.2 kt. The OCO-2 data yield an estimate of 67.9±10.0 kt with uncertainty contributions from wind (5.2 kt), the background (0.59 kt), the enhancement (3.2 kt) and an additional error term for the presence of secondary sources (5.6 kt), determined by perturbing the CARMA values by ±20%, which gave a perturbation to the estimated emissions of ±5.6 $ktCO_2$/day (ε_s in equation 3). We also tested the sensitivity of the result to the along-wind length of plume used ranging from 20-50 km, but it had a smaller impact than any of the error terms included. With this large XCO_2 enhancement, a well-defined background and good consistency in winds, our uncertainty is 14.7% of the estimated emission value, but would be only 9.1% if not for the secondary sources.

4.9.4.4 Discussion and Conclusions from Case Studies

Gaussian plume models are attractive for their simplicity, but like all models, have limitations, so we applied the model only to flat regions and to moderate distances and times (up to ~50 km, ~3 h) since our implementation assumes constant emissions and wind speed and direction, assumptions that degrade over longer distances and times. Table 1 in *Nassar et al.* [2017] shows emission estimates for 3 US power plants, 1 in India and 1 in South Africa, including the case studies above. US emission estimates are within 1%, 4% and 17% of the EPA daily values. Internationally, only annual values (from another year) are available, so we calculated mean daily values. Typically, uncertainties related to wind speed were the largest contributor to total uncertainty, which could potentially be reduced with higher space-time resolution wind fields. The background CO_2 concentration was another source of uncertainty, which we dealt with by avoiding overpasses with ambiguous backgrounds or using an ensemble of background definitions. OCO-2 bias and precision both contribute to the enhancement uncertainty term, which was usually lower than the uncertainty due to wind. The low uncertainty contribution from the observations means that the accuracy and precision of OCO-2 are adequate for quantifying emissions from large and mid-sized coal power plants and its real limitation is coverage. OCO-2 is a global sampling mission with a narrow swath, not a mapping mission, so there are wide gaps between successive orbit tracks. Since so much of the Earth is covered by clouds at any given moment and XCO_2 retrievals are very sensitive to cloud

contamination, ~90% of XCO_2 observations from OCO-2 and other CO_2 missions are rejected, with some variation based on observing geometry, field-of-view size and cloud detection methods. As a result, in ~2 years of OCO-2 data there is rarely more than 1-2 overpasses that are sufficiently uninterrupted by cloud and have an appropriate wind direction for any given power plant.

To quantify CO_2 emissions from individual power plants from space, precise CO_2 imaging with good spatial resolution and coverage is essential. China's TanSat adds to the coverage currently obtained from OCO-2 and the upcoming OCO-3 will have an emphasis on targeting cities and power plants, but these LEO imaging missions will still only enable point source quantification in select cases. Wider-swath LEO missions would be a benefit; however, estimating annual emissions, arguably the most policy-relevant time scale for MRV, requires multiple clear-sky revisits in a given year, which is likely not possible to obtain from a single LEO mission. The number of revisits required (considering seasonal and diurnal variations) must be established in future work, but with enough overpasses, annual emission estimates should have lower relative uncertainties than single-overpass daily values. The Sentinel-7 candidate constellation of 3-4 CO_2 monitoring LEO satellites could potentially provide the required sampling frequency. Imaging from geostationary orbit (GEO) like NASA's future GeoCarb mission or other GEO concepts is another approach that would offer diurnal sampling over land with the flexibility for very frequent observations by targeting priority locations or cloud-free areas. GEO satellites positioned to observe the Americas, Europe/Africa and East Asia could provide a system for monitoring low to mid latitude sources, while highly elliptical orbit (HEO) satellites [*Nassar et al.*, 2014] could view higher latitudes.

Nassar et al. [2017] presents the first detection and quantification of CO_2 emissions from individual facilities using space-based observations, and has yielded daily emission estimates for coal power plants with reasonable accuracy and precision. The results were obtained with observations from OCO-2, a mission not designed for this purpose, and suggest that a constellation of multiple CO_2 imaging satellites optimized for point sources could provide data for regular policy-relevant CO_2 emission quantification for mid- and large-sized fossil fuel burning power plants across the world.

APPENDIX-1 REFERENCES

Aggarwal, C. C. (2015), Data Mining: The Textbook, Springer, New York.

Alexe, M., et al. (2015), Inverse modelling of CH_4 emissions for 2010–2011 using different satellite retrieval products from GOSAT and SCIAMACHY, Atmospheric Chemistry and Physics, 15, 113–133, doi:10.5194/acp-15-113-2015.

Bergamaschi, P., et al. (2009), Inverse modeling of global and regional CH_4 emissions using SCIAMACHY satellite retrievals, J. Geophys. Res., 114, D22301, doi:10.1029/2009JD01228.

Bergamaschi, P., et al. (2013), Atmospheric CH_4 in the first decade of the 21st century: Inverse modeling analysis using SCIAMACHY satellite retrievals and NOAA surface measurements, Journal of Geophysical Research: Atmospheres, 118, 7350–7369, doi:10.1002/jgrd.50480.

Bergamaschi, P., et al. (2018), Inverse modelling of European CH_4 emissions during 2006-2012 using different inverse models and reassessed atmospheric observations, Atmos. Chem. Phys., 18, 901-920, doi: 10.5194/acp-18-901-2018.

Beusse, R., et al. (2014), Improvements needed in EPA efforts to address methane emissions from natural gas distribution pipelines, 14-P-0324, US EPA Office of Inspector General, available at: https://www.epa.gov/sites/production/files/2015-09/documents/20140725-14-p-0324_0.pdf (last access: 28 Sep 2017).

Bishop, C. M. (2007), Pattern Recognition and Machine Learning, Springer, 1 edn.

Bocquet, M. (2009), Toward Optimal Choices of Control Space Representation for Geophysical Data Assimilation, Monthly Weather Review, 137, 2331–2348, doi:10.1175/2009mwr2789.1.

Bocquet, M., et al. (2011), Bayesian design of control space for optimal assimilation of observations. Part I: Consistent multiscale formalism, Quarterly Journal of the Royal Meteorological Society, 137, 1340–1356, doi:10.1002/qj.837.

Boden, T. A., et al. (2016), Global, Regional, and National Fossil-Fuel CO_2 Emissions. In: Carbon Dioxide Information Analysis Center, Oak Ridge National Laboratory, U.S. Department of Energy, Oak Ridge, Tenn., U.S.A., doi:10.3334/CDIAC/00001_V2016.

Bovensmann, H., et al. (1999), SCIAMACHY - Mission objectives and measurement modes, J. Atmos. Sci., 56, (2), 127-150.

Bovensmann, H., et al. (2010), A remote sensing technique for global monitoring of power plant CO_2 emissions from space and related applications, Atmos. Meas. Tech. 3, 781–811.

Bréon, F. M., et al. (2015), An attempt at estimating Paris area CO_2 emissions from atmospheric concentration measurements, Atmos. Chem. Phys., 15, 1707-1724, https://doi.org/10.5194/acp-15-1707-2015.

Brioude, J., et al. (2013), Top-down estimate of surface flux in the Los Angeles Basin using a mesoscale inverse modeling technique: assessing anthropogenic emissions of CO, NOx and CO_2

and their impacts, Atmos. Chem. Phys., 13(7), 3661-3677, doi:10.5194/acp-13-3661-2013.

Broquet, G., et al. (2011), A European summertime CO_2 biogenic flux inversion at mesoscale from continuous in situ mixing ratio measurements, J. Geophys. Res., 116, D23303, doi:10.1029/2011JD016202.

Bruhwiler, L., et al. (2014), CarbonTracker-CH_4: an assimilation system for estimating emissions of atmospheric methane, Atmospheric Chemistry and Physics, 14, 8269–8293, doi:10.5194/acp-14-8269-2014.

Bruhwiler, L., et al. (2017), US CH_4 emissions from oil and gas production: Have recent large increases been detected?, J. Geophys. Res., 122(7), 4070-4083, doi:10.1002/2016JD026157.

Buchwitz, M., et al. (2000), A near-infrared optimized DOAS method for the fast global retrieval of atmospheric CH_4, CO, CO_2, H_2O, and N_2O total column amounts from SCIAMACHY Envisat-1 nadir radiances, J. Geophys. Res. 105, 15,231-15,245.

Buchwitz, M., et al. (2015), The Greenhouse Gas Climate Change Initiative (GHG-CCI): comparison and quality assessment of near-surface-sensitive satellite-derived CO_2 and CH_4 global data sets, Remote Sensing of Environment, 162, 344-362, doi:10.1016/j.rse.2013.04.024.

Buchwitz, M., et al. (2016), Global satellite observations of column-averaged carbon dioxide and methane: The GHG-CCI XCO_2 and XCH_4 CRDP3 data set, Remote Sensing of Environment (in press), DOI: 10.1016/j.rse.2016.12.027, pp. 20.

Buchwitz, M., et al. (2017), Satellite-derived methane hotspot emission estimates using a fast data-driven method, Atmos. Chem. Phys., 17(9), 5751-5774, doi:10.5194/acp-17-5751-2017.

Burrows, J., et al. (1995), SCIAMACHY – Scanning Imaging Absorption Spectrometer for Atmospheric Chartography, Acta Astronaut., 35, 445–451.

Butz, A., et al. (2011), Toward accurate CO_2 and CH_4 observations from GOSAT, Geophysical Research Letters, 38, doi:10.1029/2011gl047888, 2011.

Calle, L., et al. (2016), Regional Carbon Fluxes from Land Use and Land Cover Change in Asia, 1980-2009, Env. Res. Lett., 11, 074011, doi:10.1088/1748-9326/11/7/074011.

Caulton, D. R., et al. (2014), Toward a better understanding and quantification of methane emissions from shale gas development, Proc. Natl. Acad. Sci. U. S. A., 111(17), 6237–6242, doi:10.1073/pnas.1316546111.

Chandra, N., et al. (2016), What controls the seasonal cycle of columnar methane observed by GOSAT over different regions in India?, Atmos. Chem. Phys., in review.

Chen, Z., et al. (2007), Correlative Learning: A Basis for Brain and Adaptive Systems, John Wiley & Sons, New York, 1st edn.

CIESIN/CIAT, CIESIN (Center for International Earth Science Information Network) (2005), Columbia University/CIAT (Centro Internacional de Agricultura Tropical): Gridded Population of the World Version 3 (GPWv3): Population Density Grids, Palisades, NY, Socioeconomic Data

and Applications Center (SEDAC), Columbia University, available at: http://sedac.ciesin.columbia.edu/gpw.

Conley, S., et al. (2016), Methane emissions from the 2015 Aliso Canyon blowout in Los Angeles, CA, Science, 351, 1317–20, doi:10.1126/science.aaf2348.

Cressot, C., et al. (2014), On the consistency between global and regional methane emissions inferred from SCIAMACHY, TANSO-FTS, IASI and surface measurements, Atmospheric Chemistry and Physics, 14, 577–592, doi:10. 5194/acp-14-577-2014.

Crisp, D., et al. (2004), The Orbiting Carbon Observatory (OCO) mission, Adv. Space Res., 34(4), 0273–1177, doi:10.1016/j.asr.2003.08.062.

Crisp, D., et al. (2008), NASA Orbiting Carbon Observatory: Measuring the column averaged carbon dioxide mole fraction from space, J. Appl. Remote Sens., 2, 023508, doi:10.1117/1.2898457.

Dee, D. P., et al. (2011), The ERA-Interim reanalysis: Configuration and performance of the data assimilation system, Q. J. R. Meteorol. Soc., 137(656), 553–597, doi:10.1002/qj.828.

Dlugokencky E. J., et al. (2005), Conversion of NOAA atmospheric dry air CH_4 mole fractions to a gravimetrically prepared standard scale, J. Geophys. Res., 110, D18306.

EDGAR42FT (2013), Global Emissions EDGAR v4.2 FT2010, http://edgar.jrc.ec.europa.eu/overview.php?v=42FT2010, last accessed: October 2015.

Enting, I. G. (2002), Inverse Problems in Atmospheric Constituent Transport, Cambridge University Press, Cambridge, doi: 10.1017/CBO9780511535741.

EPA, U. (2014), Inventory of U.S. Greenhouse Gas Emissions and Sinks: 1990 – 2012, Tech. rep., U.S. Environmental Protection Agency.

European Commission, Joint Research Centre (JRC)/Netherlands Environmental Assessment Agency (PBL) (2011), Emission Database for Global Atmospheric Research (EDGAR), release version 4.2. Available at http://edgar.jrc.ec.europa.eu.

Frankenberg, C., et al. (2005), Assessing methane emissions from global space-borne observations, Science, 308, 1010–4, doi:10.1126/science.1106644.

Frankenberg, C., et al. (2011), Global column-averaged methane mixing ratios from 2003 to 2009 as derived from SCIAMACHY: Trends and variability. Journal of Geophysical Research-Atmospheres 116. doi: 10.1029/2010jd014849.

Fraser, A., et al. (2013), Estimating regional methane surface fluxes: the relative importance of surface and GOSAT mole fraction measurements, Atmospheric Chemistry and Physics, 13, 5697–5713, doi:10.5194/acp-13-5697-2013.

Ganesan, A. L., et al. (2017), Atmospheric observations show accurate reporting and little growth in India's methane emissions, Nature Comm., 8(1), 836, doi:10.1038/s41467-017-00994-7.

Ganshin, A., et al. (2012), A global coupled Eulerian-Lagrangian model and 1 × 1 km CO_2 surface

flux dataset for high-resolution atmospheric CO_2 transport simulations, Geosci. Model Dev., 5, 231–243.

Global Methane Budget 2000-2012 (2016), Dataset (http://cdiac.ess-dive.lbl.gov/GCP/methanebudget/2016/, Last access 09/28/2017), doi:10.3334/CDIAC/Global_Methane_Budget_2016_v1.1

GLOBALVIEW-CO2 (2013), Cooperative Global Atmospheric Data Integration Project, updated annually. Multi-laboratory compilation of atmospheric carbon dioxide data for the period 2000–2012 (obspack_co2_1_PROTOTYPE_v1.0.4b_2014- 02-13), Compiled by NOAA Global Monitoring Division: Boulder, Colorado, U.S.A., doi:10.3334/OBSPACK/1002.

Gourdji, S. M., et al. (2008), Global monthly averaged CO_2 fluxes recovered using a geostatistical inverse modeling approach: 2. Results including auxiliary environmental data, Journal of Geophysical Research, 113, doi:10.1029/2007jd009733.

Grell, G. A., et al. (2005), Fully coupled "online" chemistry within the WRF model. Atmospheric Environment 39 (37):6957-6975. doi: 10.1016/j.atmosenv.2005.04.027.

Guan, D., et al. (2012), The gigatonne gap in China's carbon dioxide inventories. Nature Clim. Change, 2, 672–675, doi:10.1038/nclimate1560.

Hakkarainen, J., et al. (2016), Direct space-based observations of anthropogenic CO_2 emission areas from OCO-2, Geophys. Res. Lett., 43, 11,400–11,406, doi:10.1002/2016GL070885.

He, W., et al. (2017) CTDAS-Lagrange v1.0: A high-resolution data assimilation system for regional carbon dioxide observations, Geosci. Model Dev. Discuss., https://doi.org/10.5194/gmd-2017-222, in review.

Heald, C. L., et al. (2004), Comparative inverse analysis of satellite (MOPITT) and aircraft (TRACE-P) observations to estimate Asian sources of carbon monoxide, Journal of Geophysical Research- Atmospheres, 109, doi:10.1029/2004jd005185.

Heimann, M., and Keeling, C. D. (1989), In Aspects of Climate Variability in the Pacific and Western Americas (ed. Peterson, D. H.), AGU Geophys. Monogr., 55, 237−275.

Henne, S., et al. (2016), Validation of the Swiss methane emission inventory by atmospheric observations and inverse modelling, Atmos. Chem. Phys., 16(6), 3683-3710.

Henze, D. K., et al. (2007), Development of the adjoint of GEOS-Chem, Atmospheric Chemistry and Physics, 7, 2413–2433, doi:10.5194/acp-7-2413-2007.

Heymann, J., et al. (2015), Consistent satellite XCO_2 retrievals from SCIAMACHY and GOSAT using the BESD algorithm, Atmos. Meas. Tech., 8, 2961-2980.

Heymann, J., et al. (2017), CO_2 emission of Indonesian fires in 2015 estimated from satellite-derived atmospheric CO_2 concentrations, Geophys. Res. Lett., 44(3), 1537-1544, doi:10.1002/2016GL072042.

Hollmann, R., et al. (2013), The ESA Climate Change Initiative: satellite data records for essential

climate variables, Bulletin of the American Meteorological Society (BAMS), 0.1175/BAMS-D-11-00254.1, pp. 12.

Houweling, S., et al. (2015), An intercomparison of inverse models for estimating sources and sinks of CO_2 using GOSAT measurements, J. Geophys. Res., 120(10), 5253-5266, doi:10.1002/2014JD022962.

Houweling, S., et al. (2016), Global inverse modeling of CH_4 sources and sinks: An overview of methods, Atmospheric Chemistry and Physics Discussions, pp. 1–30, doi:10.5194/acp-2016-572.

Hsu, Y. K., et al. (2010), Methane emissions inventory verification in southern California, Atmospheric Environment, 44, 1–7, doi: Doi10.1016/J.Atmosenv.2009.10.002.

Inoue, M., et al. (2016), Bias corrections of GOSAT SWIR XCO_2 and XCH_4 with TCCON data and their evaluation using aircraft measurement data, Atmos. Meas. Tech., 9, 3491–3512.

IPCC (2013), Climate Change 2013: The Physical Science Basis, Contribution of Working Group I to the Fifth Assessment Report of the Intergovernmental Panel on Climate Change [Stocker, T.F., et al. (eds.)], Cambridge University Press, 1535 pp.

Ishijima, K., et al. (2010), The stratospheric influence on seasonal cycle of nitrous oxide in the troposphere as deduced from aircraft observation and model, J. Geophys. Res., 115, D20308.

Ishizawa, M., et al. (2016), Large XCH4 anomaly in summer 2013 over northeast Asia observed by GOSAT, Atmos. Chem. Phys., 16, 9149–9161.

Ito, A. (2010), Changing ecophysiological processes and carbon budget in East Asian ecosystems under near-future changes in climate: Implications for long-term monitoring from a process-based model, J. Plant Res., 123, 577–588.

Ito, A., et al. (2012), Use of a process-based model for assessing the methane budgets of global terrestrial ecosystems and evaluation of uncertainty. Biogeosciences 2012, 9, 759–773, doi:10.5194/bg-9-759-2012.

Jacob, D. J., et al. (2016), Satellite observations of atmospheric methane and their value for quantifying methane emissions, Atmos. Chem. Phys., 16(22), 14371-14396, doi:10.5194/acp-16-14371-2016.

Janardanan, R., et al. (2016), Comparing GOSAT observations of localized CO_2 enhancements by large emitters with inventory-based estimates. Geophysical Research Letters 2016, 43, 3486–3493, doi:10.1002/2016GL067843.

Janardanan, R., et al. (2017), Assessment of Anthropogenic Methane Emissions over Large Regions Based on GOSAT Observations and High Resolution Transport Modeling, Remote Sensing, 9(9), 941, doi:10.3390/rs9090941.

Janssens-Maenhout, G., et al. (2017), EDGAR v4.3.2 Global Atlas of the three major Greenhouse Gas Emissions for the period 1970-2012, Earth Syst. Sci. Data Discuss., 2017, 1-55, doi:10.5194/essd-2017-79.

Jeong, S., et al. (2012), Seasonal variation of CH_4 emissions from central California, Journal of Geophysical Research, 117, doi:10.1029/2011jd016896.

Jeong, S., et al. (2013), A multi-tower measurement network estimate of California's methane emissions, Journal of Geophysical Research: Atmospheres, 118, 11,339–11,351, doi:10.1002/jgrd.50854.

Jeong, S., et al. (2014), Spatially Explicit Methane Emissions from Petroleum Production and the Natural Gas System in California, Environ. Sci. Technol.,48, 5982–5990, doi:10.1021/es4046692.

Kaiser, J. W., et al. (2012), Biomass burning emissions estimated with a global fire assimilation system based on observed fire radiative power, Biogeosciences, 9, 527–554.

Kaminski, T., et al. (2001), Inverse modeling of atmospheric carbon dioxide fluxes, Science, 294, 259, doi:10.1126/science.294.5541.259a.

Kaminski, T., et al. (2001), On aggregation errors in atmospheric transport inversions, Journal of Geophysical Research, 106, 4703, doi:10.1029/2000jd900581.

Karion, A., et al. (2013), Methane emissions estimate from airborne measurements over a western United States natural gas field, Geophysical Research Letters, 40, 4393–4397, doi:10.1002/grl.50811.

Karion, A., et al. (2015), Aircraft-Based Estimate of Total Methane Emissions from the Barnett Shale Region, Environ. Sci. Technol., 49(13), 8124-8131, doi:10.1021/acs.est.5b00217.

Kirschke, S., et al. (2013), Three decades of global methane sources and sinks, Nature Geoscience, 6, 813–823, doi:10.1038/ngeo1955.

Korsbakken, J. I., et al. (2016), Uncertainties around reductions in China's coal use and CO_2 emissions. Nature Clim. Change, 6, 687–690, doi:10.1038/nclimate2963.

Kort, E. A., et al. (2012), Space-based observations of megacity carbon dioxide, Geophys. Res. Lett., 39, L17806, doi:10.1029/2012GL052738.

Kort, E. A., et al. (2014), Four corners: The largest US methane anomaly viewed from space, Geophys. Res. Lett., 41, 6898-6903, doi:10.1002/ 2014GL061503.

Kuze, A., et al. (2009), Thermal and near infrared sensor for carbon observation Fourier-transform spectrometer on the Greenhouse gases Observing Satellite for greenhouse gases monitoring, Appl. Opt., 48, 6716–6733.

Kuze, A., et al. (2016), Update on GOSAT TANSO-FTS performance, operations, and data products after more than 6 years in space, Atmospheric Measurement Techniques, 9, 2445–2461, doi:10.5194/amt-9-2445-2016.

Lauvaux, T., et al. (2016), High-resolution atmospheric inversion of urban CO_2 emissions during the dormant season of the Indianapolis Flux Experiment (INFLUX), J. Geophys. Res., 121(10), 5213-5236, doi:10.1002/2015JD024473.

Lavoie, T. N., et al. (2015), Aircraft-Based Measurements of Point Source Methane Emissions in the Barnett Shale Basin, Environ Sci Technol, 49, 7904–13, doi:10.1021/acs.est.5b00410.

Le Quéré, C., et al. (2015), Global carbon budget 2015. Earth Syst. Sci. Data, 7. 349–396, doi:10.5194/essd-7-349-2015.

Levelt, P. F., et al. (2006), The ozone monitoring instrument, IEEE Trans. on Geosci. Rem. Sens., 44(5), 1093–1101, doi:10.1109/TGRS.2006.872333.

Liu, Z., et al. (2015), Reduced carbon emission estimates from fossil fuel combustion and cement production in China. Nature, 524, 335–338, doi:10.1038/nature14677.

Maksyutov, S., et al. (2013), Regional CO_2 flux estimates for 2009-2010 based on GOSAT and ground-based CO_2 observations, Atmos. Chem. Phys., 13(18), 9351-9373, doi:10.5194/acp-13-9351-2013.

Manning, A., et al. (2011), Estimating UK methane and nitrous oxide emissions from 1990 to 2007 using an inversion modeling approach, J. Geophys. Res., 116, doi:10.1029/2010JD014763.

Maasakkers, J. D., et al. (2016), Gridded National Inventory of US Methane Emissions, Environ. Sci. Technol., 50, 13123–13133, doi:10.1021/acs.est.6b02878, 2016.

McKain, K., et al. (2015), Methane emissions from natural gas infrastructure and use in the urban region of Boston, Massachusetts, P. Natl. Acad. Sci. USA, 112(7), 1941-1946, doi:10.1073/pnas.1416261112.

McLinden, C. A., et al. (2016), Space-based detection of missing sulfur dioxide sources of global air pollution, Nat. Geosci., 9, 496–500, doi:10.1038/ngeo2724.

Michalak, A. M., et al. (2004), A geostatistical approach to surface flux estimation of atmospheric trace gases, Journal of Geophysical Research, 109, doi:10.1029/2003jd004422.

Michalak, A. M., et al. (2005), Maximum likelihood estimation of covariance parameters for Bayesian atmospheric trace gas surface flux inversions, Journal of Geophysical Research, 110, doi:10.1029/2005jd005970.

Miller, S. M., et al. (2012), Regional sources of nitrous oxide over the United States: Seasonal variation and spatial distribution, Journal of Geophysical Research, 117, doi: 10.1029/2011jd016951.

Miller, S. M., et al. (2013), Anthropogenic emissions of methane in the United States, Proc Natl Acad Sci U S A, 110, 20 018–22, doi:10.1073/pnas.1314392110.

Miller, S., and Michalak, A. (2017), Constraining sector-specific CO_2 and CH_4 emissions in the US, Atmos. Chem. Phys., 17(6), 3963-3985, doi:10.5194/acp-17-3963-2017.

Miller, S., et al. (2013), Anthropogenic emissions of methane in the United States, P. Natl. Acad. Sci. USA, 110(50), 20018-20022, doi:10.1073/pnas.1314392110.

Molod, A., et al. (2015), Development of the GEOS-5 atmospheric general circulation model from MERRA to MERRA2, Geosci. Model Dev. 8, 1339–1356.

Monteil, G., et al. (2013), Comparison of CH_4 inversions based on 15 months of GOSAT and SCIAMACHY observations, Journal of Geophysical Research: Atmospheres, 118, 11,807–11,823, doi: 10.1002/2013jd019760.

Morino, I., et al. (2011), Preliminary validation of column-averaged volume mixing ratios of carbon dioxide and methane retrieved from GOSAT short-wavelength infrared spectra, Atmospheric Measurement Techniques, 4(6), 1061–1076, doi:10.5194/amt-4-1061-2011.

Nassar, R., et al. (2014), Satellite observations of CO_2 from a Highly Elliptical Orbit for studies of the Arctic and boreal carbon cycle, J. Geophys. Res. Atm., 119, 2654-2673.

Nassar, R., et al. (2017), Quantifying CO_2 emissions from individual power plants from space, Geophys. Res. Lett., doi:10.1002/2017GL074702.

O'Brien., et al. (2016), Potential of a geostationary geoCARB mission to estimate surface emissions of CO_2, CH_4 and CO in a polluted urban environment: case study Shanghai, Atmos. Meas. Tech., 9(9), 4633-4654, doi:10.5194/amt-9-4633-2016.

Oda, T., and Maksyutov, S. (2011), A very high-resolution (1 km×1 km) global fossil fuel CO_2 emission inventory derived using a point source database and satellite observations of nighttime lights, Atmos. Chem. Phys., 11, 543–556, doi:10.5194/acp-11-543-2011.

O'Dell, C. W., et al. (2012), The ACOS CO_2 retrieval algorithm—Part 1: Description and validation against synthetic observations, Atmos. Meas. Tech., 5, 99–121, doi:10.5194/amt-5-99-2012.

Olivier J. G. J., et al. (2012 Edition), Part III: Greenhouse-Gas Emissions, IEA, Paris, France, 2012, ISBN:978-92-64-17475-7.

Olivier, J. G. J., et al. (2005), Recent trends in global greenhouse gas emissions: regional trends and spatial distribution of key sources, in: Non-CO_2 Greenhouse Gases (NCGG-4), A. van Amstel (Coord.), Millpress, Rotterdam, ISBN 90-5966-043-9, 325–330, 2005.

Olivier, J. G. J., et al. (2012), Trends in global CO_2 emissions, 2012 Report, PBL Netherlands Environmental Assessment Agency, The Hague, Joint Research Centre, Ispra, ISBN 978-92-79-25381-2, 2012.

Olivier, J. G. J., et al. (2014), Trends in global CO_2 emissions: 2014 Report. PBL Netherlands Environmental Assessment Agency, The Hague; European Commission, Joint Research Centre (JRC), Institute for Environment and Sustainability (IES), JRC report 93171/PBL report 1490.

Oney, B., et al. (2017), A CO-based method to determine the regional biospheric signal in atmospheric CO_2, Tellus B, 69, doi:10.1080/16000889.2017.1353388.

Onogi, K., et al. (2007), The JRA-25 Reanalysis, J. Meteorol. Soc. Jpn., 85, 369–432.

Pacala, S., et al. (2010), Verifying greenhouse gas emissions: methods to support international climate agreements. Committee on Methods for Estimating Greenhouse Gas Emissions, National Research Council Report, National Academies Press, Washington, ISBN 978-0-309-15211-2.

Pandey, S., et al. (2016), Inverse modeling of GOSAT-retrieved ratios of total column CH_4 and CO_2

for 2009 and 2010, Atmos. Chem. Phys., 16, 5043–5062.

Pandey, S., et al. (2017), Enhanced methane emissions from tropical wetlands during the 2011 La Nina, Scientific Reports, 7, doi:10.1038/srep45759.

Parker, R., et al. (2011), Methane observations from the Greenhouse Gases Observing SATellite: Comparison to ground-based TCCON data and model calculations, Geophysical Research Letters, 38, doi:10.1029/2011gl047871.

Parker, R. J., et al. (2015), Assessing 5 years of GOSAT Proxy XCH_4 data and associated uncertainties, Atmos. Meas. Tech., 8, 4785–4801, doi:10.5194/amt-8-4785-2015.

Parker, R., et al. (2016), Atmospheric CH_4 and CO_2 enhancements and biomass burning emission ratios derived from satellite observations of the 2015 Indonesian fire plumes, Atmos. Chem. Phys., 16(15), 10111-10131, doi:10.5194/acp-16-10111-2016.

Pasquill, F. (1961), The estimation of the dispersion of windborne material, The Meteorological Magazine, 90, No. 1063, 33-49.

Patra, P. K., et al. (2009) Growth rate, seasonal, synoptic, diurnal variations and budget of methane in lower atmosphere, J. Meteorol. Soc. Jpn., 87(4), 635–663.

Patra, P. K., et al. (2014), Observational evidence for interhemispheric hydroxyl parity, Nature, 513, 219–223.

Patra, P. K., et al. (2016), Regional methane emission estimation based on observed atmospheric concentrations (2002–2012). J. Meteorol Soc. Jpn., 94, 91–113, doi:10.2151/jmsj.2016-006.

Peischl, J., et al. (2012), Airborne observations of methane emissions from rice cultivation in the Sacramento Valley of California, Journal of Geophysical Research: Atmospheres, 117, doi:10.1029/2012jd017994, 2012.

Peischl, J., et al. (2013), Quantifying sources of methane using light alkanes in the Los Angeles basin, California, Journal of Geophysical Research: Atmospheres, 118, 4974–4990, doi:10.1002/jgrd.50413.

Peischl, J., et al. (2015), Quantifying atmospheric methane emissions from the Haynesville, Fayetteville, and northeastern Marcellus shale gas production regions, Journal of Geophysical Research-Atmospheres, 120, 2119–2139, doi:10.1002/2014JD022697.

Peischl, J., et al. (2016), Quantifying atmospheric methane emissions from oil and natural gas production in the Bakken shale region of North Dakota, Journal of Geophysical Research: Atmospheres, 121, 6101–6111, doi:10.1002/2015jd024631.

Peng, S., et al. (2016), Inventory of anthropogenic methane emissions in mainland China from 1980 to2010. Atmos. Chem. Phys., 16, 14545–14562, doi:10.5194/acp-16-14545-2016.

Peters, W., et al. (2007), An atmospheric perspective on North American carbon dioxide exchange: CarbonTracker, Proceedings of the National Academy of Sciences (PNAS) of the United States of America, 27 November 2007, 104(48), 18 925–18 930.

Pétron, G., et al. (2012), Hydrocarbon emissions characterization in the Colorado Front Range: A pilot study, J. Geophys. Res., 117(D4), D04304, doi:10.1029/2011JD016360.

Peylin, P., et al. (2013), Global atmospheric carbon budget: results from an ensemble of atmospheric CO_2 inversions. Biogeosciences, 10, 6699–6720, do:10.5194/bg-10-6699-2013.

Pickett-Heaps, C. A., et al. (2011), Magnitude and seasonality of wetland methane emissions from the Hudson Bay Lowlands (Canada), Atmospheric Chemistry and Physics, 11, 3773–3779, doi:10.5194/acp-11-3773-2011.

Prinn, R. G., et al. (2000), A history of chemically and radiatively important gases in air deduced from ALE/GAGE/AGAGE, J. Geophys. Res., 105, 17751-17792.

Rayner, P., et al. (1999), Reconstructing the recent carbon cycle from atmospheric CO_2, delta C-13 and O-2/N-2 observations, Tellus B, 51(2), 213-232, doi:10.1034/j.1600-0889.1999.t01-1-00008.x.

Rayner, P. J., and O'Brien, D. M. (2001), The utility of remotely sensed CO_2 concentration data in surface source inversions, Geophys. Res. Lett., 28(1), 175-178, doi:10.1029/2000GL011912.

Reuter, M., et al. (2010), A method for improved SCIAMACHY CO_2 retrieval in the presence of optically thin clouds, Atmos. Meas. Tech., 3, 209-232.

Reuter, M., et al. (2011), Retrieval of atmospheric CO_2 with enhanced accuracy and precision from SCIAMACHY: Validation with FTS measurements and comparison with model results, J. Geophys. Res., 116, D04301, doi:10.1029/2010JD015047.

Reuter, M., et al. (2014a), Satellite-inferred European carbon sink larger than expected, Atmos. Chem. Phys., 14, 13739-13753.

Reuter, M., et al. (2014b), Decreasing emissions of NOx relative to CO_2 in East Asia inferred from satellite observations, Nature Geoscience, 28 Sept. 2014, doi:10.1038/ngeo2257, pp.4.

Reuter, M., et al. (2017), How much CO_2 is taken up by the European terrestrial biosphere? Bull. Amer. Meteor. Soc. doi:10.1175/BAMS-D-15-00310.1, 24 April 2017, 665-671.

Rodenbeck, C., et al. (2003), Time-dependent atmospheric CO_2 inversions based on interannually varying tracer transport, Tellus B, 55(2), 488-497, doi:10.1034/j.1600-0889.2003.00033.x.

Rodgers, C. D. (2000), Inverse Methods for Atmospheric Sounding: Theory and Practice, World Sci., Singapore.

Ross, A., et al. (2013), First satellite measurements of carbon dioxide and methane emission ratios in wildfire plumes, Geophys. Res. Lett., 40(15), 4098-4102, doi:10.1002/grl.50733.

Rypdal, K., et al. (2005), Introducing top-down methods in assessing compliance with the Kyoto Protocol, Climate Policy, 5(4), 393-405, doi:10.1080/14693062.2005.9685565.

Saeki, T., and Patra, P. K. (2017), Implications of overestimated anthropogenic CO_2 emissions on East Asian and global land CO_2 flux inversion, Geoscience Letters, 4, 9, doi:10.1186/s40562-017-0074-7.

Saito, M., et al. (2014), Optimization of a prognostic biosphere model for terrestrial biomass and atmospheric CO_2 variability, Geosci. Model Dev., 7, 1829–1840.

Saito, M., et al. (2016), Enhanced Methane Emissions during Amazonian Drought by Biomass Burning, Plos One, 11(11), doi:10.1371/journal.pone.0166039.

Santoni, G. W., et al. (2014), California's methane budget derived from CalNex P-3 Aircraft Observations and a Lagrangian transport model, Journal of Geophysical Research.

Saunois, M., et al. (2016), The global methane budget 2000-2012, Earth System Science Data, 8(2), 697-751, doi:10.5194/essd-8-697-2016.

Schepers, D., et al. (2012), Methane retrievals from Greenhouse Gases Observing Satellite (GOSAT) shortwave infrared measurements: Performance comparison of proxy and physics retrieval algorithms, Journal of Geophysical Research, 117, doi: 10.1029/2012jd017549.

Schneising, O., et al. (2008), Three years of greenhouse gas column-averaged dry air mole fractions retrieved from satellite - Part 1: Carbon dioxide, Atmos. Chem. Phys., 8(14), 3827-3853, doi:10.5194/acp-8-3827-2008.

Schneising, O., et al. (2009), Three years of greenhouse gas column-averaged dry air mole fractions retrieved from satellite - Part 2: Methane, Atmos. Chem. Phys., 9, 443-465.

Schneising, O., et al. (2011), Long-term analysis of carbon dioxide and methane column-averaged mole fractions retrieved from SCIAMACHY, Atmos. Chem. Phys., 11(6), 2863-2880, doi:10.5194/acp-11-2863-2011.

Schneising, O., et al. (2013), Anthropogenic carbon dioxide source areas observed from space: assessment of regional enhancements and trends, Atmos. Chem. Phys., 13, 2445-2454, doi:10.5194/acp-13-2445-2013.

Schneising, O., et al. (2014a), Remote sensing of fugitive methane emissions from oil and gas production in North American tight geologic formations, Earths Future, 2(10), 548-558, doi:10.1002/2014EF000265.

Schneising, O., et al. (2014b), Terrestrial carbon sink observed from space: variation of growth rates and seasonal cycle amplitudes in response to interannual surface temperature variability, Atmos. Chem. Phys., 14, 133-141.

Schuh, A. E., et al. (2009), Seeing the forest through the trees: Recovering large-scale carbon flux biases in the midst of small-scale variability, Journal of Geophysical Research, 114, doi:10.1029/2008jg000842.

Sitch, S., et al. (2015), Recent trends and drivers of regional sources and sinks of carbon dioxide. Biogeosciences, 12, 653–679, doi:10.5194/bg-12-653-2015.

SkyTruth (2013), SkyTruth fracking chemical database. Available at http://frack.skytruth.org/fracking-chemical-database/frackchemical-data-download

Smith, M. L., et al. (2017), Airborne Quantification of Methane Emissions over the Four Corners

Region, Environ. Sci. Technol., 51 (10), 5832-5837, doi: 10.1021/acs.est.6b06107.

Spivakovsky, C., et al. (2000), Three-dimensional climatological distribution of tropospheric OH: update and evaluation, J. Geophys. Res. 105, 8931–8980.

Stohl, A., et al. (1998), Validation of the Lagrangian particle dispersion model FLEXPART against large-scale tracer experiment data, Atmos. Environ., 32, 4245–4264.

Stohl, A., et al. (2009), An analytical inversion method for determining regional and global emissions of greenhouse gases: Sensitivity studies and application to halocarbons, Atmos. Chem. Phys., 9(5), 1597-1620, doi:10.5194/acp-9-1597-2009.

Streets, D., et al. (2013), Emissions estimation from satellite retrievals: A review of current capability, Atmospheric Environment, 77, 1011-1042, doi:10.1016/j.atmosenv.2013.05.051.

Sudo, K., et al. (2002), CHASER: A global chemical model of the troposphere 1. Model description, J. Geophys. Res., 107, 4339.

Taylor, T. E., et al. (2011), Comparison of Cloud-Screening Methods Applied to GOSAT Near-Infrared Spectra, IEEE Trans. Geosci. Remote Sens., 50, 295-309, doi:10.1109/TGRS.2011.2160270

Taylor, T. E., et al. (2016), Orbiting Carbon Observatory-2 (OCO-2) cloud screening algorithms: validation against collocated MODIS and CALIOP data, Atmos. Meas. Tech., 9, 973–989, doi:10.5194/amt-9-973-2016.

Thompson, R. L., et al. (2016), Top–down assessment of the Asian carbon budget since the mid 1990s, Nature Comm., 7, 10724, doi:10.1038/ncomms10724.

Turner, A. J., and Jacob, D. (2015), Balancing aggregation and smoothing errors in inverse models, Atmospheric Chemistry and Physics, 15, 7039–7048, doi:10.5194/acp-15-7039-2015.

Turner, A., and Jacob, D. (2016), CMS (Carbon Monitoring System) Methane (CH_4) Flux for North America 0.5 degree x 0.667 degree V1, Greenbelt, MD, USA, Goddard Earth Sciences Data and Information Services Center (GES DISC), Accessed 09/08/2017, doi:10.5067/RF3R3G9I3UVX.

Turner, A. J., et al. (2015), Estimating global and North American methane emissions with high spatial resolution using GOSAT satellite data, Atmospheric Chemistry and Physics, 15, 7049–7069, doi: 10.5194/acp-15-7049-2015.

Turner, A. J., et al. (2016), A large increase in U.S. methane emissions over the past decade inferred from satellite data and surface observations, Geophys. Res. Lett., 43(5), 2218-2224, doi:10.1002/2016GL067987.

Turner, A. J., et al. (2017), Ambiguity in the causes for decadal trends in atmospheric methane and hydroxyl, Proc Natl Acad Sci U S A, 114, 5367–5372, doi:10.1073/pnas. 1616020114.

U.S. Energy Information Administration (2012), Shale oil maps. Bakken Shale Play, Williston Basin, North Dakota, Montana, Saskatchewan and Manitoba. Available at http://www.eia.gov/oil_gas/rpd/shaleoil1.pdf

U.S. Environmental Protection Agency (2014), Inventory of U.S. greenhouse gas emissions and sinks: 1990–2012. Available at http://www.epa.gov/climatechange/Downloads/ghgemissions/US-GHG-Inventory-2014-Main-Text.pdf and http://www.epa.gov/climatechange/Downloads/ghgemissions/US-GHG-Inventory-2014-Annexes.pdf

Umezawa, T., et al. (2014), Variations of tropospheric methane over Japan during 1988–2010. Tellus B, 66, 23837, doi:10.3402/tellusb.v66.23837.

Ummel, K. (2012), CARMA revisited: an updated database of carbon dioxide emissions from power plants worldwide. Center for Global Development, Working Paper 304.

Wecht, K. J., et al. (2012), Validation of TES methane with HIPPO aircraft observations: implications for inverse modeling of methane sources, Atmospheric Chemistry and Physics, 12, 1823–1832, doi: 10.5194/acp-12-1823-2012.

Wecht, K. J., et al. (2014a), Mapping of North American methane emissions with high spatial resolution by inversion of SCIAMACHY satellite data, Journal of Geophysical Research: Atmospheres, 119, 7741–7756, doi:10.1002/2014jd021551.

Wecht, K. J., et al. (2014b), Spatially resolving methane emissions in California: constraints from the CalNex aircraft campaign and from present (GOSAT, TES) and future (TROPOMI, geostationary) satellite observations, Atmospheric Chemistry and Physics, 14, 8173–8184, doi:10.5194/acp-14-8173-2014.

Wennberg, P. O., et al. (2012), On the sources of methane to the Los Angeles atmosphere, Environ Sci Technol, 46, 9282–9, doi:10.1021/es301138y.

Wheeler, D., and Ummel, K. (2008), Calculating CARMA: global estimation of CO_2 emissions from the power sector. Center for Global Development, Working Paper 145.

Wu, L., et al. (2011), Optimal representation of source-sink fluxes for mesoscale carbon dioxide inversion with synthetic data, Journal of Geophysical Research, 116, doi:10.1029/2011jd016198.

Wunch, D., et al. (2009), Emissions of greenhouse gases from a North American megacity, Geophysical Research Letters, 36, doi:10.1029/2009gl039825.

Wunch, D., et al. (2011), The Total Carbon Column Observing Network, Phil. Trans. R. Soc. A, 369, 2087–2112, doi:10.1098/rsta.2010.0240.

Wunch, D., et al. (2017), Comparisons of the Orbiting Carbon Observatory-2 (OCO-2) XCO_2 measurements with TCCON, Atmos. Meas. Tech., 10, 2209–2238.

Yokota, T., et al. (2009), Global concentrations of CO_2 and CH_4 retrieved from GOSAT: First preliminary results, SOLA, 5, 160–163.

Yoshida, Y., et al. (2013), Improvement of the retrieval algorithm for GOSAT SWIR XCO_2 and XCH_4 and their validation using TCCON data, Atmos. Meas. Tech., 6, 1533–1547.

Zavala-Araiza, D., et al. (2015), Reconciling divergent estimates of oil and gas methane emissions, P. Natl. Acad. Sci. USA, 112(51), 15597-15602, doi:10.1073/pnas.1522126112.

Zhao, C. F., et al. (2009), Atmospheric inverse estimates of methane emissions from Central California, Journal of Geophysical Research-Atmospheres, 114, doi:10.1029/2008jd011671.

APPENDIX-2 ACRONYMS AND ABBREVIATIONS

ACOS	Atmospheric CO_2 Observations from Space
ACTM	Atmosphere Chemistry-Transport Model
AGCM	Atmospheric General Circulation Model
CAI	Cloud and Aerosol Imager
CAMS	Copernicus Atmosphere Monitoring Service
CARBONES	CARBON Environmental Service
CARMA	Carbon Monitoring for Action
CCI	Climate Change Initiative
CCSR	Center for Climate System Research
CDIAC	Carbon Dioxide Information Analysis Center
COP	Conference of the Parties
CTM	Chemistry-Transport Model
DGVM	Dynamic Global Vegetation Model
ECMWF	European Centre for Medium-range Weather Forecasts
EDGAR	Emission Database for Global Atmospheric Research
ENVISAT	ENVIronmental SATellite
EPA	Environmental Protection Agency
ESA	European Space Agency
ESRL	Earth System Research Laboratory
ESS-DIVE	Environmental System Science Data Infrastructure for a Virtual Ecosystem
FAO	Food and Agriculture Organization
FFC	Fossil Fuel consumption and Cement production
FLEXPART	FLEXible PARTicle dispersion model
FRA	Forest Resource Assessment
FRCGC	Frontier Research Center for Global Change
FTS	Fourier Transform Spectrometer
GCP	Global Carbon Project
GDAS	GOSAT Data Archive Service
GDP	Gross Domestic Product
GEO	Geostationary Orbit
GEOS	Goddard Earth Observing System
GFAS	Global Fire Assimilation System
GHG	GreenHouse Gas
GMM	Gaussian Mixture Model

GOSAT	Greenhouse gases Observing SATellite
IAV	InterAnnual Variation
IEA	International Energy Agency
IFOV	Instantaneous Field of View
IPCC	Intergovernmental Panel on Climate Change
JAMSTEC	Japan Agency for Marine-Earth Science and Technology
JAXA	Japan Aerospace Exploration Agency
JCDAS	JMA Climate Dara Assimilation System
JMA	Japan Meteorological Agency
KIT	Karlsruhe Institute for Technology
LEO	Low Earth Orbit
LSCE	Laboratoire des Sciences du Climat et de l'Environnement
LWIR	Long-Wavelength InfraRed
MERLIN	Methane Remote Sensing Lidar Mission
MERRA	Modern-Era Retrospective analysis for Research and Applications
MODIS	MODerate resolution Imaging Spectroradiometer
MOE	Ministry of the Environment
MPI BGC	Max Planck Institute for Biogeochemistry
MRV	Measurement, Reporting and Verification
MWIR	Mid-Wavelength InfraRed
NASA	National Aeronautics and Space Administration
NDCs	Nationally Determined Contributions
NIES	National Institute for Environmental Studies
NIR	Near InfraRed
NOAA	National Oceanic and Atmospheric Administration
OCO	Orbiting Carbon Observatory
ODIAC	Open-source Data Inventory for Anthropogenic CO_2
OMI	Ozone Monitoring Instrument
RBF	Radial Basis Function
SCIAMACHY	SCanning Imaging Absorption spectroMeter for Atmospheric CHartographY
SDGs	Sustainable Development Goals
SWIR	Short Wavelength InfraRed
TCCON	Total Carbon Column Observing Network
TFI	Task Force on National Greenhouse Gas Inventories
TIR	Thermal InfraRed
TROPOMI	TROPOspheric Monitoring Instrument

UN	United Nations
UNFCCC	United Nations Framework Convention on Climate Change
UV	Ultra Violet
VISIT	Vegetation Integrative SImulator for Trace gases
WDCGG	World Data Center for Greenhouse Gases
WMO	World Meteorological Organization
WMO GAW	World Meteorological Organization Global Atmospheric Watch
WRF	Weather Research and Forecasting

APPENDIX-3 LIST OF GREENHOUSE GAS MEASURING SATELLITES

Table. List of Past and Existing Satellites for Remote Sensing of Greenhouse Gases Using the SWIR Region.

Satellite	Envisat	Instrument	SCIAMACHY
Country / Organization	(Satellite) ESA (Instrument) Germany, Netherlands, and Belgium	Period	2002 - 2012
Orbit Type / Altitude	Sun synchronous / 782 km	Orbit Recurrent Period	35 days
Type of Instrument	Nadir and limb viewing grating imaging spectrometer		
Spectral Range	UV to SWIR	Target Gases	O_3, NO_2, BrO, SO_2, HCHO, OClO, H_2O/D_2O, CH_4, CO, CO_2
Swath	1000 km	Nadir Footprint Size	32 x 60 km
Project Website	http://www.sciamachy.org http://www.esa-ghg-cci.org/		
Data Website	http://www.sciamachy.org/products/ http://www.esa-ghg-cci.org/sites/default/files/documents/public/documents/GHG-CCI_DATA.html		
Level 1B ATBD	https://earth.esa.int/documents/700255/708683/ENV-ATB-DLR-SCIA-0041-6-SCIA-L1B-ATBD.pdf		
Leve 2 Algorithm Documentation	See links to ATBDs on http://www.esa-ghg-cci.org/sites/default/files/documents/public/documents/GHG-CCI_DATA.html		
Validation Report	http://www.esa-ghg-cci.org/?q=webfm_send/352		
Detailed Product Information	http://www.esa-ghg-cci.org/index.php?q=webfm_send/160		

Satellite	GOSAT	Instrument	TANSO-FTS
Country / Organization	Japan	Period	2009 - present
Orbit Type / Altitude	Sun synchronous / 666 km	Orbit Recurrent Period	3 days
Type of Instrument	Nadir viewing Fourier transform spectrometer		
Spectral Range	SWIR and TIR	Target Gases	CO_2, CH_4, and H_2O
Cross Track Pointing	±35 °	Nadir Footprint Size	10.5 km (diameter)
Project website	http://www.gosat.nies.go.jp/en/index.html http://www.jaxa.jp/projects/sat/gosat/		
Data Website	https://data2.gosat.nies.go.jp		
Level 1 ATBD	-		
Level 2 ATBD	(SWIR) https://data2.gosat.nies.go.jp/doc/documents/ATBD_FTSSWIRL2_V2.0_en.pdf (TIR) -		
Validation Report	(SWIR) https://data2.gosat.nies.go.jp/doc/documents/ValidationResult_FTSSWIRL2_V02.xx_GU_en.pdf		

Satellite	OCO-2	Instrument	-
Country / Organization	US	Period	2014 - present
Orbit Type / Altitude	Sun synchronous / 705 km	Orbit Recurrent Period	16 days
Type of Instrument	Grating imaging spectrometer		
Spectral Range	SWIR	Target Gases	CO_2
Swath	10.3 km	Nadir Footprint Size	1.3 x 2.3 km
Project website	https://oco.jpl.nasa.gov		
Data Website	https://daac.gsfc.nasa.gov		
Level 1 ATBD	https://docserver.gesdisc.eosdis.nasa.gov/public/project/OCO/OCO2_L1B_ATBD.V7.pdf		
Level 2 ATBD	https://docserver.gesdisc.eosdis.nasa.gov/public/project/OCO/OCO2_L2_ATBD.V6.pdf		
Validation Plan	https://oco.jpl.nasa.gov/files/ocov2/OCO-2_SciValPlan_111005_ver1_0_revA_final_signed1.pdf		

Satellite	TanSat	Instrument	ACGS (Former CDS)
Country / Organization	China	Period	2016 - present
Orbit Type / Altitude	Sun synchronous / ≈700km	Orbit Recurrent Period	16 days
Type of Instrument	Grating imaging spectrometer		
Spectral Range	SWIR	Target Gases	CO_2
Swath	-	IFOV	-
Project website	-		
Data Website	http://chinageoss.org/tansat/index.html http://data.nsmc.org.cn/portalsite/default.aspx		
Level 1 ATBD	-		
Level 2 ATBD	-		
Validation Plan	-		

Satellite	Sentinel 5p	Instrument	TROPOMI
Country / Organization	EC	Period	2017 - present
Orbit Type / Altitude	Sun synchronous / 824 km	Orbit Recurrent Period	17 days
Type of Instrument	Grating imaging spectrometer		
Spectral Range	UV and SWIR	Target Gases	CO, HCHO, CH_4, NO_2, SO_2, and O_3
Swath	2600 km	Nadir Footprint Size	7 x 7 km
Project website	http://www.tropomi.eu, http://www.tropomi.nl		
Data Website	-		
Level 1 ATBD	http://www.tropomi.eu/sites/default/files/files/S5P-KNMI-L01B-0009-SD-algorithm_theoretical_basis_document-8.0.0-20170601_0.pdf		
Level 2 ATBD	(CH_4)http://www.tropomi.eu/sites/default/files/files/SRON-S5P-LEV2-RP-001_TROPOMI_ATBD_CH4_v1p0p0_20160205.pdf		

Note : The SWIR region includes O_2A band around 760 nm.